



**NTNU – Trondheim**  
Norwegian University of  
Science and Technology

# Probabilistic Design of Midship Panel based on Model scale compressive Ice Test

**Karoline Mali Neumann**

Marine Technology

Submission date: July 2013

Supervisor: Bernt Johan Leira, IMT

Co-supervisor: Sören Ehlers, IMT  
Pentti Kujala, Aalto University

Norwegian University of Science and Technology  
Department of Marine Technology



# Probabilistic design of midship panel based on model scale compressive ice test

Karoline Mali Neumann

July 3, 2013

Master thesis



**NTNU – Trondheim**  
Norwegian University of  
Science and Technology

## Assignment

### Probabilistic design of midship panel based on model scale compressive ice test

#### Probabilistisk design av midskip panel basert på modell-test i is under kompresjon

Ship-ice interaction is a complicated process causing stochastically varying contact pressure on the hull. Typically, in all ice class rules, the design pressure to be used for various structural elements is defined "as nominal" affecting on a certain area. The new measurements conducted in model scale in Aalto ice tank has revealed new insight about the nature of the contact between ship and ice. It has been shown that the contact between the ship and ice resulting from the ice-breaking process is fluctuating, and can be described by pressure area-curves.

The aim of the thesis is to identify the pressure area relationship, and to predict loads based on the model scale experiment. The model scale results will be scaled to full scale. Design-load should be defined as a function of contact area with proper occurrence probability level. The scantlings to be used will be optimized for weight and cost, using the defined design load.

The following subjects will be examined in this thesis:

1. Ice features relevant for local ice pressure are to be described. A review of different classification societies' rules for local ice load design is to be performed. The nature of local ice pressure and the associated physical ice breaking processes are to be highlighted.
2. Measurements from pressure cells installed on a ship model in the Aalto Ice Tank are to be analyzed. The spatial and temporal properties of the contact pressure are to be investigated
3. Statistical analysis tools are used to obtain the design load as a function of area for the applied ice thickness (as defined in the model scale tests). By conducting literature studies, the loads are scaled to the design ice thickness to be used in a specific case study which is to be agreed upon with the supervisors.

4. The scantlings of the hull which is selected for the case study are to be optimized based on the obtained pressure as a function of area, in addition to a cost objective.

The work scope may prove to be larger than initially anticipated. Subject to approval from the supervisor, topics may be deleted from the list above or reduced in extent.

In the thesis the candidate shall present her personal contribution to the resolution of problems within the scope of the thesis work.

Theories and conclusions should be based on mathematical derivations and/or logic reasoning identifying the various steps in the deduction.

The candidate should utilize the existing possibilities for obtaining relevant literature.

The thesis should be organized in a rational manner to give a clear exposition of results, assessments, and conclusions. The text should be brief and to the point, with a clear language. Telegraphic language should be avoided.

The thesis shall contain the following elements: A text defining the scope, preface, list of contents, summary, main body of thesis, conclusions with recommendations for further work, list of symbols and acronyms, references and (optional) appendices. All figures, tables and equations shall be numbered.

The supervisor may require that the candidate, in an early stage of the work, presents a written plan for the completion of the work.

The original contribution of the candidate and material taken from other sources shall be clearly defined. Work from other sources shall be properly referenced using an acknowledged referencing system.

The thesis shall be submitted in electronic form:

- Signed by the candidate
- The text defining the scope included
- Drawings and/or computer prints which cannot be bound should be organized in a separate folder

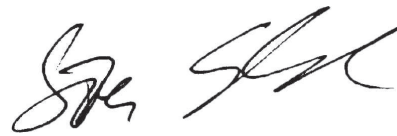
Supervisors:

Prof. Bernt J. Leira

Prof. Sören Ehlers

Prof. Pentti Kujala (Aalto University)

\_\_\_\_\_  
Prof. Bernt J. Leira



\_\_\_\_\_  
Prof. Sören Ehlers

Deadline: July 22nd 2013  
Trondheim, January 14th 2013

## Abstract

This thesis is investigating compressive ice loads acting on the midship using a model experiment performed in Aalto ice tank where a tactile sensor was mounted on the side. In order to get insight in the very complex behavior of ice; the sea ice growth, mechanical properties and failure mechanisms are presented. Further some previous work on the topic is presented, with discussion, in addition to regulations on local ice loads and structure requirements. The execution of the experiment is described, and the method for processing the data and based on this data using probabilistic design to design a midship panel. For datasets where the interaction area is semi-continuous a new event definition is proposed, based on temporal events consisting of spatial events. The maximum event method developed by [Jordaan et al., 1993] is applied in sampling data from the new temporal events. Data is sampled for increasing area sizes corresponding to number of connected triggered sensor cells. The data is adjusted for exposure in order to have a standardized curve corresponding to the area in question. An exponential distribution is fitted to the tail of the data, and presented in a Weibull probability plot. The parameters of the distributions,  $x_0$  and  $\alpha$  are functions of area. Assuming the area is acting in a line corresponding to the span of a longitudinally framed panel, and given a return period and a scenario, a design load is predicted. Based on this load, scantlings of a panel is recommended which also complies with Finnish-Swedish ice class rules. The integrity of the structure is checked using Monte Carlo analysis. To get more insight into the data set, a local pressure area curve, and an average pressure over total measured contact area relationship is presented for the entire data set, as well as spatial and process pressure area curves and pressure history for the biggest load event and the biggest pressure event.

## Acknowledgments

I would like to express my sincere appreciation to my supervisors, Bernt Johan Leira who has guided me and given valuable feedback, Sören Ehlers for always answering my frequent requests, sharing his contacts and knowledge, and Pentti Kujala at Aalto University for access to the data, help with interpreting and suggestions to improvement. Special thanks goes to Mikko Suominen for answering my inquiries, providing data and literature and more insight into the data. I am also thankful for the conversation with Rüdiger on Bock und Polach who gave me insight to the scaling of model ice. Thanks goes to the SAFEWIN project, which is a part of the EU FP7 project and all it's associates, and the staff at Aalto ice tank for making this possible. My parents' and Sebastian Mevatne's help with editorial support is also greatly acknowledged. I would further like to thank MEMO as and Jon Willy Klaussen for offering office space and printer in the final stage of my work. Finally I wouldn't be able to write this if it wasn't for all the persons in the references, I would especially like to point out Ian Jordaan and Rocky Taylor whom my work is greatly dependent on. Especially thanks to Ian Jordaan and also Ralph Freeman for their feedback on my early work.

*Karoline Mali Neumann*

Karoline Mali Neumann



# Contents

<b>Assignment</b>	<b>i</b>
<b>1 Introduction</b>	<b>1</b>
1.1 Limitations . . . . .	1
1.2 Formation and structure of sea ice . . . . .	2
1.3 Engineering properties of sea ice . . . . .	6
1.3.1 Tensile strength . . . . .	6
1.3.2 Flexural strength . . . . .	6
1.3.3 Compressive strength . . . . .	7
1.3.4 Other properties . . . . .	7
1.4 Failure modes . . . . .	9
1.4.1 Crushing and high pressure zones . . . . .	9
1.5 Previous work . . . . .	11
1.5.1 Full scale measurements . . . . .	11
1.5.2 Model scale experiments . . . . .	13
1.5.3 Discussion of analysis of historic data . . . . .	14
1.6 Most relevant literature . . . . .	20
1.6.1 Compressive ice and damages . . . . .	22
1.7 Regulations . . . . .	24
1.7.1 Finnish-Swedish ice class rules . . . . .	24
<b>2 Model scale experiment</b>	<b>26</b>
2.1 Description of experiment . . . . .	26
2.1.1 Scaling of model ice . . . . .	27
2.1.2 I-SCAN tactile sensor . . . . .	30
2.1.3 Sources of error . . . . .	31
<b>3 Methodology</b>	<b>32</b>
3.1 Motivation . . . . .	32
3.2 Sampling based on spatial and temporal event definitions . . . . .	33
3.3 Applied pressure area relationships . . . . .	34
3.4 Methodology for design of panel . . . . .	35
3.4.1 Area distributions sampling . . . . .	36
3.4.2 Adjusting for exposure of internal areas of increasing size . . . . .	36
3.4.3 Statistics . . . . .	37
3.4.4 Design curves . . . . .	37

3.4.5	Scenario . . . . .	38
3.4.6	Design procedure . . . . .	38
3.4.7	Monte Carlo . . . . .	39
3.5	Exposure . . . . .	40
3.6	Matlab functions . . . . .	41
<b>4</b>	<b>Results</b>	<b>42</b>
4.1	Exposure of cells . . . . .	42
4.2	Critical events . . . . .	48
4.2.1	Maximum load event . . . . .	48
4.2.2	Maximum triggered cell . . . . .	51
4.3	Pressure-area curves . . . . .	53
4.3.1	Distribution . . . . .	56
4.3.2	Design curves . . . . .	58
4.3.3	Return period . . . . .	61
4.4	Optimized structure . . . . .	61
4.4.1	Monte Carlo simulation . . . . .	63
<b>5</b>	<b>Discussion</b>	<b>65</b>
5.1	Exposure of cells . . . . .	65
5.2	Distributions and design curves tendencies . . . . .	65
5.3	Optimized structure . . . . .	69
<b>6</b>	<b>Conclusion</b>	<b>70</b>
6.1	Further work . . . . .	71
<b>7</b>	<b>References</b>	<b>72</b>
<b>A</b>	<b>DNV strength rules for ships navigating in ice</b>	<b>77</b>
<b>B</b>	<b>Matlab functions</b>	<b>81</b>
<b>C</b>	<b>Float charts</b>	<b>88</b>
<b>D</b>	<b>Weibull probability plots for each area</b>	<b>90</b>
<b>E</b>	<b>Results from monte carlo simulation</b>	<b>102</b>
<b>F</b>	<b>Cusp breaking and rotating</b>	<b>108</b>

# 1 Introduction

Compressive ice can cause ships to be stuck in ice, and may cause large loads and damage vertical midships. Compressive ice occurs if the wind or current is directed towards a boundary such as the shore causing a pressure within the ice field. Kujala [1991a] investigates damages to ships in the Baltic sea 1084-1987 and states that "most of the damages appear at midship and have occurred while the ships have been stuck in compressive ice" . The loads associated with compressive ice is largely unknown, and due to cost of full scale experiments, prediction of compressive ice loads is here proposed approached with model tests. A compressive ice test with a model equipped with a tactile sensor at midship is made available from Aalto University. The methodology used to process the data, and, based on the distribution, design a panel is based on Jordaan et al. [1993] and Taylor et al. [2010].

## 1.1 Limitations

This thesis is mainly concerned with data processing in order to obtain distributions and design curves according to Jordaan et al. [1993] and Taylor et al. [2010] and analysis of the results based on this. From the data processing, pressure area curves will be obtained, and the most critical pressure and load from the data set will be given special attention. Based on the design curves, a probabilistic design methodology is applied in order to recommend scantlings for plate and stiffener in the ice zone midship, balanced with a qualitative economy objective. Several options will be considered, but spacing in the case of longitudinal framing and span in the case of transversal framing will be kept constant. For simplicity, one kind of stiffener alternative is chosen, L-profiles in different sizes from the manufacturer Ruukki. Only one run where the model is towed in severe compressive ice in a channel is considered, because of limit of time, although there are more runs in the experiment. The data population is thus limiting. Time also limits the workload, in that more complicated algorithms are avoided. The quality of the experiment will not be the main focus. Unexpected results that fall outside of the objective is not followed further. The specifics of the instrumentation limits the resolution of data, see details in subsection 2.1.2. The data available is from Aalto ice tank, and the methods and possibilities of the staff and tank there sets the framework for the work conducted here. Here, large loads are of interest, and thus more important than smaller values.

## 1.2 Formation and structure of sea ice

The structure and therefore the properties of sea ice is highly dependent on the environmental history, which affects the growth. This paragraph is based on knowledge obtained from Weeks [2010]. Salt water starts to freeze at about  $-1.8\text{ }^{\circ}\text{C}$ , depending on the salinity. The nucleation of ice crystals is aided by particles such as salt and pollution in the air, but also sometimes by crashing with other ice crystals. The crystal starts out as a small disk, growing slowly, and if conditions are calm, it starts to grow arms to more effectively dissipate energy, and growth rate increases. Ice crystals are hexagonal, as shown in Figure 1, showing the basal plane described by the a-axes, and the c-axis parallel to this plane. The flat initial crystal will have 6 arms, parallel to the a-axes. It grows more easily in the basal plane, and the ratio of the dimension in the basal plane to the c-axis direction is of typically 50 000:1 [Weeks, 2010]. As the dendric hexagonal star crystals grow, they start to intersect and connect arms with other crystals, forming a thin, black appearing layer under very calm and cold conditions. More likely for sea ice, there will be waves, wind, swell, turbulence, generally mixing and disturbing and nothing like calm conditions. Any attempt to grow needles from a disc will be cut off in crashing with other crystals. The mixing will cause a larger portion of the upper surface to be at freezing temperatures, creating a layer with crystals embedded in seawater. As this soup grows and becomes increasingly viscous it is called grease ice. As there gets more of them they start to bond and in-between water also eventually freezes, forming a tougher crust. When so tough that the vertical movement is prohibited, the conditions for growth changes. Growth rate is affected by the temperature gradient through the ice sheet, and the conductivity of it. Besides, the only way to grow is now downwards. In the initial layer, crystal orientations are random giving an isotropic structure of small grains. Now the transition layer starts, where crystals trying to grow any other direction than downwards will be cut off by other crystals. As mentioned, the local preferable growth direction is along the basal plane, so the surviving crystals will be oriented with basal plane, meaning plane of the a-axes vertically. As grains other than those growing downwards are extinct, the columnar zone starts where crystals can grow parallel without interfering, and the grain sizes are gradually increasing. As seen in Figure 3, the columnar zone dominates the thickness, and first year sea ice is because of this treated as an anisotropic material. The c-axis is, as a result of the orientation, in the horizontal plane. They can

be in random directions, or could be aligned. The reason for alignment is believed to correspond a general mean current. An illustration of the packing of ice crystals can be seen in Figure 2, where the c-axes are aligned. The alternatives A, B and C shows idealized packing of a hexagonal metal, zinc, which is far more strict than the ice seen under. Even so, it may best be described by packing structure B. Slight misalignment leads to small spaces between the grains allowing for impurities like brine, salts and gas. The higher growth rate, the higher porosity and consequently lower strength of the ice specimen. In the bottom of the ice is the skeleton layer. This is very weak, as not all grains grow as fast, and some are reaching below the others, and there is a lack of ice-ice contact between them. This layer can easily be scraped off by hand, and is easily damaged if trying to obtain a sample. This description is a simplified description of first year level ice growing by heat gradient through the ice. In reality ice can grow by mechanical means, from snow falling, rafting and ridging. Old ice, meaning second and multi-year ice is generally considered isotropic because of the many random orientations resulting from mechanical growth, degradations, snowfall and new growth.

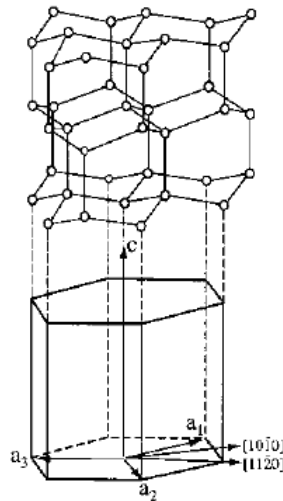


Figure 1: Hexagonal structure of ice with c-axis upwards, and the a-axes in the basal plane [Weeks, 2010]

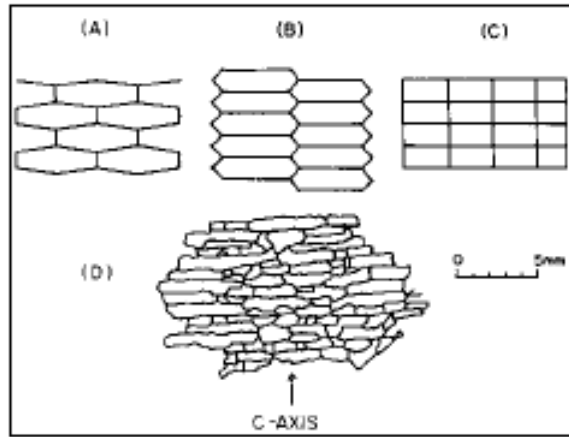


Figure 2: Packing of ice crystals [Weeks, 2010]

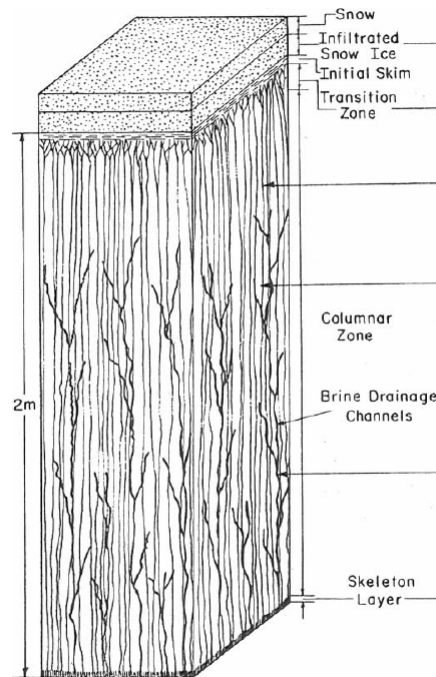


Figure 3: The different zones over the thickness of sea ice [Tuh]

Thermodynamic ice growth may be determined from Stefan’s law, which states that the ice thickness is proportional to the sum of freezing degree days, as shown in Equation 1, where subscript b is for bottom and a for air as it is assumed that the surface of the ice is equal to the air above. This formula is somewhat over predicting and is often used multiplied with a factor less than 1. The limit of thermodynamic growth is about 2 meters [Timco and Weeks, 2010]. Different ice properties is often expressed as function of brine volume, temperature or salinity. Brine volume is a function of temperature and salinity as shown in Equation 2, where typical salinities for first year ice is 4-6 ppm, and temperature profile typically linear over the thickness in growing ice [Timco and Weeks, 2010]. From this one can conclude that properties dependent on brine volume or temperature may vary properties from top to bottom. Not just growth conditions of ice determines properties, but also deterioration. Sea ice consists of solid ice, brine and gas. The porosity of ice may also be a factor for mechanical properties, and is the ratio between ice volume and sum of brine and gas volume. When the temperature increases, more salts dissolve in brine pockets inside the ice, they increase in size and interconnect, forming brine drainage channels as illustrated in Figure 3. This way the ice gets less salty, but still has high porosity. Typical density of first year ice is 0.84-0.91  $Mgm^{-3}$  above the waterline, and 0.90-0.94  $Mgm^{-3}$  below [Timco and Weeks, 2010].

$$h = \sqrt{\frac{2k_i}{\rho_i L}} \sqrt{[(T_b - T_a)t]} \quad (1)$$

$$v_b = S_i \left[ \frac{49.185}{T_i} + 0.532 \right] \quad (2)$$

## 1.3 Engineering properties of sea ice

With the growth and structure of sea ice in mind, relevant mechanical properties of sea ice will be presented based on Timco and Weeks [2010].

### 1.3.1 Tensile strength

When measuring the tensile strength a small sample is collected, and machined to a cylinder which should be perfectly aligned. Low temperature is required to prevent brine drainage. The contact between the testing machine and the ice should be so that the ice fails internally and not by the contact. Values are from 0.2 to 0.8 MPa in the horizontal direction (perpendicular to the basal plane) and about 3 times higher, up to 2 MPa in the vertical direction (direction of growth and columnar grains), while old ice has values from 0.5 to 1.5 MPa [Timco and Weeks, 2010]. Generally tensile strength is increasing with decreasing temperature, decreasing porosity, and only slightly increasing by loading rate.

### 1.3.2 Flexural strength

Flexural strength is not a material property, but serves more as an index value. This is still measured as under many circumstances ice fail under flexural conditions and it is easy to perform large in situ tests. One possibility is to saw out a cantilever beam from the ice, opening for water around 3 sides, and leaving one short side connected and load until failure. A beam can also be removed from the water, and simply supported on two sides, loaded with one or two point loads until failure at the middle. The tests are analyzed with simple elastic beam theory, which assumes that the beam is homogeneous and perfectly elastic. As explained in subsection 1.2, sea ice is considered anisotropic because of the columnar grains, in addition it behaves viscoelastic, and sometimes brittle under high loading rates, so beam theory assumptions is definitely not valid for a sea ice beam. If it was valid, flexural strength and tensile strength would be the same. Flexural strength values range from 1 MPa and decreasing with brine volume, while ice that is not growing show values from 100 to 150 kPa [Timco and Weeks, 2010]. For sea ice there is not a difference between large and small beams as it is for fresh water ice, where a stress concentration at the root is dominating the test. As also indicated by tensile strength, the flexural strength is not strongly dependent on loading rate. When sawing out from the floating ice sheet, a



horizontal specimen is tested, but values from tests on vertically cut beams shows 2-2.5 times higher values [Timco and Weeks, 2010]. Orientation of the beam in the horizontal plane does not show different values for initial frazil layer or for randomly oriented c-axis, but in the case of aligned c-axis the flexural strength was higher in the c direction. Beams were also tested both from over and underside, but showed little difference in values. Old ice estimates are 0.8 to 1.1 MPa in winter and 0.4 to 0.6 MPa in summer [Timco and Weeks, 2010].

### 1.3.3 Compressive strength

For testing of compressive strength, cylinders are cut out from the ice and tested in an apparatus that can generate high loads. At the same time as applying a known load, the sample is monitored by extensometers measuring the strain, to obtain the effective elastic modulus at the same time. Compressive strength is a function of strain rate, and total porosity  $v_t$ , as in Equation 3. For horizontally loaded columnar ice, a is 37 and b 270, for vertical a=160 and b=200, and for granular ice a = 49 and b = 280 [Timco and Weeks, 2010]. These were observed for strain rates between  $10^{-7}s^{-1}$  and  $2 \cdot 10^{-4}s^{-1}$ , for higher strain rate brittle behavior can occur. Values ranges from 0.4 MPa to 5 MPa, and is a strong function of loading rate up to  $10^{-4}s^{-1}$ . Old ice exhibits values from 7 to 15 MPa. Compressive strength under confining pressure increases from 1.2 to 4 times higher depending on type of confinement and strain rate. Note that compressive strength is much higher than the other strength parameters, and may therefor cause high loads on structures when the ice fails in compression, as it does in the experiment handled in this thesis.

$$\sigma_c = a \cdot \epsilon^{0.22} \left(1 - \sqrt{\frac{v_t}{b}}\right) \quad (3)$$

### 1.3.4 Other properties

The rest of the interesting properties is summed up here. The effective elastic modulus or strain modulus corresponding to  $\sigma = E\epsilon$  in the viscoelastic ice, is not the same as Youngs modulus or Elastic modulus as strain is not purely a result of displacement within the ice lattice. The strain modulus found from Hooks law ranges from 1-5 GPa and increases with increasing loading rate,

and is about 5 % lower for old ice [Timco and Weeks, 2010]. The effective Poisson ratio ranges from 0.8 to 1.2 in horizontal direction and 0 to 0.2 in the vertical direction, meaning it deforms more in the direction perpendicular to the columnar grains. The critical crack intensity factor for opening mode  $K_{Ic}$ , is about  $115 \text{ kPa}\sqrt{\text{m}}$ , but it is indicated that there might be a size factor since larger values were observed for bigger samples. Shear strength is 400-700 kPa for granular ice and 550-900 kPa for columnar ice, but lower when the fracture plane is parallel to the columnar grains.

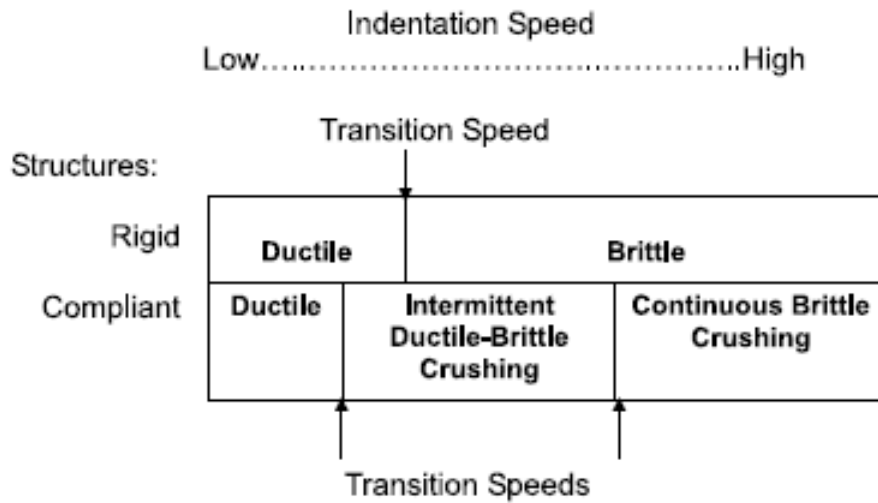


Figure 4: Ductile- brittle transition tendencies Failure mode as a function of speed and compliance of structure [Sodhi, 2001]

## 1.4 Failure modes

Ice may fail in many different ways depending on the geometry of the ice, geometry and compliance of indenter, indentation speed, strength, orientation and structure of the ice and confinement. From a global perspective, considering a vessel with an inclined bow advancing into the ice, the vessel will, in the case of thick ice, first slide onto the ice, and the failure commences with crushing, which will be treated thoroughly in subsection 1.4.1. The bow acts on the ice with a horizontal and a vertical component. As the crushing area increases, the vertical load will build up until it exceeds the flexural strength of the ice, and it fails along the grain boundaries through the thickness of the ice. This occurs a distance into the ice, where a stress concentration develops due to a local flaw. Seen from above the vessel will cause radial and circumferential cracking. Typically a piece that is broken off will have the form of a cusp - a half moon shape. This will further rotate, submerge, and slide along and under the ship. Left on the ice edge is a wedge. As the vessel advances, this will lead to a narrow but increasing contact where the ice fails in crushing, until a new bending failure occurs. This process can be seen in Appendix F, which shows snapshots of a video recorded by the author on an expedition with MS Husvik Supporter winter 2013. From a resistance point of view, the forces are commonly divided into crushing, bending and rotating, submerging and sliding. In really thick ice, 2m, cleavage can occur, a brittle failure across the grain boundaries longitudinally into the ice. For very slow indentation speeds, ice acts ductile, whereas for higher indentation speeds and vertical structures, continuous brittle crushing occurs. Global ice loads are important in predicting resistance and collision forces in ice and for the response of the ship beam. Dimensioning of frames, stiffeners and plate thickness is a concern of local ice pressures, where crushing is responsible for the highest pressures.

### 1.4.1 Crushing and high pressure zones

Crushing can be described as compressive ice failure, and is when the result of the interaction is small spalls and powderized ice. Crushing is governed by compressive strength, which can be very high, especially under high confinement. It can cause very high local pressures, up to 70 MPa [Frederking et al., 1990], as well as critical loads. The former is especially true for compressive ice loads acting on a long vertical midship, where the interacting area can

be large, and these loads may dominate the design of the midship structure. For higher impact rates the loads are known to act mostly along a narrow line smaller than the ice thickness, and also smaller than the nominal contact height, with localized peak pressures along it, fluctuating rapidly spatially and temporally. These peak pressures are believed to be the center of so called high pressure zones, hpzs . Wells et al. [2011] distinguishes between fracture and damage in compressive ice failures. Fracture is defined as distinct events typical for brittle failure, typically spalling, where local cracks propagate to a nearby free surface. Damage refers to micro structural modification, and includes local pressure melting, micro cracking and dynamic recrystallization. Rubble from the crushed ice containing small spalls and powdered ice is pushed both up and down. The buoyancy of this rubble from the underside, and the gravity of the rubble from the upper side, contributes to a confining pressure. Close to the edges small spalls will occur driven by high shear and closeness to a free surface. In areas of low confinement, but closer to the hpz micro cracking is prevalent, driven by very local tensile stresses, which are soon arrested by higher pressure. At the center of hpzs, there is dynamic recrystallization and pressure melting due to high pressure. Dynamic recrystallization is a dissipative process, forming finely grained ice that is stronger than the initial ice. This ice is still damaged by definition, and can be seen afterwards as zones of clear blue ice, opposed to rest of the ice which appears white. Pressure melting is a thermodynamically reversible process and starts in the grain boundaries. The three processes of micro cracking, recrystallization and pressure melting all happens close to the indenter or structure and is referred to as the damage layer. On the sides of the hpz, micro cracking leads to a softening of the layer. The more it cracks the softer it gets, and the pressure is localized into the center, forming the high pressure zone from recrystallization until the onset of pressure melting contributing to a total loss of bearing capacity of the layer, which leads to an extrusion event, ejecting the rubble, also called crushing event. Wells et al. [2011] also indicates that the cyclic loading, the known saw tooth behavior of force time series, are not only due to spalling events, but also crushing events, or combinations of these. It is further argued that the study of hpzs could be studied in small scale if only damage process is present, based on the argumentation that damage is a scale independent process, as opposed to fracture that is scale dependent. This is encouraging for the results of the test considered, as it is compression acting on a vertical midship, promoting crushing, and at low indentation speeds, which promotes damage rather than brittle fracture.

## 1.5 Previous work

### 1.5.1 Full scale measurements

Enkvist et al. [1979] performed long term measurements on IB Sisu from 1978-1979. A total of 500 000 impacts were recorded, with an average of 3.3 impacts per minute. Daily maxima was found to fit a Gumbel distribution. Measurements on I.B Sisu were continued to 1982 with strain gauges and ice gauges of diameter 200 mm at various locations, in addition to speed recordings Riska et al. [1985]. Loading as long as 4.8 meters were observed (2 spacings).

The icebreaker CANMAR Kigoriak was monitored using strain gauges on plating, longitudinal framing and web frames while impacting thick ice in 1981 and 1983. Accelerometers were mounted in bow, aft and on the bridge. The loads were found using finite element method (FEM) calibrations. Based on 157 + 240 rams a pressure area curve was presented [Ghoneim and Keinonen, 1983]. Analysis of IB Sisu data by Kujala and Vuorio [1985] reports that 67000 ice pressure peaks measured over 234 days year 1978-1979 fits a log-normal distribution, but comments that Gumbel extremes are more reliable for limited amount of data. Durations of peaks were on the order of a few hundred milliseconds.

MV Arctic was monitored during June, 1981 and 1984. Strain gauges measuring the dynamic hull girder and camera observing the indentation into large ice features and accelerometer readings were recorded. Using the bow print and global load pressure area curves could be obtained. 142 rams were recorded [Masterson and Frederking, 1993].

In 1987 the research vessel Polarstern was monitored using triaxial force transducers under Arctic conditions. It was found that loads were more concentrated than evenly distributed along a line. The ship had permanent deflection below the ice strengthened region [Müller and Payer, 1987].

IB Sampo was equipped with a 50 cm diameter window in the ice belt, 34 pressure gauges and a high speed camera. A line like load region with pressures up to 50 MPa were observed. Typical duration of an event was 50 ms, and an average pressure of 1.5 MPa. A Gumbel 1 distribution was fitted to the data [Riska, 1991].

A load panel of 0.9 m x 1.35 m was installed on the cutter MV Uisko in 1988-1989 measuring normal and tangential forces while sailing in the Baltic. The panel was calibrated by FEM. Short term measurements were collected

with 400 Hz, in addition to long term every 4 hours (81 samples). Maximum load was found to 694 kN [Kivimaa, 1993].

RV Akademik Fedorov measured pressure, stress and reaction of frames when sailing the Northern Sea route (NSR) during summer 1994, and data from interaction with 11 ice massives were recorded [Stepanov et al., 1995].

Oden and Louis St. Laurent transited the North Pole in summer 1991 and 1994 respectively. Louis St. Laurent was monitored on an area of 7.2m x 3m, consisting of 30 sub panels, each 1200mm x 600 mm. On Oden an area of 8.5m x 3m over 8 frames were monitored, consisting of 32 sub panels each of 850mm x 770 mm, in addition to hull girder strain. Loads were obtained using shear differences on frames and FEM for both vessels.

The chemical tanker MS Kemira sailing in the Bay of Bothnia was monitored in a bow, midship and aft frame during winters 1985-1988, using the shear difference between upper and lower part of frames, and calculating loads from FEM and beam theory. 12 hour maximum were gathered and used to fit a Gumbel 1 distribution to the long term maxima [Kujala, 1995].

USCGP Polar Sea and Louis St. Laurent transited the North Pole in tandem in 1994. 8 different compact trials was performed with Polar Sea, from 1982-1986. On the Polar Sea a total area of 9.1  $m^2$  was monitored, consisting of sub panels of 0.152  $m^2$  each.

MT Uikko and Kapitan Dranitsyn was monitored using strain gauges during the Arctic Demonstration and Exploratory Voyage (ARVDEV) from Murmansk to Ob Bay in spring 1998. On Kapitan Dranitsyn, 24 sub-areas were measured, of sizes between 0.05  $m^2$  and 0.77  $m^2$ . FEM calibration was used, and  $\Gamma$  and exponential distribution was fitted to the data in order to predict return pressure [Timofeev et al., 1999]. From MT Uikko strain was recorded every 20 minutes from bow, shoulder, mid and aft gauges [Kotisalo and Kujala, 1999].

The Molikpaq caisson structure outside Shakalin Island was monitored with ice load panels 2m x 1m, strain gauges, extensometers and accelerometers. Global ice loads were recorded and reported by Weiss et al. [2001].

During the trials of USCGC Healy in spring 2000 the forward shoulder was monitored using difference in upper and lower strain gauges on 10 unsupported frames, and using FEM for load calculations. Impact events were triggered by a threshold value. 1800 impacts were recorded [St. John et al., 2001].

Short term load measurements were conducted by Uto et al. [2005] on the icebreaker PM Teshio in the South Sea of Okhotsk in 1999. Strain gauges

were monitored on 6 frames, and load calculated by means of FEM.

The Canadian coast guard vessel CCGS Tery Fox impacted ice features from growlers to icebergs outside the northern tip of Newfoundland in June 2001. The experiment is referred to as the Bergy bit impact trials and the vessel impacted features from 100 to 22 000 tonnes [Gagnon, 2008]. The vessel was monitored by two load sensing systems, one external impact panel covering an area of 1.4 m x 2.4 m consisting of independent sensor areas of 18 x 18 mm, and strain gauges mounted between frames covering an area of 2 m x 2.8 m, with each single sub panel covering an area of 0.08  $m^2$  [Ritch et al., 2008]. The loads from the strain gauges were obtained by calibration from a finite element model of the monitored area.

KV Svalbard was equipped with 66 fiber-optic strain sensors at upper and lower part of frames in the bow and midship during winters 2007-2008 in Barents Sea. FEM was used mainly to determine the area affected by the observed load.

The Japanese coastguard vessel PV Soya was monitored using strain gauges one week in February from 2005 to 2009 sailing in Sea of Okhotsk. More than 10 web frames had gauges measuring shear strain over and under the ice loads, using the difference to calculate the load. Segments of constant speed and similar ice conditions were separated, and peak over threshold method was used to obtain statistics and fitting an exponential distribution [Matsuzawa et al., 2010].

Global ice forces were measured on the icebreaker Kapitan Nikolaev in the Barents Sea in 2008. Ice features were of 3200 tonnes to 300 000 tonnes. Information on the ice feature is first gathered, then linear and angular motions and accelerations of the ship were recorded during the impact to obtain the global load. Impacts lasted from 20 to 170 seconds [Krupina and Chernov V, 2009].

The cargo ship MT Uikko was monitored with 61 strain gauges measuring shear differences on frames. Short term maxima were recorded with 10 minutes intervals and loads were obtained using FEM. Weibull distribution proved the best fit [Kujala et al., 2009].

### 1.5.2 Model scale experiments

Kujala et al. [1993] performed compressive ice test on a model in the VTT (Technical Research Center of Finland) ice tank. The ice sheet was pushed against a moving ship hull, and against a pusher plate with a window. It

was observed that the process was strongly dependent on the frame angle and friction coefficient.

A 1:20 model of the Japanese icebreaker Soya was equipped with tactile sensors at bow and midship, consisting of 44 x 44 cells covering an area of 210 mm x 210 mm each. The model ice was doped with propylene glycol and bobbles for density, and had a columnar structure. The bow area showed an elongated load distribution, while the midship area was more round. Sum of the longitudinal compounds corresponded well with the resistance [Izumiyama et al., 2001].

2 models, scale 1:31, equipped with tactile sensors 44 x 44 cells covering an area of 239mm x 239 mm were tested in compressive ice in Aalto ice tank. The model ice is ethanol doped with small granular grains. Events producing a peak load for the entire sensor was analyzed. The experiment had similitude in Cauchy and Froude number and data was scaled according to this. An exponential distribution was fit to peak loads, although proved conservative for higher values. A pressure area curve was proposed and compared to full scale tests [Kujala and Arughadhoss, 2012].

### 1.5.3 Discussion of analysis of historic data

Considering subsection 1.5.1 it is understood that measurement methods and sampling techniques differ. Some, like on MV Arctic the hull beam strain is measured to obtain the global load acting on the ship from an ice feature, and knowledge of the bow and ice feature form in addition to indentation to obtain the contact area. Many others, like Soya, Kemira, KV Svalbard, MT Uikko and more use the difference in shear strain of gauges mounted on the upper and lower part of a frame, and/or strain gauges on other strategic places to calculate the load using Finite Element Method, and/or beam theory. However, Kujala and Vuorio [1985] points out that "the real contact areas are, however, difficult to evaluate by pure response measurements as a great number of pressure-area configurations can cause similar structural response". Also global loads, and loads acting close to but outside the monitored area can affect the strains. Further, the total size of area monitored, and the coarseness of the sensing matrix/size of sub-panels differ. Different types of external pressure sensing panels have also been used, the MEDOF panels, each 1.135m x 2.715m applied in different configurations around the Molikpaq [Jordaan et al., 2010], acrylic strip sensor applied in CCGS Terry Fox [Gagnon et al., 2009], and an ice pressure gauge of diame-



ter 200 mm made by VTT installed on IB Sisu [Kujala and Vuorio, 1985] to mention some. Another method is identifying the mass of the ice feature to be rammed first, then measure linear and angular accelerations and motions during impact to obtain the load [Krupina and Chernov V, 2009]. On top of it all, the observation frequency and length of time of observations differs a lot.

In the light of the different measuring procedures it should not be surprising that also the methods for data analysis differs between authors. Sampling methods, possibly event definitions to sample from, area definitions, time perspective, and eventually pressure-area relations differs. Most recordings contain a large number of observations, in most cases all of these are not presented together, but some sampling procedure is used to present extreme distributions, or for use in pressure area curves. Many authors have used the max event method described by Jordaan et al. [1993], where an event is defined as a collision or ram, and the maximum pressure or load within the event is sampled. Li et al. [2010] defines an event as all triggered sub panels at one sampled time instant. Others have used a similar approach were a maximum value is sampled from time intervals or time window [Kivimaa, 1993], [Kotisalo and Kujala, 1999], [Kujala et al., 2009] [Suyuthi et al., 2010]. Jordaan et al. [2010] also distinguish between global and local events, see Figure 5, where global interaction event is defined as "a single ice-structure interaction corresponding to a distinct movement of a multi-year floe", and a local event is within the time of a global event, and within the global area, and is triggered if the pressure is above a certain threshold, and ended if it is below the threshold for a certain amount of time. Another definition of event is from Daley [2004] where an event is triggered by a threshold, and always recorded from 1 second before to 4 seconds after the trigger. Other methods to sample is the Rayleigh separation method and up-crossing method, also called peak over threshold used by Li et al. [2010] and Suyuthi et al. [2010]. For Rayleigh separation a value is chosen below 1. After finding a first peak, a new max will not be found before going under the separation value times the last max, or an absolute lower threshold value. The last max will be abandoned if a higher max is encountered before going below separation value times last max. Kujala et al. [2009] uses this procedure on MV Uikko with a separator of 0.25. Differences is also found between full scale data in the sense that some seek special kinds of severe ice features for the test [Gagnon et al., 2009], [Krupina and Chernov V, 2009] while other measure loads while

in normal shipping [Kujala, 1995] or during a special voyage, for example like USCGP Polar Sea and Louis St. Laurent transferring the North Pole in 1994.

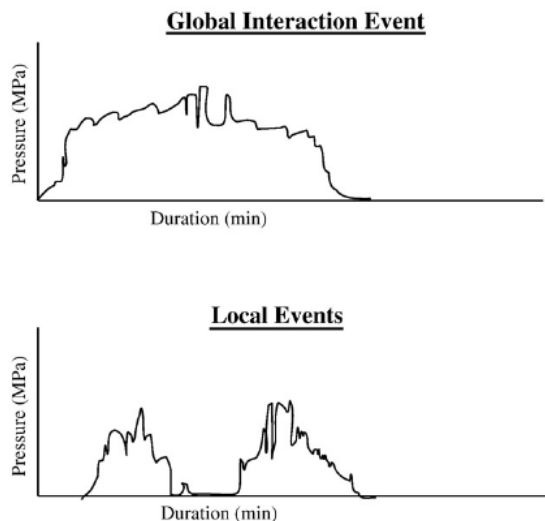


Figure 5: Illustration of global and local event definitions by Jordaan et al. [2010]

When it comes to area definitions, Jordaan et al. [2009] refers to measurements of hull beam strain like in the case of MV Arctic when defining global interaction area as "the area resulting from the projection of the structure onto the original shape of the ice feature". This area may include zero pressures from spalls, and may be found from knowledge of the geometry of the bow and the ice feature and the indentation into the ice, or a camera. The global area is also termed the nominal area by Jordaan et al. [2009], and increases as indentation increases during an impact. Jordaan et al. [2009] also defines a local area as areas within the global interaction area, such as plating between frames, a defined panel or other area interesting for local design. This area is fixed and does not change in size or position during interaction, but is defined by the local monitored area. Frederking [1999] defines the contact area as sub-panels of the monitored area experiencing a pressure over a threshold, giving a lower area and higher average pressures. Jordaan et al. [2009] later warns against this kind of procedure. Daley [2004] takes the measured contact area to be equal to the nominal area.

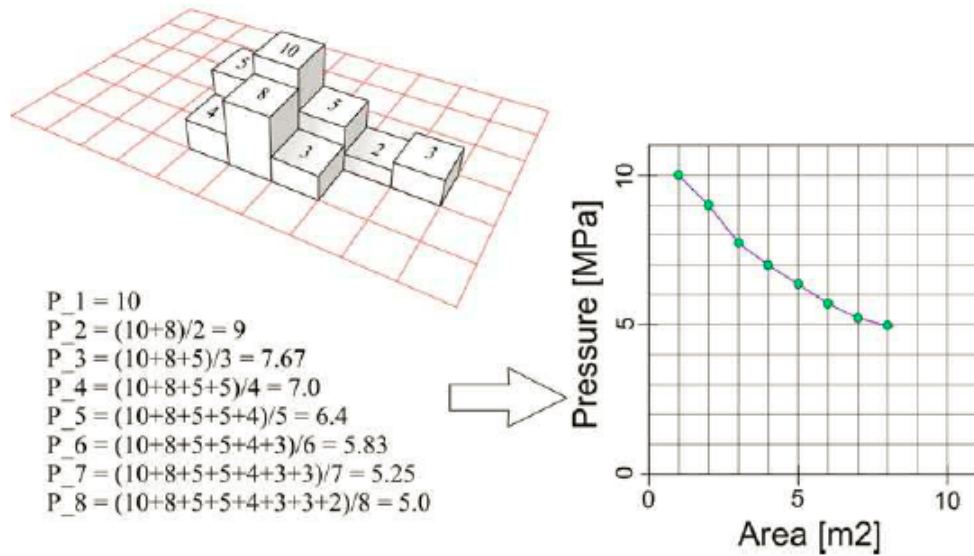


Figure 6: Method for making of spatial pressure area curve given for one time instant by [Daley, 2004]

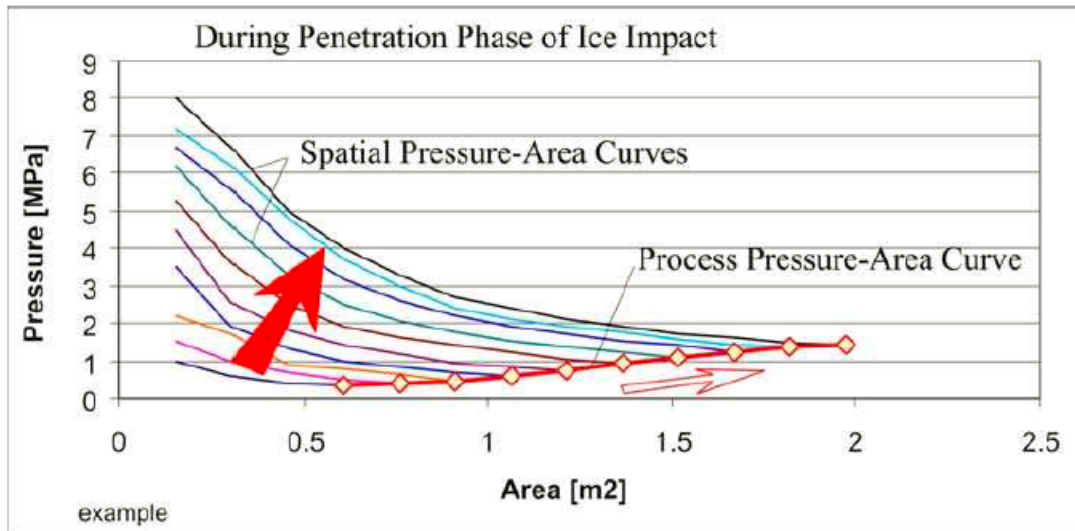


Figure 7: Link between spatial curves, and process curve by [Daley, 2004]

The definition of area is closely related to the different pressure area relationships. Based on his definition of global and local areas Jordaan et al. [2009] defines the global and local pressure area relationship based on average pressure over the respective area. Daley [2004] distinguishes between spatial and process pressure area relationship. The spatial relationship considers measured sub areas of the total contact area at one time instant. The making procedure is described as a group of connected pressures, where the highest peak over the associated area is the first point, and subsequently next highest pressures are added for increasing associated areas, as described in Figure 6. Note that all pressures are connected, but next not necessarily adjacent, as with  $P_7$  where one of the values (the last, value 3) is separated by the lower value 2. While Daley [2004] not explicitly states that sub areas for the spatial method have to be adjacent, but collects the subsequent highest pressure, Frederking [1999] defines the area used for his spatial relation as adjacent sub-panels that can be grouped in various combinations, still at one instant in time. The process pressure area relationship is an average pressure over the total measured area, and Daley [2004] and Frederking [1999] use this relation over a short time interval, typically to describe a ram, a collision or other interaction event. Frederking [1999] interprets Jordaan's local and global relationship as Daley's spatial and process relationship respectively. Note that the spatial and process relationships considers only the monitored area, although there may act forces outside of this area. Daley [2004] points out that spatial and process are not equivalent to local and global relationships, but "rather spatial and temporal trends of pressure". Daley [2004] and Frederking [1999] presents pressure area relationships for data gathered from one event, while data can also be gathered from longer amount of time, for example maxima from events over a long term measurement. Long term measurements would be more suitable for design for all areas, while relationships describing an interaction event is more suitable for scientific research of failing process and spatial distribution. As Frederking [1999] states about his process analysis "more impacts have to be analysed before a general process pressure-area can be proposed, and about his spatial analysis "many more events will have to be analysed before there are results suitable for design". Before the pressure area discussion begun in the literature, Sanderson [1988] published a pressure area curve consisting of extensive amount of data. The maybe most famous early pressure area relationship was presented by Masterson and Frederking [1993], consisting of a wide amount of data from borehole jacks to full scale ship ice interaction,

with corresponding wide amount of measuring methods and area definitions. The first design curve proposed was  $p = 8.1 \cdot a^{-0.5}$ , and was adopted by API and CSA. The revised curve is based on the average + 3 standard deviations and is  $p = 7.4 \cdot a^{-0.7}$ , and is implemented in ISO19906, and can be seen in Figure 8.

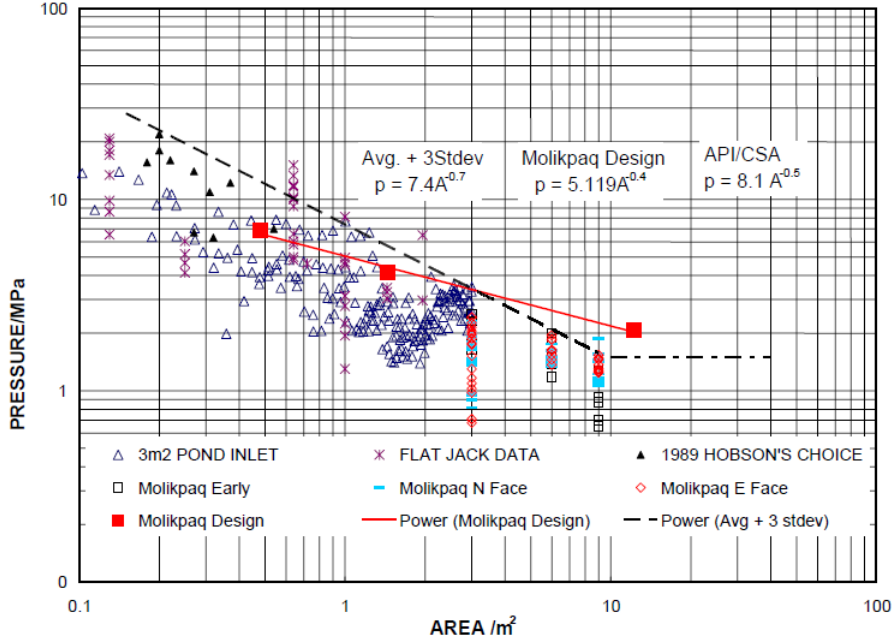


Figure 8: Pressure area curve adopted from [Masterson, 2007]

$$p = k \cdot a^{-n} \quad (4)$$

Relationships termed global, local and spatial are all agreed to follow a relationship as described by Equation 4, while there are still some discussion on the process curve, where it has been observed to rise slightly or has no specific trend for impacts and other short events [Daley, 2004] [Frederking, 1999], or follow a relation as in Equation 4 for others. Instead of pressure area relationships, some present pressure aspect ratio relations. This is interesting because larger aspect ratio gives less confinement. Ice is known to act in a elongated contact line, and so area and aspect ratios are connected, and

pressure aspect ratio relations show same tendencies as pressure area curves. This phenomenon of decreasing pressure with area is commonly referred to as the size- or scale-effect. There are two widely accepted reasons for this; probabilistic averaging, and fracturing. First note that the nature of the pressure distribution within a contact area is characterized by localized very high pressure peaks, surrounded by a larger area of lower pressures. Probabilistic averaging is clearly a reason in the case of a spatial pressure area relationship, as local high peaks in sub areas cause high average pressures, whereas this decreases rapidly as larger areas dominated by smaller pressure are also included. Fracturing, in the form of spalls leading to a smaller actual area than what is accounted for in the global method, can explain the relationship in the case of a global approach. But also for a spatial relationship fracture can be part of the explanation, as one can not expect a small sample to have the same number of flaws as a larger sample, but the size of the flaws may still be the same size for a smaller sample of the same ice. As opposed to damage, fracture has inherit scales effects, [Wells et al., 2011] as described in subsection 1.4.1.

## 1.6 Most relevant literature

Jordaan et al. [1993] developed a method to predict local pressures given an exceedance probability, based on gathered local area statistics from USCGC Polar Sea and MV Canmar Kigoriak, for fixed local areas of various sizes, depending on the data set. Data is sampled from events defined by discrete impacts, and a shifted exponential distribution is fitted, given in Equation 13. Each dataset is ranked and plotted against the logarithm of  $\frac{i}{N+1}$  where  $i$  is the rank, and  $N$  is the total number of samples in the set. The method is called the maximum event method. Taylor et al. [2010] continues this work, analyzing more datasets, and describing explicitly methods for adjusting for exposure of different kinds. Especially when sampling from sub areas within a larger area, exposure is adjusted for by changing the plotting position to that in Equation 5, where  $m$  is number of panels exposed. Different parameters  $\alpha$  and  $x_0$  for the fitted distribution is obtained from each data set, based on different fixed areas. This gives an area dependency for the parameters, and  $\alpha$ -area and  $x_0$ -area curves can be plotted and applied in design. The tendencies for the  $\alpha$ -area curve is negative exponential as seen in Figure 9. In Figure 10,  $x_0$  values adjusted for exposure is presented. The  $x_0$  values adjusted for exposure starts very low for small areas, and goes towards zero

for higher areas. Before the values were adjusted for exposure they were mainly over 0, somewhat higher for small areas, but also here going towards zero for higher areas for all data sets [Taylor et al., 2010].

$$\frac{i}{m \cdot N + 1} \quad (5)$$

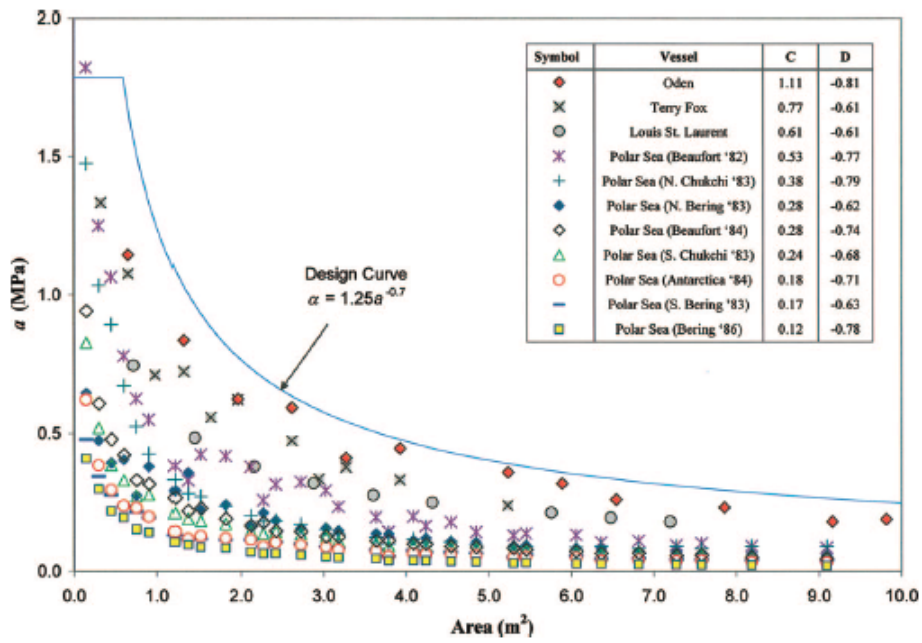


Figure 9:  $\alpha$ -area curves by [Taylor et al., 2010]

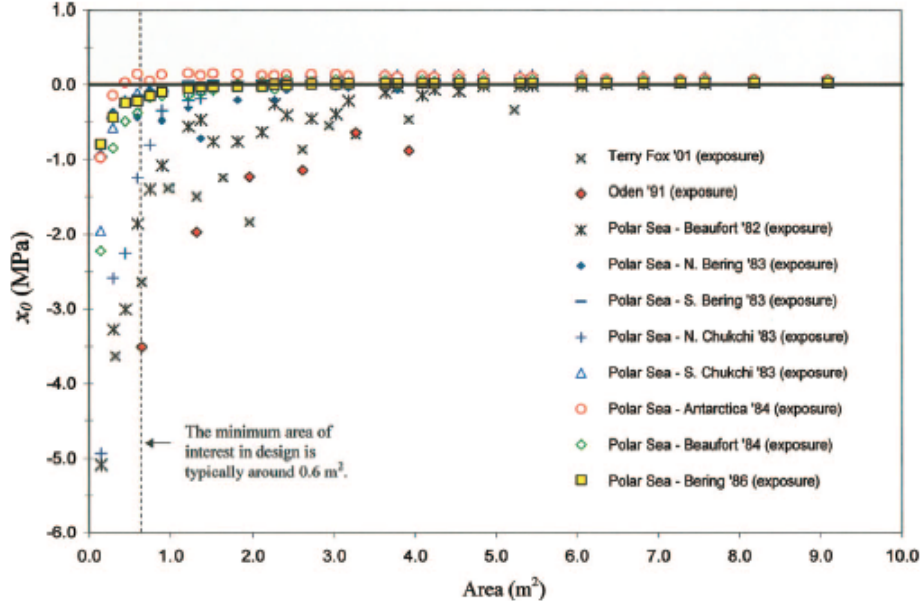


Figure 10:  $x_0$ -area curves by [Taylor et al., 2010]

### 1.6.1 Compressive ice and damages

When wind and or current is present it acts with a drag on the ice pack. The drift of the ice is about  $28^\circ$  clockwise of the wind direction, and about 2 % of the wind speed [Eriksson et al., 2009]. If a boundary is present in the direction of the ice drift, the coverage is increased to 100 % before pressure starts to rise in the ice sheet. The internal pressure in the pack is limited by rafting, which occurs at point contacts between floes, and subsequently ridging. If the pressure acts normal to the path of the ship, the resistance can increase drastically, and if the vessel stops, loads acting over a long part of the midship can be severe, leading to large plastic deformations. Compressive ice pressures have been shown to act along an elongated line [Riska, 1991], with contact like a mountain range, and peak pressures fluctuating rapidly spatially and temporally along the line.

Kujala [1991a] reports 5 ships that were damaged due to compressive ice, and more ships with damages in midship region that could be because of compressive ice. Some of the damages might have occurred before the years of the study. Typical damage at midship were buckling of web frames, yield



of frames and plastic deformation of plating. The most severe case was the ship named ship 39, a 7885 dwt bulk carrier that got stuck in compressive ice outside Luleå 18th of April 85. The maximum deflection was 500 mm with a length of 15 m. The ice condition and the resulting damage can be seen in Figure 11 and Figure 12. Hänninen [2003] reports that 15% of the damages in the study occurred in compressive ice field. A tugboat was reported drifting stuck in the compressive ice, suffering deflection of 10mm-30mm of frames, buckling of brackets and broken pipeline. Also a 95 000 dwt oil tanker got stuck in compressive ice, with ice piling up the side, causing permanent deflection over 100 m with a max of 30 mm deflection.



Figure 11: Ship 39 stuck in compressive ice [Kujala, 1991a]

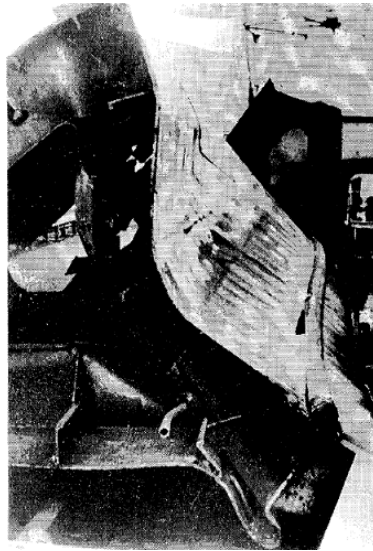


Figure 12: Ship 39 deflection after compressive ice [Kujala, 1991a]

## 1.7 Regulations

Regulations for vessels going in ice are mainly concerned with global and local structure requirements for ice loads, winterization, resistance and propulsion power in addition to some other special system requirements. Only local strength requirements will be covered here, for Finnish-Swedish Ice Class Rules (FSICR), and requirements from Det Norske Veritas (DNV), which also have included the International Association of Classification Societies, (IACS) unified polar class rules, is presented in Appendix A.

### 1.7.1 Finnish-Swedish ice class rules

The ports of Finland are icebound in winter, and to keep the economy going one can understand that they were pioneers in ice, and early to implement design rules. They were mainly concerned with propulsion power, and in the beginning the design height was taken to be the ice thickness, and required structural dimensions were a function of installed power and displacement [Kujala, 1995]. Local damages were observed every winter, and this was the driving factor for reducing the nominal height, and as a result, the design pressure increased. There are 4 classes, 1A Super, 1A, 1B and 1C, from highest to lowest requirements. The requirement for thickness of plating is

different depending on the framing system. The requirement for thickness of plating has two terms, where the second is addition for corrosion and abrasion. The first term is a function of spacing, yield strength, design ice height for the different classes and design pressure. The latter may be the most important parameter here and is presented in Equation 6.

$$p_{design} = c_d \cdot c_1 \cdot c_a \cdot p_0 \quad (6)$$

The design pressure is composed of different factors multiplied by the nominal ice pressure,  $p_0$ , which is set to the constant 5.6 MPa.  $c_d$  is a factor taking into account the size of the vessel, engine output and the hull region. Hull regions are forward, midship and aft. The factor  $c_1$  takes into account the occurrence of design pressure in certain regions of the hull, and is a function of the target class, and the mentioned region.  $c_a$  takes into account the probability that the full length of the area under consideration will be under pressure at the same time, and is a function of what structural member is considered, for example stiffeners of web frames. FSICR considers elastic design requirements, so that yield is the limit, which is more conservative than plastic design requirements. Failure modes considered are shear and bending, in addition to buckling. The design scenario is 1000 days [Riska and Kämäräinen, 2011]. This leads to requirements for section modulus and shear area for different structural members. Formula for required section modulus depends on the framing system (transversal or longitudinal). Generally it is a function of pressure given in Equation 6, framing system, height of contact area (function of class and hull region), span of member, yield strength, and a factor taking into account boundary conditions. Required shear area is a function of design pressure, design contact height of the ice, spacing of the relevant member, and a factor taking into account load distribution to adjacent members. It can also be mentioned that it is stated that the methods are based on full scale observations in the Baltic, that would be damage statistics. It is also interesting to observe that the stiffness variations between plate and frames is taken into account, leaving a design pressure that is lower in more compliant areas like between the frames, consistent with Figure 4.

## 2 Model scale experiment

Model scale experiments in model ice basins has been done a long time already, and has proven a reliable way to predict resistance in level ice, in order to install a suitable size engine, and also breaking patterns. It's still a challenge to predict local ice loads in that ice is a very complicated material and the failure modes depends on many aspects. First of all, these aspects needs to be identified, and similitude between relevant ratios in full and model scale should be maintained. For this experiment, crushing will be an important failure mode since the ice sheet will be pushed against the vertical midship. Usually the ice is not scaled to satisfy similitude in any crushing parameter. More about the experiment and scaling follows.

### 2.1 Description of experiment

The experiment was a part of the EU FP7 project called SAFEWIN, and took place in Aalto ice tank. A thorough description of the experiment is given in Suominen and Kujala [2012]. The model was of the general cargo ship, "Credo", which is applied in the Baltic sea. Specifics about Credo is given in Table 1. Credo also has a long vertical midship which promotes crushing. The basin in Aalto ice tank is 40x40 m and 2.8 m deep. The basin has a bridge extending from side to side of the basin which is able to drive along it. Under the bridge there is a carriage able to run the length of the bridge, being able to reach all point of the basin. The compressive ice is made by attaching plates to the bridge, pushing the ice sheet at a speed of 0.02 m/s towards the model and the broken channel. The Russian system of observing compression is based on the distance the ice closes after the ship. In mild compression it closes 0.75 nm after the ship, and for moderate and severe after 0.5 and 0.25 respectively [Suominen and Kujala, 2012]. In the case of this experiment it would correspond to severe compression as it closes 0.166 nm after the ship, considering the speed of the model, ice velocity and breadth of model.

Table 1: General cargo ship Credo specifications

Credo spesifications	
Ice class	1 A Super
Deadweight	21353 ton
LOA	159 m
Breadth extreme	24.6 m
Draught	9.4 m
Depth	13.5 m

Table 2: Experimental spesifications

Experiment spesifications	
Ice thickness	29 mm
Compressive ice speed	0.02 m/s
Towing speed model	0.5 m/s
Geometric scaling factor	1:25

### 2.1.1 Scaling of model ice

The scaling of model ice in this section is based on informatioun gained from Timco [1984]. For complete similitude in model scale tests, geometric (linear dimensions), kinematic (velocities) and dynamic (forces) similitude should be preserved. This means that each of these properties needs to be scaled linearly, noting the geometric factor  $\lambda = \frac{L_p}{L_m}$ , the kinematic factor  $\lambda_k = \frac{v_p}{v_m}$ , and the dynamic factor  $\lambda_d = \frac{F_p}{F_m}$ , where subscript p is for prototype and m for model. The geometric factor is straight forward, and equals the kinematic factor just by choosing the correct speed, but for the dynamic (forces), there are more aspects. For the forces that are more dominant in the test in question, the similitudes needs to be preserved. In the case of crushing and a compliant structure, the dynamic interaction is important and the natural frequencies and modes should be preserved. In our case the model is not considered compliant. In normal ship model tests, gravity, inertial- and viscous forces is considered. Gravity and inertial forces are important for breaking of ice in the case of flexural failure. In addition, cracking forces of the ice should be considered, especially in the case of crushing, but this is seldom preserved. From similitude in gravitational forces one gets that  $\lambda_d =$

$\lambda^3$  since  $g$  is the same in both scales, assuming the densities of water is the same (although that is not entirely true here). The result is that forces scale with the geometric factor to the 3rd. Combination of gravity and inertial forces leads to the Froude number, inertial and elastic forces leads to Cauchy number, inertial and viscous to Reynolds number, and inertial and cracking forces leads to the ice number. Cracking forces is given in Equation 7, where  $R$  is as given in Equation 8 with a half crack length, and critical stress intensity factor as a function of  $R$  as given in Equation 9 and  $E$  elastic modulus [Timco, 1984]. This leads to the ice number shown in Equation 10 [Atkins and Caddell, 1974]. The ice number also incorporates the Cauchy number. Because it is realized that failing process of ice is largely governed by fracture, the characteristic bending length of floating ice is sought to scale as other geometric dimensions; linearly. The result is that the elastic modulus of ice has to scale linearly with  $\lambda$  and, combined with Cauchy that  $\frac{E}{\sigma_f}$  similitude is required [Palmer and Dempsey, 2009]. Further, to preserve the breaking pattern the number of grains over the characteristic bending length is preserved.

$$F_C^2 = \frac{2R}{\frac{d}{dA}\left(\frac{u}{F_C}\right)} \quad (7)$$

$$R = \frac{\pi\sigma^2a}{E} \quad (8)$$

$$K = \sqrt{ER} \quad (9)$$

$$I_n = \frac{v_p^2\rho_p}{K_p}\sqrt{L_p} = \frac{v_m^2\rho_m}{K_m}\sqrt{L_m} = (C_n)^2\sqrt{\frac{EL}{R}} \quad (10)$$

Due to problems with measuring critical stress intensity factor properly the ice number is not preserved in Aalto ice tank. Traditional Froude and Cauchy scaling is applied in addition to characteristic bending length (number of grains relate to structure dimensions). The resulting scaling laws is seen in Table 3. Usually the most important parameter is the bending strength, or for practical purposes flexural strength. This has first priority and is scaled correctly, but leads to a generally too little value of  $E$  and  $\frac{E}{\sigma_f}$ . This leads to a too "soft" ice but is considered sufficient. The way model ice is grown in Aalto ice tank is by spraying small droplets of ethanol

Table 3: Scaling laws [Timco, 1984].

Property	Scaling rule
Time	$t_p = \sqrt{\lambda}t_m$
Velocity	$v_p = \sqrt{\lambda}v_m$
Acceleration	$a_p = a_m$
Mass	$M_p = \lambda^3M_m$
Force	$F_p = \lambda^3F_m$
Ice strength	$\sigma_p = \lambda\sigma_m$
Ice thickness	$t_p = \lambda t_m$
Ice elastic modulus	$E_p = E_m$

Table 4: Possible scaling distortion

Property	Model	Target/Full scale	$\lambda$ , (target = 25)
E	70.2-60.4 MPa	4 GPa	57-66
$t_{ice}$	28-29 mm	700-725 mm	24-26
L	6.4 m	159	25
$\sigma_f$	27.2-31.7 kPa	500-625 kPa	16-23
$\sigma_c$	52-61 kPa	2-3 MPa	33-58

doped solution onto the cold water surface to obtain the right grain size. The spraying continues until the target thickness is reached. Then the layer is consolidated until the target strength is obtained. The longer it consolidates, the stronger it gets as more ethanol freezes, as the strength is a function of unfrozen ethanol. The measured properties on the day of the experiment is shown in Table 5 for two different locations in the basin, and in Table 4 the properties are compared to full scale target values, and resulting scaling factor presented. If the factor differs from the target value the scaling is distorted.  $\frac{E}{\sigma_f}$  values are in the interval 1905 - 2580 for model scale whereas full scale is in the range 2000-5000, a little too small, but acceptable within the limitations [Nakamura et al., 1983]. If the resulting  $\lambda$  in Table 4 is higher than the target it means the property is too little, and if it is lower than the target it means it is too high. The maybe most important factor in this test is the compressive strength, which is here too little. When scaling up the target value of 25 is used, but since the compressive strength that is governing the loads is too little, the results are expected to be too low.

Table 5: Tested ice values on the day of the experiment 18th of January 2012

x [m]	y [m]	$\sigma_f$ [kPa]	$\sigma_c$ [kPa]	E [MPa]	h [mm]
8	7	27.2	61	70.2	29
25	18	31.7	52	60.4	28

### 2.1.2 I-SCAN tactile sensor

The tactical sensor 5350N provided by I-SCAN is a thin and flexible sensor sheet consisting of a matrix of force sensitive variable resistor sensels. The information in this paragraph is based on Tek. The impedance of the sensels changes from above 10 M ohm with no loading, to less than 20 k ohm with full load. An analog to digital converter assigns a value between 0 and 255. The values are sampled on a row and column basis, and the scan rate should be about 5 times faster than the frequency of the events. The sensor comes with a software package, and manuals for assisting equilibration and calibration. Equilibration is a method of ensuring all sensels have the same sensitivity. This is done by applying an even load and adjusting the digital output, (DO), of individual sensels such that it is equal to the total average digital output. Calibration is the process of linking the DO to engineering units, by applying a known load and adjusting the total DO according to this. Using zero pressure and one applied load a linear relationship is obtained. When the range of pressures are close to the calibration load this is feasible, but when a wide range of pressures needs to be observed as in this test, a two load calibration should be performed in order to fit an exponential relationship, as the nature of the load versus output may not be perfectly linear in a wider range. Calibration should preferably be done with similar interface, shape and temperatures as in the experiment. Other than the temperature this is hard to perform with the model ice as the loads would largely be unknown.

In this test, the sensor was calibrated using 3 calibration points, 0, 20% and 80% of maximum. Maximum, or saturation pressure was 221 kPa. A linear response was obtained. Equilibration was not explicitly performed, but checked by observing even output over the cells when an even load was applied. Calibration was performed in the same temperature as the experiments.



### 2.1.3 Sources of error

In a late stage of the work, it was observed that a certain interval of time of the data with much higher magnitudes dominated the whole data set. It was only then found that the measuring system was turned on before the test started and turned off after the test ended. When the time of the whole set was divided in 10 intervals, the test was roughly run during the second and third interval. During the data processing the whole data set provided was considered. The loads collected outside the time of the real experiment was generally 10 times lower than those obtained during the actual test. These are still loads from the ice sheet, just not during compressive ice on a moving ship. Since the extreme loads are considered in this work, this is not considered a significant error here, but should be checked and corrected for further work.

As indicated in subsection 2.1.1 there might be some scaling distortion. Compressive forces are of significance in crushing, and compressive strength is lower than the target value, which may lead to too low values when scaled up according to the geometric target scaling factor. Only one run with the same physical conditions and test parameters were analyzed, and more runs leading to a larger statistical population may have an impact on the results.

Calibration was performed according to the Tekscan manual as far as possible, but not including loading with a similar shape and interface. Similar output of individual cells were checked, but not adjusted, so some sensitivity variation may be present. Noise is evident on the lower part of the sensor that was curved around the lower part of the hull, triggering sensels not subjected to any loads. Most of this was cut away during data processing, but not all. The frequency and magnitudes of these are low, and since extreme loads are of interest here, it is not important for the results. The sheet spatial resolution is quite high compared to similar full scale tests, but peaks still cover single cells, suggesting it could be even more local, but it is sufficient for local design. The frequency of observation is 100 Hz, but there is no evident rise or fall of pressure peaks. The Tekscan manual states that the frequency of observation should be at least 5 times the frequency of events, which suggests higher frequency, but this is more interesting from a scientific point of view, than for design based on statistics. The system

has a resolution of 8 bits, covering 255 values over a range of 221 kPa, leaving a lower threshold and intervals of 0.97 kPa which is within the limitations.

Finally, an independent load sensor cell was mounted in the hull behind the sensor sheet, leaving a cutout around it, resulting in two sensor columns without support, therefore showing falsely too low values. It may be added that crushing and compressive forces are still not very well understood, and that compressive model ice tests are not yet an established method to predict full scale loads.

## 3 Methodology

### 3.1 Motivation

The nature of the raw data from the Credo model test is a matrix of 48 times 44 pressure sensing cells that are observed every 0.01 seconds. The forces act mainly in an elongated central region, with pressure peaks along the line. The length and position of the line varies rapidly in time. Also the peaks varies spatially along the line and in time very rapidly. The line even sometimes totally disappear for some time, maybe leaving only a single triggered cell or a small group. Due to the variation, a continuous line can be splitted in several lines the next instant, and then may join or partially join the subsequent instant. Each line may change size and shape every instant, or completely disappear. This can be described as a semi continuous interaction, unlike clearly defined events as ramming, collisions or ice floe interactions that is separated in time, or continuous interactions with coarser areas, like transiting the North Pole that can be sampled by up-crossing method, Rayleigh method or similar sampling methods for continuous data. The data set in question has fine spatial and temporal resolution, and both expel semi-continuous behavior. Each of the cells could be considered as a sub area of a larger area, and a local design methodology based on Jordaan et al. [1993] could be applied on each of the cells, which are sub areas on a fixed location. Each cell corresponds to an areas of 27.28 cm times 22.91 cm in full scale that would be the area to design for. The consequence is that datasets of subareas the same size only can be used for local design of an area that exact size. By grouping adjacent triggered cells within the monitored area, larger sub areas than one cell could be considered. By doing

this design curves based on Jordaan et al. [1993] ( $\alpha$ -area and  $x_0$ -area from subsection 1.6) can be produced from this one single dataset. This further requires that an event out of the semi continuous data set is defined, in order to apply the maximum event method. This is solved by defining spatial and temporal events as described below. A method for adjusting for exposure is applied on larger sub areas than one cell based on the original adjustment by Taylor et al. [2010].

### 3.2 Sampling based on spatial and temporal event definitions

The maximum event method is described as "for each collision, the highest pressure on a single sub panel was recorded" [Jordaan et al., 1993], where the event is a collision. In order to sample max pressures, an event has to be defined, and retrieved from the dataset. To do this, a spatial event is defined as triggered sensels that are geometrically adjacent to each other, either left, right, up, down or diagonally. All groups of adjacent triggered cells, within the censoring sheet and for each time instant will be given a unique id number. Further a temporal event (time event), is defined as spatial events that are adjacent in time. The temporal event is not far from Jordaan's local event described in Figure 5, only it considers change in spatial distribution in addition. If any one of the cells in a spatial event is also triggered in the previous and/or next time instant, these spatial events will be assigned to the same time event. So that each time event is composed of one, or more likely, more spatial events. In the special case where the associated cells the next time instant are split in two, both the two new spatial events will belong to the same time event id . Also if two spatial events with each their associated time event, the next time instant are joined to one spatial event, the time event with more triggered cell in the previous spatial event will dominate. The method is illustrated in Figure 13. The result is that one time event will correspond to a collision, or the event to be sampled from in the maximum event method. Each temporal event has a certain id number, a duration, and an area that is changing with time. The samples for distributions are picked as the highest average pressure for a given area occurring during one time event.

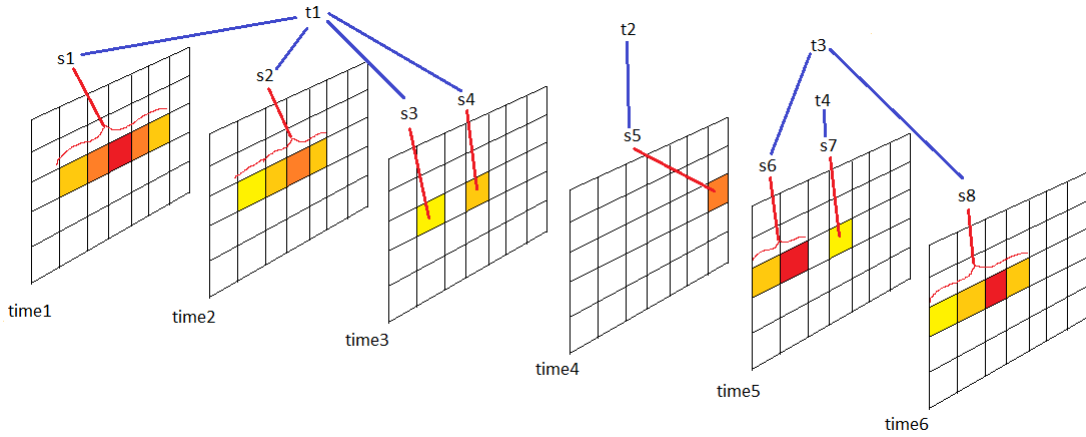


Figure 13: Illustration of spatial events (s) and temporal events (t) applied in max event method

### 3.3 Applied pressure area relationships

The spatial pressure area relationship used here is adopted from Daley [2004]. It is established for one time instant, and uses sub areas within and including the total contact area of a spatial event as defined in subsection 3.2. For  $n$  triggered cells within the spatial event contact area, the single greatest pressure will be plotted against the one single area corresponding to that monitored sub panel, or in this case, sensor cell. Then the second greatest pressure is found, and the average of the two biggest pressures are plotted against the area corresponding to their two sub panels. This continues to include the subsequently next highest in the average, and all the time plotted to the corresponding area, as described in Figure 6. In the method applied here the subsequent highest triggered cell in the spatial event is not necessarily directly adjacent, but always connected via the other triggered cells in the spatial event. One can argue that a better definition would be to find the combination of directly adjacent cells that would give the largest average for each area investigated, but this would lead to a very difficult sorting algorithm. Here we are satisfied as long as the subsequent highest is connected (within the same spatial event), which also will lead to conservative pressure estimates, especially for small areas. The sampling from spatial events instead of the whole monitored area is here new in the making of pressure area curves. Treating distinct groups of adjacent triggered cells as one area

although they are not connected seems wrong. Applying the spatial methodology on all time instants that are available in the experiment, and keeping only the highest pressure for each area, while disregarding the rest, a kind of local design pressure area relationship emerges. Based on this definition the term local pressure area curve will be applied from now on. As Jordaan's definition of local pressure area curves, it does consider sub areas of the total area, but instead of sampling from sub areas of different sizes to obtain the area dependence, adjacent sub areas are grouped to obtain pressures over larger areas from the same data set. It differs from the way Daley and Frederking applies spatial relationships in that they consider one event at a time, only short time periods, while here the whole data set is taken into account. The local pressure area curve can be used for design of local structural members with an exposed area according to the curve, where the design scenario is similar to the test conditions and area of hull considered. The process pressure area relationship used here is adapted from Daley [2004]. It deals only with the total contact area for each spatial event. It can be plotted over one time event in order to see how the pressure and area develops over a collision, or any other time interval in interest. If plotted over the entire experiment time and disregard all but the highest pressures for each area, a total contact area-average pressure relationship emerges. This differs from Jordaan's global relationship in that there might be pressures acting both outside the monitored area, and also in other spatial events inside the monitored area. It differs from the process relationship in that it considers the whole data set rather than just an event of a short time interval. The local pressure area relationship used here approaches the total contact area-average pressure relationship when the sub areas increases towards total contact areas.

### **3.4 Methodology for design of panel**

Design of a repetitive midship plate with one stiffener is based on a statistical approach as described by Jordaan et al. [1993] and Taylor et al. [2010]. A shifted exponential distribution is fitted to tail of the data gathered from different area sizes of the model test. The distributions are adjusted for exposure. Design curves are produced based on the area dependence of the parameters of the distribution. Based on the extreme pressure distributions, a load for the proposed structures is calculated. Using a design scenario and yield as design limit and applying existing stiffeners, scantlings are proposed

based on required section modulus. The proposed designs are also compatible with FSICR, and checked using Monte Carlo simulation.

### 3.4.1 Area distributions sampling

Distributions are collected for all area sizes using the max event method on temporal events, such that within each temporal event, the spatial event with the biggest average pressure over the area in question is sampled. This gives individual distributions for each area, from 1 cell up to 32, which is the largest amount of triggered cells found within a single spatial event. Sub areas of the spatial events are also considered, because the area one wants to design for may be exposed to a load acting also outside the design area of interest, and is therefore an internal area, possible experiencing a higher average pressure than the total interaction area, causing a corresponding higher load. When area sizes to gather distributions from rise, the population sinks, as total areas smaller than the one in question is omitted, and large interaction areas are fewer. As distributions for larger areas are based on small populations these are more uncertain.

### 3.4.2 Adjusting for exposure of internal areas of increasing size

Distributions can be presented in a Weibull plot, and in the case of one cell, adjusted for exposure as done in Taylor et al. [2010] and described in subsection 1.6. When applied here, the amount of exposed censoring cells is interpreted as numbers of cells that were ever triggered during the test, as the censor sheet extends far beyond the ice loaded region. This number is the same as number of red cells in Figure 14 which is 507, and equals  $m$  for exposure of one cell. As sampling for higher areas composed of more adjacent triggered cells within the total area is not done in previous literature, adjusting for exposure of these are not described. The variable  $m$  in Equation 5 used for exposure will here be expanded to use on larger areas, by defining it as: how many of the area in question there is room for in the total exposed area, or expressed by Equation 11. In practice the slope of the distribution in a Weibull plot will stay unchanged, while the intersection with the x axis will change. The adjusted curve is now standardized and is the one used for design.

$$m = \frac{\text{total amount of exposed cells}}{\text{nr of cells corresponding to the area in question}} \quad (11)$$

### 3.4.3 Statistics

The shifted exponential distribution in Equation 13 is a straight line in a Weibull plot. As only the highest values are interesting for design, the distribution is fitted to the tail in the plot, which contains the biggest pressures. Long term measurements has shown that a Gumbel1 distribution as in Equation 14 is a good fit [Kujala, 1995], and will here be applied for the extreme distribution shown in Equation 14. Here  $x_1$  is as in Equation 15 with  $\mu$  expected number of hits per unit time and the reference time is one year. Probability of exceedance  $P_e = 1 - F_x$  is shown in Equation 12. Given a return period  $F_z = 1 - \frac{1}{rep}$  the corresponding design load,  $z_e$  can be found from Equation 16.

$$P_e = e^{-\frac{(x-x_0)}{\alpha}} \quad (12)$$

$$F_x(x) = 1 - e^{-\frac{(x-x_0)}{\alpha}} \quad (13)$$

$$F_z(z) = e^{-\frac{(z-x_0-x_1)}{\alpha}} \quad (14)$$

$$x_1 = \alpha(\ln(\mu)) \quad (15)$$

$$z_e = x_0 + \alpha\{-\ln[-\ln(F_z(z_e))] + \ln(\mu)\} \quad (16)$$

### 3.4.4 Design curves

Design curves are more specifically  $\alpha$ -area and  $x_0$ -area curves, where  $\alpha$  and  $x_0$  are parameters in the shifted exponential distribution, see Equation 13. This is called design curve, because the area that is monitored and collected data from, may be different from the area that needs to be designed for. Hence from the design curves, based on the desired design area, the correct  $\alpha$  and  $x_0$  to be used in the distribution can be found. Viewed in a Weibull plot the exponential distribution is a straight line, where  $\alpha$  is the inverse slope,  $slope = \frac{1}{\alpha}$  and  $x_0$  is the intersection with the x-axis. For each of the individual area distributions there is a corresponding  $\alpha$  and  $x_0$ . Both can then be plotted as a function of area and used for design.

### 3.4.5 Scenario

In order to design a structure based on the distribution obtained, one has to define a design scenario that the midship panel must stand. This should include how many days per year similar compression as the one in the test can be expected, and what should be the return period of the critical load. This should be based on an appropriate risk level. Risk of an event can be defined as the probability of the event times the consequence of the event. The event we will design for here is yield of the midship panel, and the probability that this will occur is based on the extreme distribution of the sampled pressures from the test. The severity is harder to predict. What could be the consequence of yield at midship during a compression event? At least repairs, which would be an economic loss. Could the deflection of the plate contribute to the vessel being screwed down by the ice? The more severe the consequence is, the lower should the probability of exceeding that design value be. The scenario that is defined for design should reflect the loads that the vessel is predicted to meet, and the proper safety level. Based on the prototype vessel Credo, which sails in the Baltic the example scenario for this thesis is set to 10 days a year in severe compressive ice and 100 years return period, corresponding to a probability of exceedance of 0.01, when the reference time of the distribution is one year. This scenario is just set as an example, but for any design it should reflect the design strategy.

### 3.4.6 Design procedure

The structural part that is designed for is a plate at midship in the ice region with a stiffener over the length of the plate. The dimensions of the plate is equal to span times spacing. Both longitudinal and transversal framing is considered. In the case of longitudinal framing the length of the plate is the span, and height is equal to spacing, and opposite in the case of transversal framing. The load is assumed to act over a height equal to one sensor cell height in full scale (0.2728 m) as it mainly does in the test, and the load length equal to the longitudinal length of the plate. The longitudinal length options are based on the area from the height and  $n$  integer times cell breadth, 0.2291 m. This gives an area based on the different area distributions.  $\alpha$  and  $x_0$  parameters are chosen from the design curves based on this area, to give the correct area distribution for each design case. Given scenario, span, spacing and weather it is longitudinal or transversal framing, the design



load can be found from Equation 16. The scenario includes days per year in ice and return period. Using beam theory where the stiffener with the plate flange, making out a beam, is assumed clamped, the corresponding moment and further the section modulus can be found from Equation 17 and Equation 18. The scantlings are given picking an existing Ruukki profile and a plate thickness according to FSICR or equal to web thickness (whichever is larger). Running this procedure for several inputs creates several possible designs, where one is recommended based on low weight per area and a simple qualitative cost measure. Inputs are choice of longitudinal or transversal stiffening, in addition to one of the area distributions.

$$M = \frac{PL}{8} \quad (17)$$

$$Z = \frac{M}{\sigma_y} \quad (18)$$

### 3.4.7 Monte Carlo

The design procedure is reversed in order to check the design. Assuming a normal distribution of steel strength, the mean (289.9 MPa) and standard deviation (22.36 MPa) is applied in addition to the area distribution used to design the structure [Kujala, 1991b]. In the Monte Carlo simulation the cumulative distributions are utilized. For each loop, two numbers between 0 and 1 is produced, one for the load distribution, the other for the structure strength distribution. These are fed into the representative cumulative distribution to produce a corresponding load and strength. The loop runs 10000 times, and strength and load values are saved each loop to simulate the distributions. An overlap between the distributions indicate a probability of failure. For each loop a margin is also produced from the difference between load and strength. From the resulting margin distribution the probability of failure can be found from the percentage of the area that is lower than zero. The goal is that the probability of failure is equal or smaller than the target value corresponding to a 100 year return period,  $P_f = 0.01$ .

### 3.5 Exposure

Both in data analysis and for design, exposure has to be taken into account. There are several aspects of exposure, both spatial and temporal, and all require some kind of action to adjust for this exposure, either for standardization in data analysis or to reflect the design scenario. Four aspects are pointed out by [Jordaan et al., 1993], and will be presented here. The first is spatial and related both to data analysis and design, where it is treated differently [Taylor et al., 2010]. In full scale measurements one or more panels corresponding to areas can be measured. If the data is sampled from more censoring sub panels, the distribution obtained must be adjusted to account only for one panel in the data analysis in order to get a standardized curve. This is more thoroughly explained in subsection 3.4.2. When it comes to design, an area different than the one corresponding to one monitored sub panel has to be considered. This is when design curves are needed, as explained in 3.4.4. For the area one wants to design pressures for, the parameters for the exponential distribution,  $\alpha$  and  $x_0$  corresponding to the desired area is picked in order to obtain the correct distribution. Notice that the  $x_0$  chosen should be adjusted for exposure during data analysis for each area as explained in subsection 3.4.2. The second aspect is a temporal one, namely duration of contact. The maximum event method always seeks the largest value within a continuous event, ram or collision. In some cases a vessel may go in hours and days continuously crushing ice, and in other cases many discrete collisions happens every minute, and in both cases the max for each one event is sought. According to [Jordaan et al., 1993] long durations tend to the Gumbell distribution, as opposed to shorter durations in which an exponential form has often proved a good fit. Also if the reference duration from the data set differs from what one would like to design for, this can be incorporated in the distribution using a factor that is the ratio of the design duration to the reference duration, see [Taylor et al., 2010]. The third aspect concerns which general area of the vessel the data is from, and which area that is to be designed for. Obviously the bow is subject to more severe loads than the midship, and keel less than midship, but aft maybe more and so on. Classification rules take this into account by applying area factors, with reference to one of the areas. The fourth concern of exposure is the frequency of impacts. For design this should be included in the distribution as a factor,  $\mu$ , see Equation 16, number of expected hits during a reference period, here set as one year. One last aspect of exposure is what kind of

environment, what kind of ice that is encountered. In High Arctic multi year ice and ridges are more common and will cause more severe loads than sub Arctic areas. In class rules this is dealt with using different ice classes.

### 3.6 Matlab functions

The raw material for the experiment is in the form of a .csv file, a comma separated file produced with the software that comes with the tactile sensor. In order to read the data, process it and produce the different curves in this thesis, a number of matlab functions is made. All relevant functions is included in the digital attachment, and some of the more important ones will be described here with an accompanying float chart. The series of functions could be applied on a similar data set in the same format with only small changes. Most of the functions are divided in 3 parent functions, pre-processing.m, processing.m and post-processing.m. In preprocessing.m the data is first read from the .csv file and passed to the workspace memory. Then the spatial events are found, sorted and renamed, before they are associated with timevents. Before moving on to processing.m, the data that was brought to the workspace to be available for these functions, is cleared, because it takes up a lot of space. Relevant information about the spatial events and timevents are passed to processing.m. In processing.m there are 3 functions. The first finds the cumulative sum of each single cell. The next finds the loads of each spatial event and sorts according to magnitude. The third makes distributions for each of the areas corresponding to number of triggered cells according to the maximum event method. The results of each function is passed on to postprocessing.m. This calls functions that are plotting different kinds of results, the various graphs that are presented in this thesis based on the data. In one of the functions, design curves, the parameters  $\alpha$  and  $x_0$  for each area distribution is integrated. These are found using a single standing separated function called man.m by manually fitting each graph to the tail of the data, also for the data that is accounted for exposure. These parameters are special for this data set, but using the tool man.m, these can easily be found for other sets as well. A function calling other functions, named "the\_ring.m" takes in a design scenario, recommends a structure and then performs a Monte Carlo simulation to see if the probability of failure is close to the target value. All functions starts with a premeable informing what the function does, what it returns, the author and date. In addition there is plentiful commenting inside the function to de-

scribe the work flow. In Appendix B all functions in the digital attachment is described. The maybe most relevant functions finding spatial and temporal events are explained in float charts found in Appendix C for assisting the understanding of the programs for the more interested.

## 4 Results

Based on the methodology described in section 3 and by the help of the authors Matlab functions the different results will be presented and explained. In the case where specific results demand more attention, this will come in section 5 following this section. First exposure of the sensor sheet, and distribution of the loads will be presented. Then two critical events is picked, based on highest load and highest single cell pressure, and presented with load history, spatial and process pressure area curves, in addition to a 3d plot of the magnitude and spatial distribution. Further design pressure area curves will be presented, both average pressure over total contact area relationship, and local pressure area curve considering sub areas for the whole dataset. The area distributions are presented, in addition to resulting design curves. Design load as a function of return period is presented. Finally possible structural alternatives is given in a table, and results from the Monte Carlo simulation is added.

### 4.1 Exposure of cells

The spatial exposure of the sensor over the test is examined. In order to have a standardized pressure distribution for each area, accounting for exposure is necessary as described in subsection 3.5. The parameter that determines the shift in the distribution is the total amount of censoring cells corresponding to the area in question that is exposed. For the pressure distribution corresponding to an area of one cell this is 507, which is the number of red cells in Figure 14. The figure shows all the cells in red that where ever triggered during test. The censoring sheet was 48 x 44 cells, but is here cut at 48 x 30 because the lower part of the sheet is dominated by noise, from about row  $> 25$ . The noise is due to curving of the support in the lower part, effecting the censor. Increasing rows is downwards, and increasing columns are in the direction of the bow. Although some noise is included, this is of little magnitude compared to the other data, as the following figures will show.

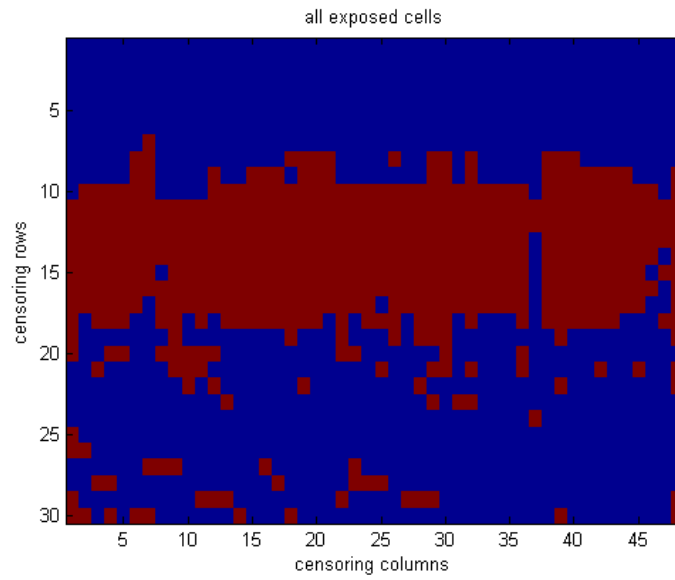


Figure 14: Showing all 507 cells in red that was ever triggered

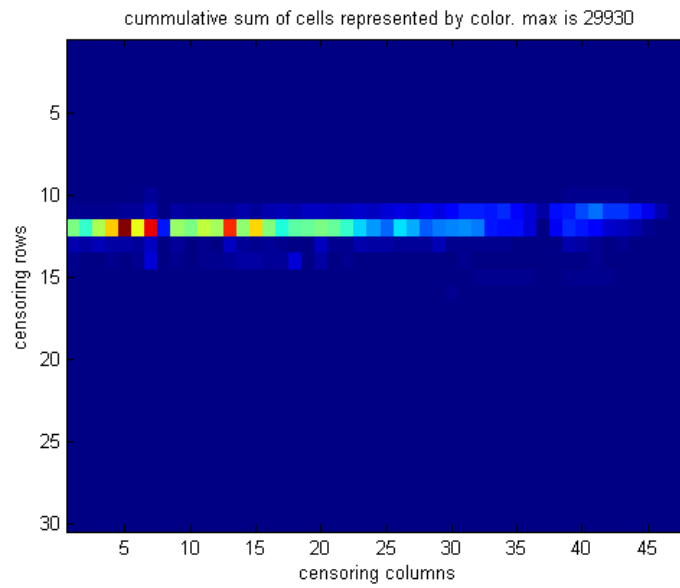


Figure 15: Cumulative value after color

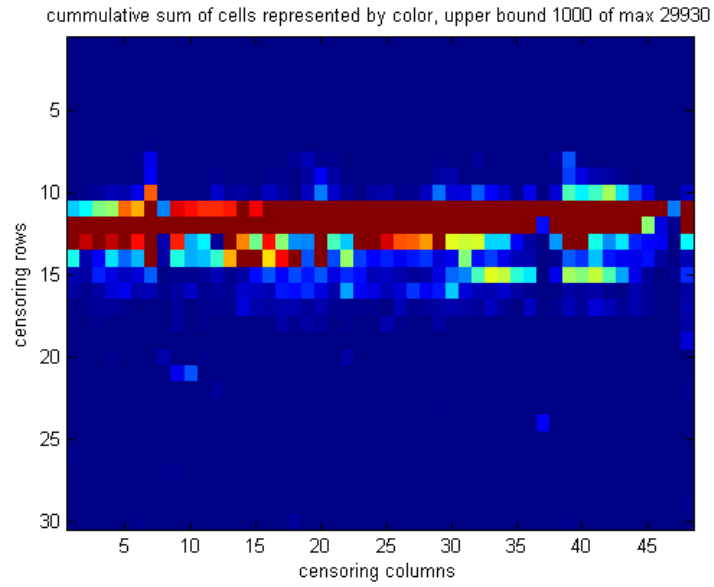


Figure 16: Cummulative value after color, saturated at 1000

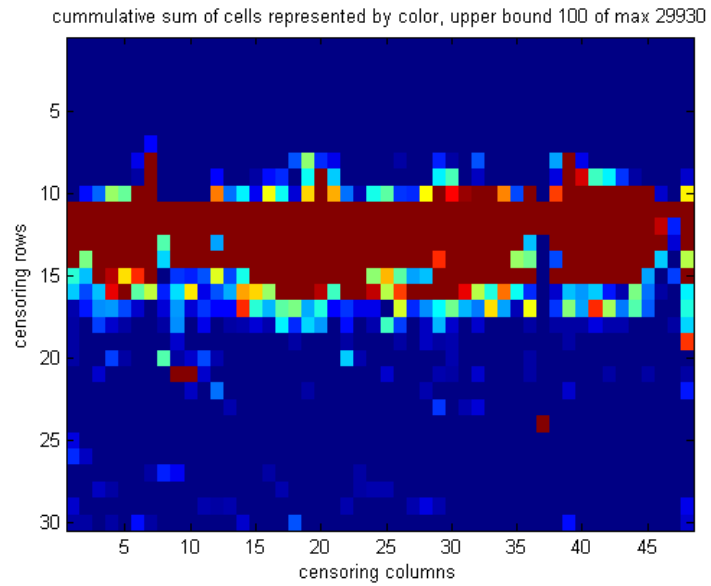


Figure 17: Cummulative value after color, saturated at 100

A Matlab function finding the cumulative sum of all pressures for each cell is used to produce Figure 15, Figure 16 and Figure 17. A warmth color map is divided into the range of cumulative pressures from dark blue at zero to deep red at 29930 for Figure 15, so that the color chart spans 29930 colors between dark red and dark blue. The range is here so large that the majority of the pressure cells are shown as deep blue, the lowest possible color, and it also shows it is a big drop between the top highest pressure cells. High frequencies and magnitudes are expected to appear at a line as shown here, but it is skewed to the left. This is not expected. To investigate this more Figure 18 and Figure 19 is plotted, showing also cumulative distributions, now represented by rows and columns respectively. Reasons for this will be discussed further in subsection 5.1.

In order to observe the lower range of cumulative pressures, Figure 16 and Figure 17 are plotted, now the color map is saturated at 1000 and 100 respectively, where all the dark red cells are now over 1000 and 100 respectively. In observing these lower range values the scatter is more clear, and higher values are closer to the top. When the color map is saturated at 100, the dark red color that represents all values over 100 spreads almost exclusively downwards. This is more clearly shown in Figure 18 where the cumulative distribution based on rows, is shown, with lower rows upwards. This distribution is skewed to the left, meaning upwards on the sheet, and with the majority of magnitude in row 12.

In Figure 20 the occurrence of number of contact spots are shown, where sub areas are included, so that an event with total  $n$  cells triggered will be counted also for all instants where less than  $n$  contact spots are considered, but not over. The plot is logarithmic, and occurrences less than 2 is not shown in the plot, but there is one event covering 32 cells, which is the maximum. The plot shows that the occurrences of smaller areas is much higher than for the larger ones. The figure represents the number of sample points that are the basis for each area distribution. From this one can understand that the distributions for higher areas are very uncertain. Because of this, area distributions from 15 triggered cells and up are not applied in the process of optimizing a structure. For clearance and comparison the occurrences of total contact areas of individual spatial events is shown in Figure 21.

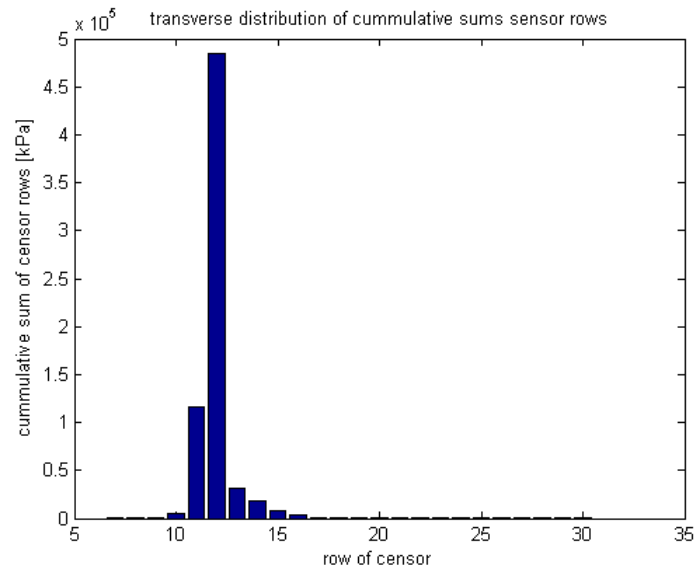


Figure 18: Vertical distribution of cummulative pressure over sensor

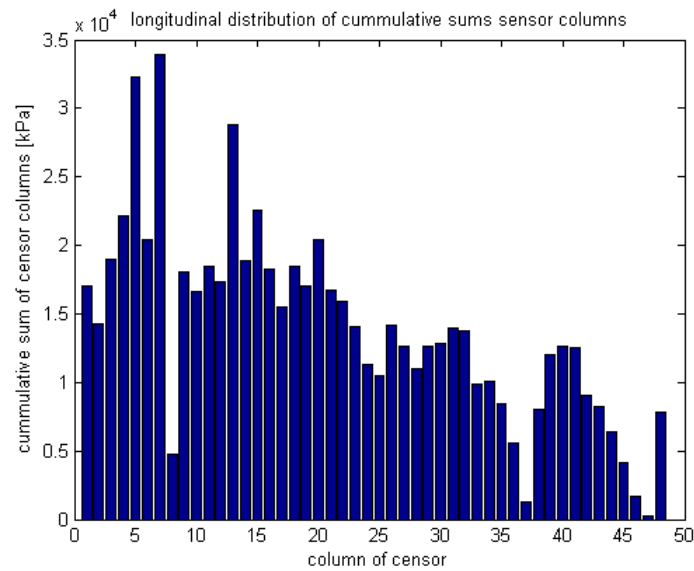


Figure 19: Longitudinal distribution of cummulative pressure over sensor



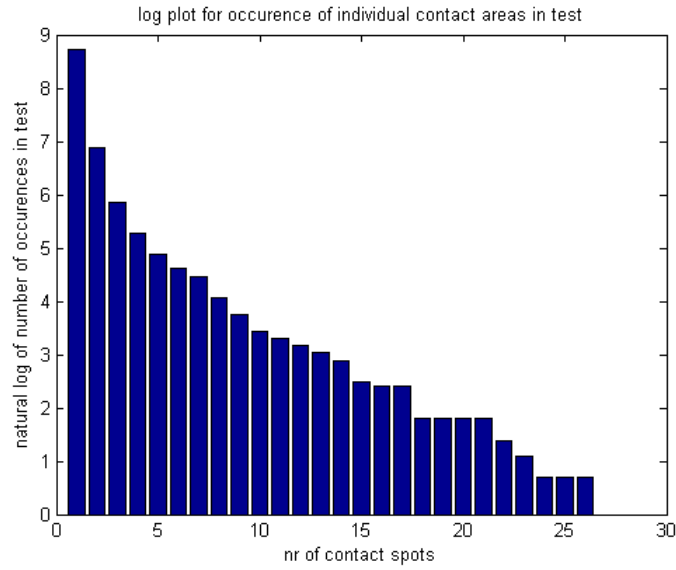


Figure 20: Occurance of individual contact area sizes including sub areas.

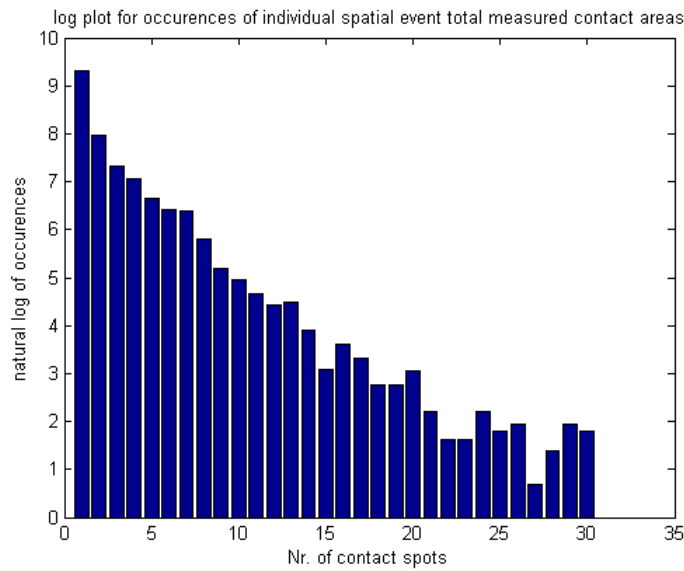


Figure 21: Log plot of occurrences of total areas of spatial events

## 4.2 Critical events

In order to get some insight into the nature of the dataset and to show methods to present individual events, two critical time events are presented. First the time event containing the highest load spatial event, then the time event containing the highest single cell pressure. The spatial events are presented with a 3d plot showing magnitude by individual cells with height and color, and the time events are presented by spatial pressure area curves for each of the individual spatial events. These are linked together with the process curve of the time event. In the digital attachment following this thesis there is a movie presenting the whole time series of the experiment showing following snapshots of the pressure sheet with triggered cells as colored bars after magnitude. Each snapshot is identified with the time frame at top where the difference between each time frame is 1/100 second, corresponding to frequency of observations.

### 4.2.1 Maximum load event

In Figure 22 a 3d plot for the spatial event with the highest load is presented. The x and y axis are the columns and rows of the sensor sheet with columns longitudinally and rows vertically along the midship. As is very typical for the whole experiment, the cells are triggered in a line, which is concentrated at row 12. This is a somewhat longer connected line than usual, since non triggered cells along the line is not unusual. Very local relatively high magnitudes are also not uncommon as can be seen at about row 27. The id number of the spatial event is 17598 and occurs at time event id 5385, at time frame 7244. The first spatial event in this time event is number 17280 at time frame 7175 and the last spatial event has id 17851 at time frame 7291. By use of the time frames the events can be seen in the pressure movie provided in the digital attachment. The greatest load measured about 2000 N, and can be seen as the peak in the time plot of the corresponding time event in Figure 24. Here also the time frame start, maximum and end can be seen, as the load builds up in a sawtooth kind of behavior and descends after the maximum. Figure 22 corresponds to the snapshot at the highest peak in Figure 24. Figure 23 shows spatial pressure area curves until maximum load for time event 7244 again corresponding to the highest load, with an attempt of explanation. Each spatial curve corresponds to each of the spatial events, each at one time instant. Early in the time event spatial curves are

plotted in dark blue, corresponding to the first time frames in Figure 24, and as the time event proceeds, the crushing area increases as seen in Figure 23 and spatial curves are plotted in increasingly warmer color, until maximum load plotted in a dark red fashion. The biggest area of the highest dark red curve corresponds to the maximum load, and smaller areas are pressures for sub areas within the total contact area of the maximum load spatial event. Connecting pressures for the total contact area of each spatial event (corresponding to a time instant), marked with black points in Figure 23, gives the process pressure area curve for the interval of time of this time event. As time and penetration increases to the maximum load of the event, the process curve may be interpreted as a rising tendency for higher areas for this event, but the curve is quite chaotic, and a connecting line is therefore not plotted. For design a similar curve is plotted but for the whole time of the experiment, and only the highest pressure for each area is kept. Figure 23 is similar to the illustration in Figure 6.

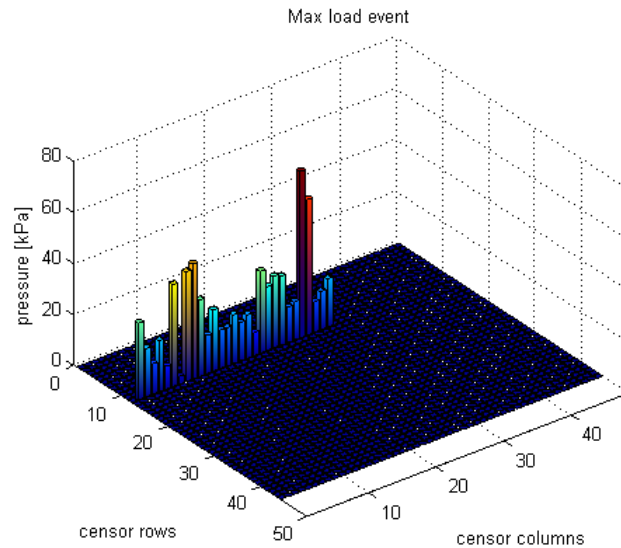


Figure 22: 3d plot for time instant of largest load

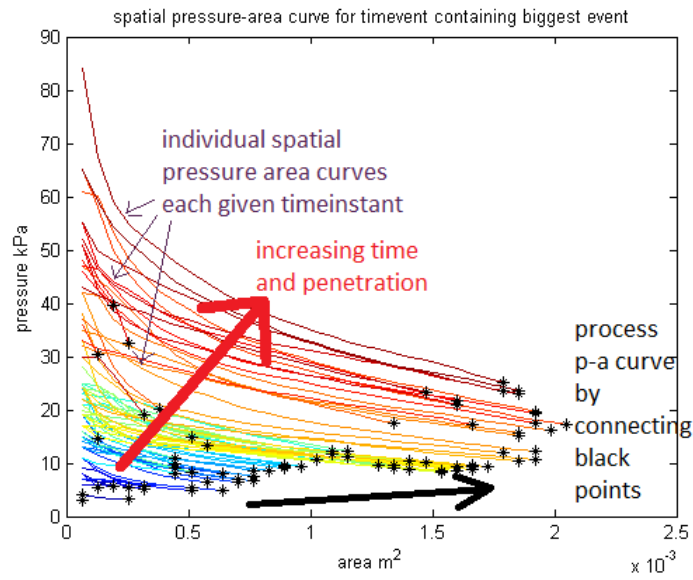


Figure 23: Spatial pressure area curve for largest load event

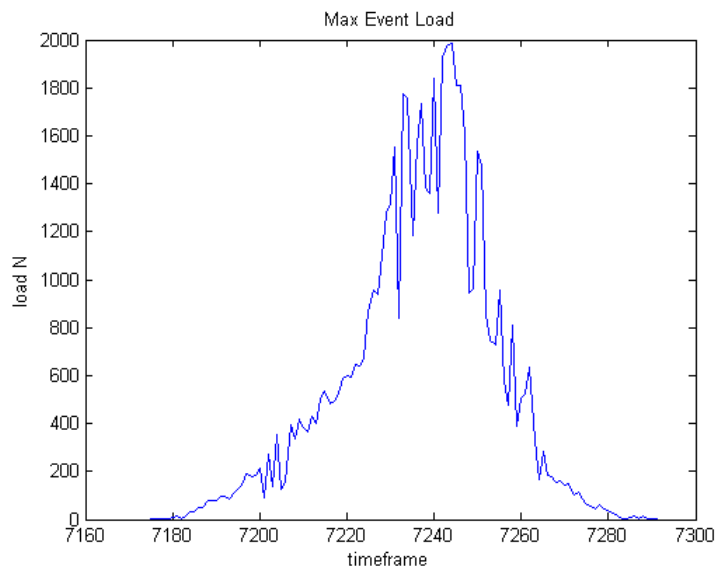


Figure 24: Force time series for largest load time event

### 4.2.2 Maximum triggered cell

In Figure 25 a 3d plot similar to Figure 22, showing the spatial event containing the highest single triggered cell pressure of 150 kPa. Very high local pressures fluctuating rapidly in time and space are not uncommon in his experiment, nor in full scale experiments. These are believed to be in the center of high pressure zones as described in subsection 1.4.1, transferring most of the load through a highly damaged layer under high confinement. The id number of the spatial event containing the highest pressure is 835 and occurs in time event id 408 at time frame 1789. This can be seen in Figure 27 showing time series of biggest single triggered cell in each event contained in time event 408. The peak of this curve corresponds to the plot in Figure 25 and the pressure of the lowest area of the highest curve in Figure 26. Figure 26 is similar to Figure 23 and Figure 6, but here for time event 408 containing the highest pressure, and no explanation added in the plot. The time event starts at time frame 1761 at cold blue colors and goes towards warmer colors until it peaks at time frame 1789, displayed in dark red. The time event containing the highest pressure lasts over a shorter time and contains fewer spatial events, that is why Figure 26 has less curves than Figure 23.

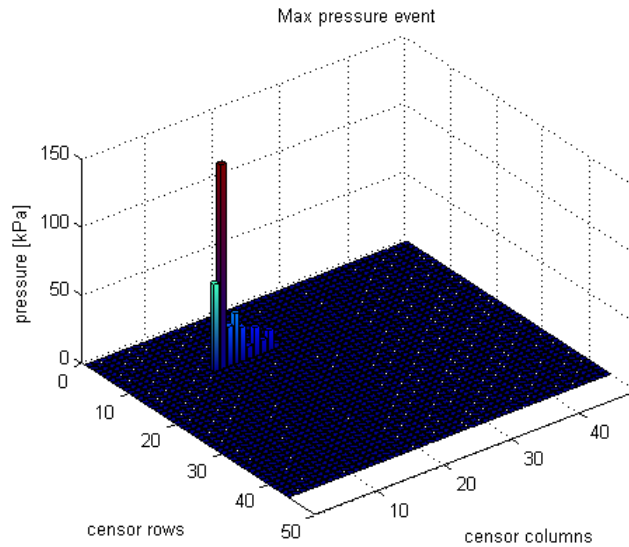


Figure 25: 3d plot for time instant of maximum triggered pressure cell

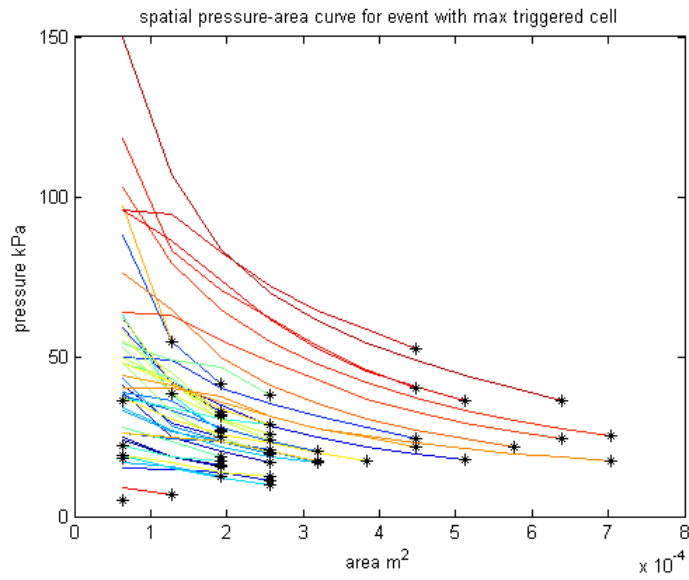


Figure 26: Spatial pressure area curve for largest triggered pressure cell

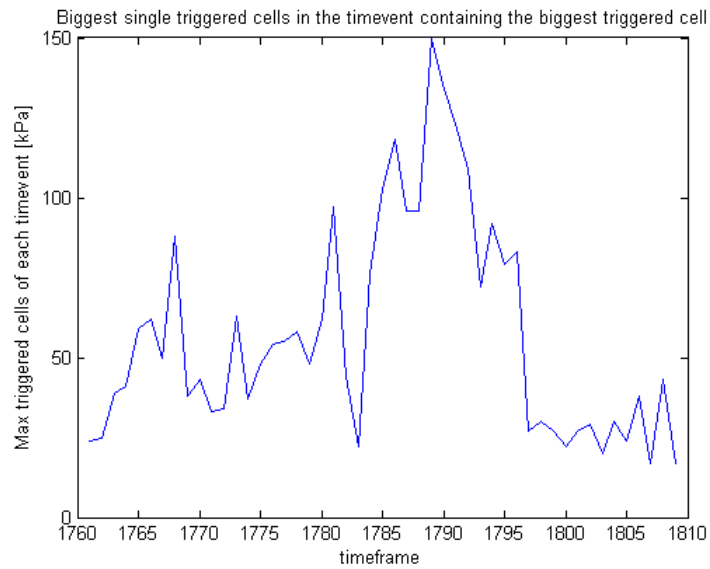


Figure 27: Pressure time series of biggest single triggered cell in each spatial event of the time event containing the largest single triggered cell [kPa].

### 4.3 Pressure-area curves

The process and spatial pressure area relationships discussed in subsection 1.5.3 were presented for demonstration in subsection 4.2. Here, the two other relationships that were discussed, the local pressure area relationship and the average pressure over total measured area relationship, will be presented. The local curve can be used for local design, while the other is less useful as long as the monitored area does not cover the entire global interaction area, meaning there are loads outside the monitored area.

The local pressure area curve describing pressures over sub areas and up to total contact areas of spatial events over the whole experiment is shown in Figure 29. The data follows a tendency as in Equation 4 as anticipated. The pressure is plotted for areas from one triggered cell at about  $0.1 \cdot 10^{-3} m^2$  until 32 triggered cells which is the highest amount of cells that are triggered in one spatial event. The plot is very even, except for 2 evident steps. This indicated that all values in each step is from the same very large spatial event. The first big event is only 21 triggered cells, or about  $2.2 \cdot 10^{-3} m^2$ , after this it jumps to the biggest spatial event bigger than 21 cells. The curve is plotted using the Matlab function called `pacurve.m`, which is available in the digital attachment. The function goes through all spatial events, observing pressures for sub areas within the event, starting with the highest single pressure and expanding to subsequent highest pressures until the total contact area of the spatial event as explained in section 3. Only the highest pressures for each area are kept and presented in the curve. The local curve is generally higher, but will approach the average pressure over total measured contact area curve for higher areas.

The average pressure over total measured area for the whole test is seen in Figure 28. It has a more random nature than the local curve because all points are from individual spatial events. Each spatial event of the data set is considered. This curve is by definition smaller or equal to the local curve, and is thus not used in design. It can be compared to the process curve, only for a longer time interval, and removing all but the highest occurrences for each area. The average pressure over total measured area curve is sinking with area according to Equation 4. Similarly the spatial relationship described for one time instant can be compared to the local pressure area relationship, only the local relationship considers all time instants in the data set and keeps only the highest values for each area.

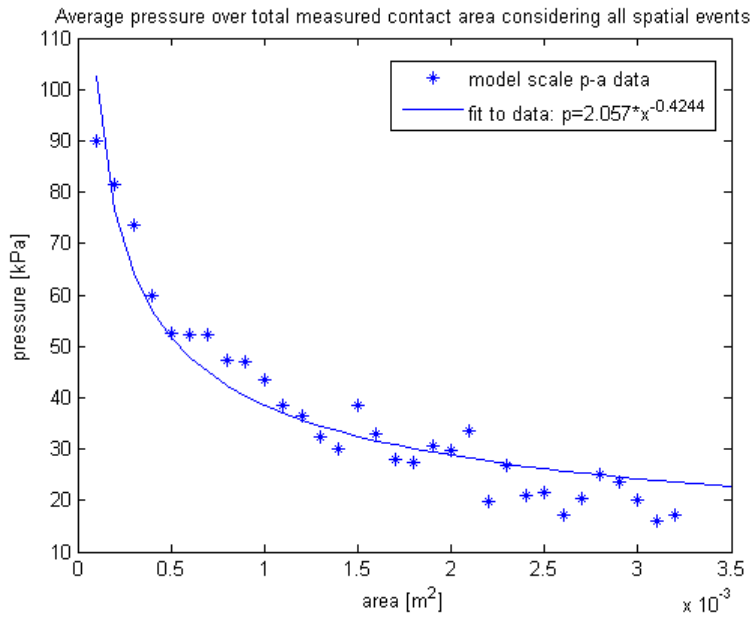


Figure 28: Average pressure over total measured area curve

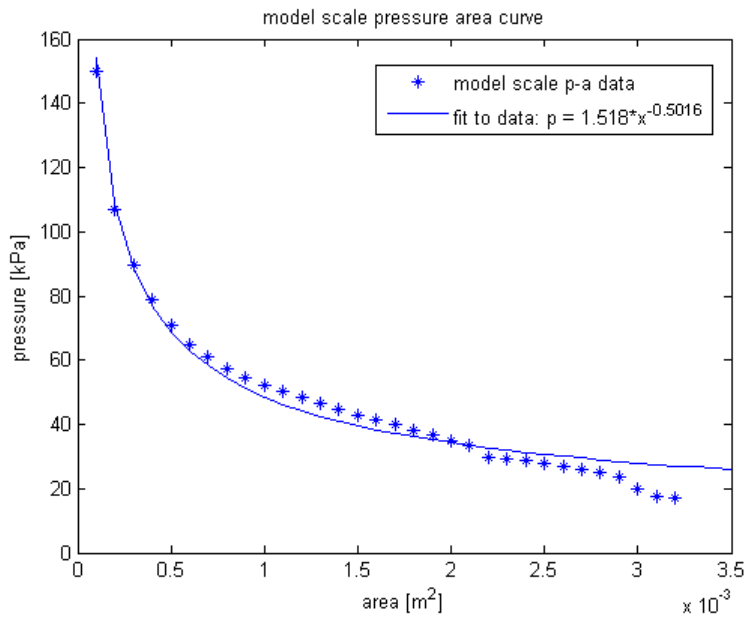


Figure 29: Local pressure area curve model scale



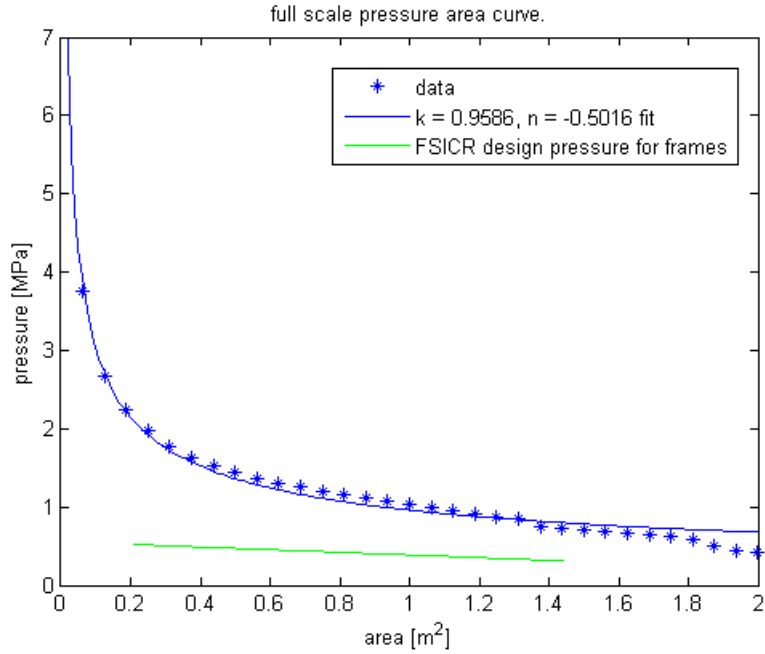


Figure 30: Local pressure area curve full scale presented with FSICR requirements for frames

The model scale pressures are scaled up linearly according to subsection 2.1.1 to give the blue plot in Figure 8. A curve is fitted to the data based on Equation 4 with  $k = 0.9586$  and  $n = 0.5016$ . The design pressure for frames midship from Finnish-Swedish ice class rules class 1 a super is shown in green. This considers a design ice thickness of 1 meter and a design pressure height of 0.35 meter, compared to 0.2728 m here, which is comparable. The design pressure is calculated as described in subsection 1.7.1, with Equation 19 limiting  $l_a$ , which is the spacing in the case of transverse framing, and the span in the case of longitudinal framing.  $c_a$  has a maximum value of 1.0 and a minimum of 0.6. The design rules pressure is about half of the scaled up extreme local pressures from the test. This indicates that compressive loads can be higher than what FSICR design for. In Figure 31 the same plot without the FSICR curve is presented in a double logarithmic plot. The data follows a straight line meaning it decreases exponentially with area until the largest areas, where it decreases more rapidly. This can be explained by the fact that the 6 largest areas are based on one single spatial event. The largest spatial event is composed of 32 adjacent cells, while

the next largest is only 26 cells. The 6 last pressure cells that are added to the average are the 6 smallest pressures of that spatial event and constitutes very little rise in the total average pressure. Considering the sparse data for these last 6 points, they should maybe have been omitted, but are showed for explanation purposes.

$$c_a = \frac{47 - 5l_a}{44} \quad (19)$$

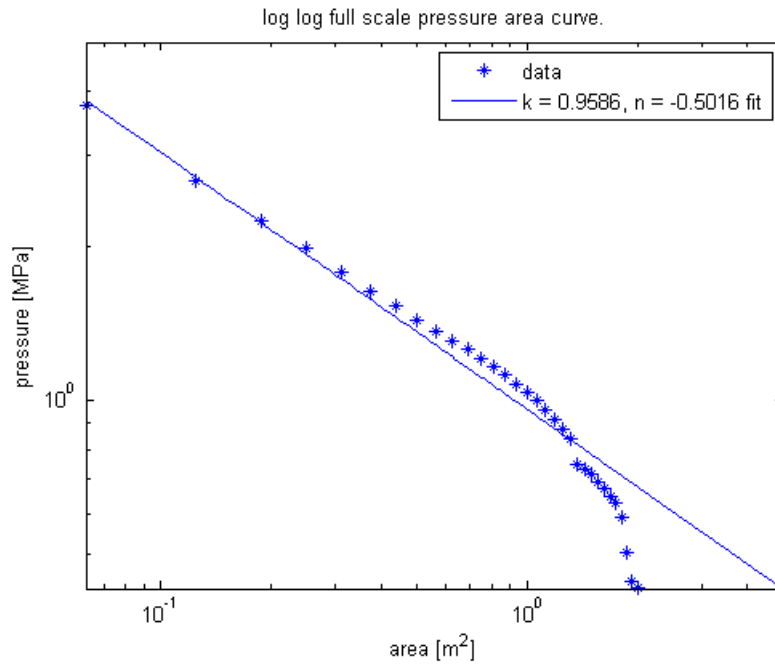


Figure 31: Local pressure area curve in double logarithmic scale

### 4.3.1 Distribution

Each area distribution can be presented ranking the data and plotting against the logarithm of  $\frac{i}{N+1}$  as explained in subsection 1.6, and adjusted for exposure as explained in subsection 3.4.2. This is done in Figure 33 for the area distribution corresponding to one cell and the pressure values are scaled up linearly according to subsection 2.1.1. Also included in this plot is the fit to tail data adjusted for exposure from the Polar Sea in Bering Sea 1983 obtained from [Taylor et al., 2010]. The data is based on an area of one

sub panel of the area  $0.1516 \text{ m}^2$ . The dimensions of one censor cell in the experiment considered here is in full scale  $0.2291 \text{ m}$  wide, and  $0.2728 \text{ m}$  high, giving an area of  $0.0625 \text{ m}^2$ . The Polar Sea data is quite much lower in the plot than the compressive test data accounted for exposure, meaning it is actually towards higher probability of exceedance. This is not surprising since data is collected from the bow, from a larger area and is probably more severe conditions in the Bering Sea. It is still compared here in that it is one of the few other data sets presented in the literature that has a similar data processing procedure. Similar Weibull plots, but in model scale for each of the distributions up to an area of 26 triggered cells are presented in Appendix D.

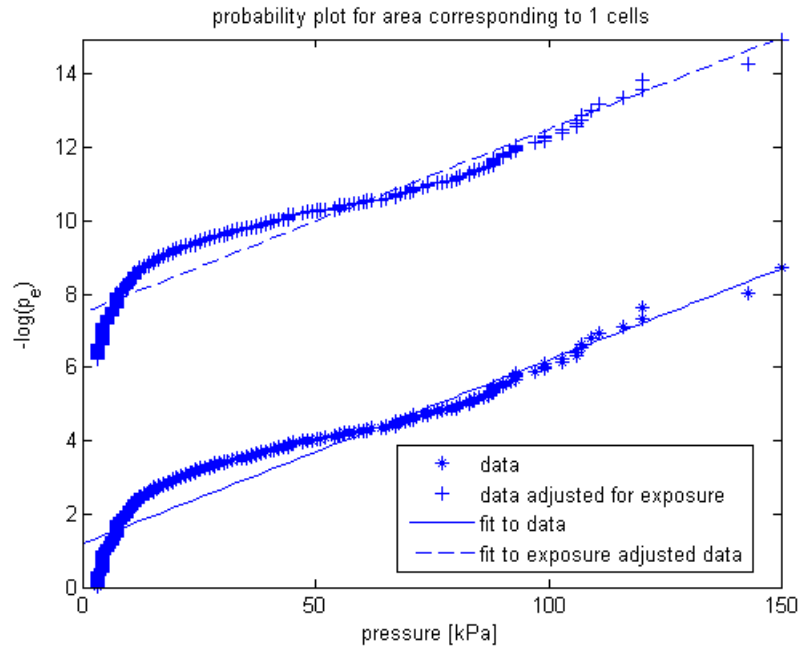


Figure 32: Probability of exceedance presented in Weibull plot for original pressure data

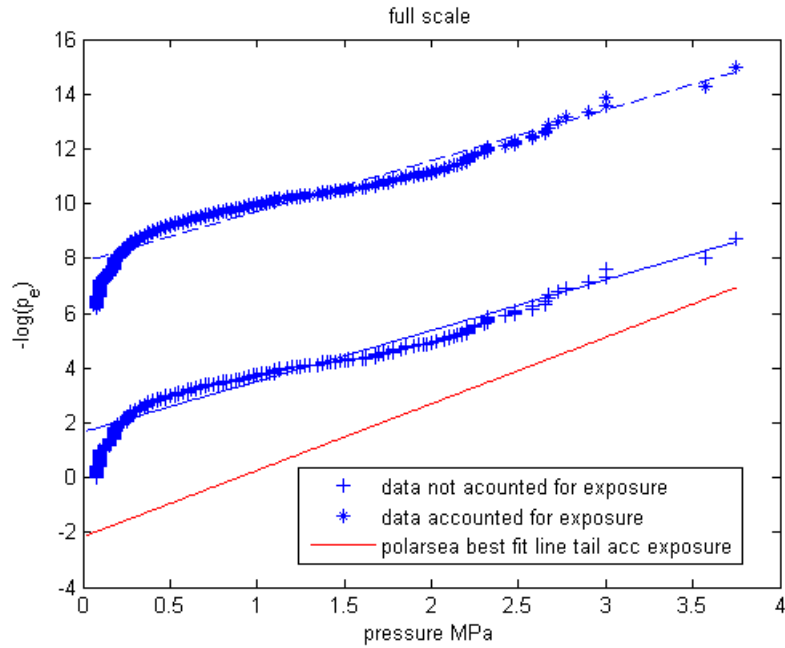


Figure 33: Probability of exceedance of pressures presented in weibull plot for scaled up data compared to Polar Sea best fit to tail distribution [Taylor et al., 2010].

### 4.3.2 Design curves

The making of the design curves presented in Figure 35 and Figure 36 are presented in subsection 3.4.4. These curves are produced from one data set. Based on the local area one wants to design for, the correct parameters,  $\alpha$  and  $x_0$ , are chosen to the shifted exponential distribution, where  $\alpha$  is the inverse slope and  $x_0$  is the intersection with the x axis. Several data sets were studied by Taylor et al. [2010], showing that the tendency of the  $\alpha$  - area relationship follows a curve described by Equation 20, where  $D$  is smaller than one. This curve should not be confused with the pressure area curve, described by Equation 4, although they have the same tendencies, and are sometimes both referred to as design curves.

In Figure 34 the curve referred to as the "design curve", also seen in Figure 9, from Taylor et al. [2010] is added in red, in addition to the fit to the lowest data set from Polar Sea, Bering 1986 shown in green. All the other data sets were in between these. The blue points are the data from

the set considered here, showing even smaller values. The fitting of each distribution, resulting in the design curves can be seen in Appendix D and is done by hand, so the quality can be discussed, but there is still no doubt about the tendency. The low values and the smiling shape seen in Figure 34 is unsuspected based on existing curves as seen in Figure 9. This will be discussed in subsection 5.2.

The pressure resulting from the distributions with the different parameters is also a result of  $x_0$ .  $x_0$  is the intersection with the x axis in the Weibull plot, and changes when adjusted for exposure, to  $x_0e$ , ( $x_0$  adjusted for exposure) which is applied in design. Both can be seen as a function of area in Figure 36. The raw values follows the same tendency as expected from Figure 10, but the data adjusted for exposure does not, it is rather decreasing for increasing areas. This will also be discussed further in subsection 5.2.

$$\alpha = C \cdot a^{-D} \quad (20)$$

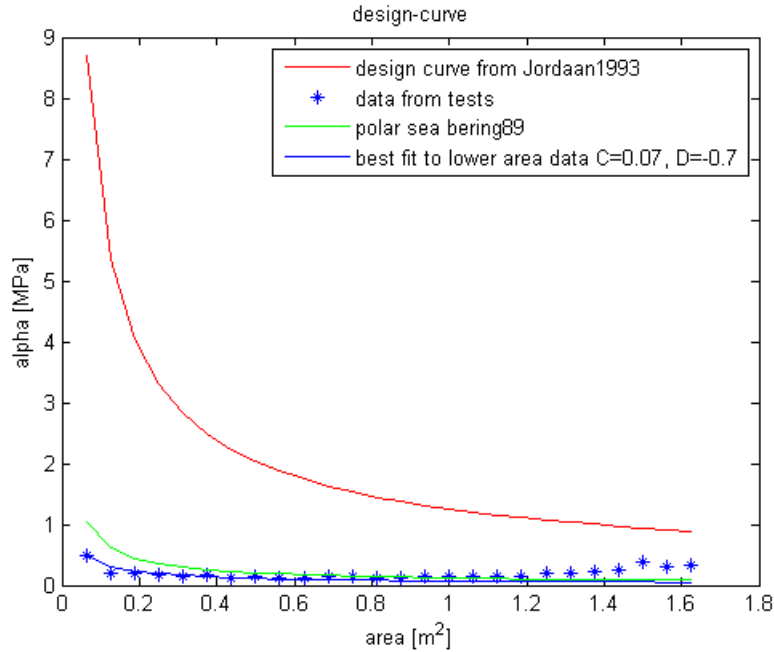


Figure 34: alpha-area design curve

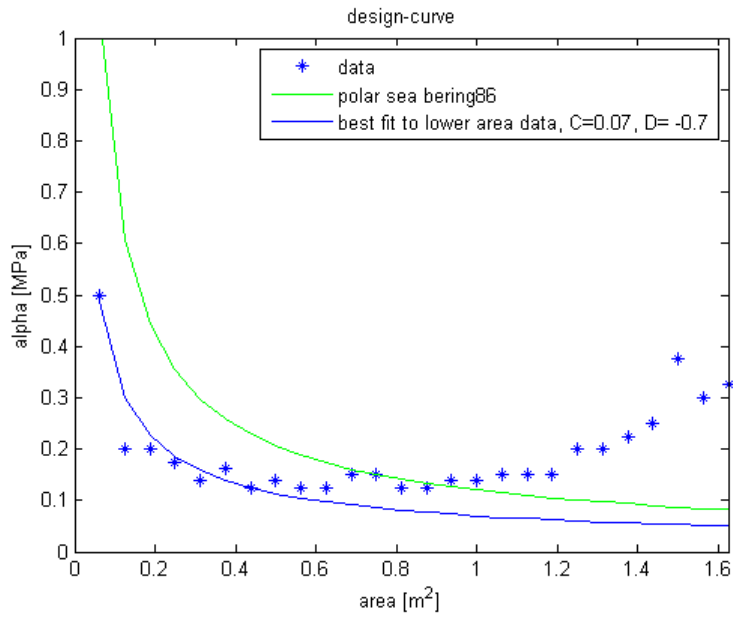


Figure 35: alpha-area design curve

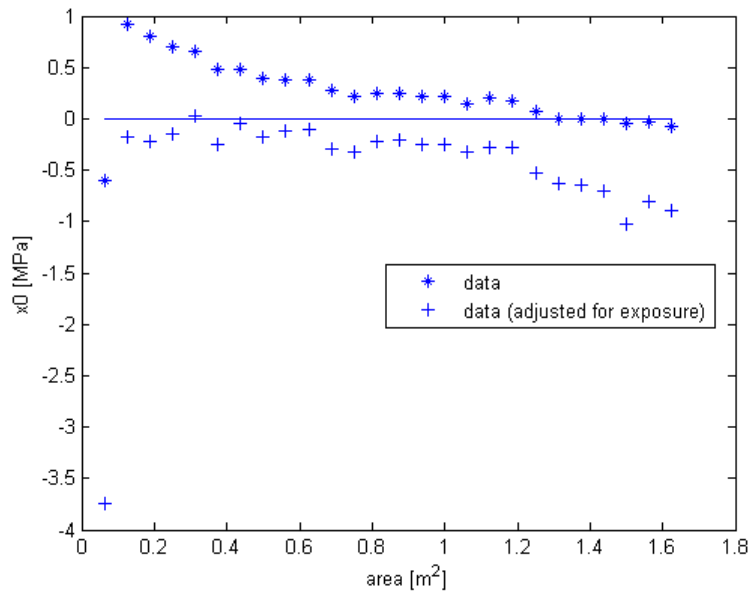


Figure 36: x0-area design curve

### 4.3.3 Return period

Using Equation 16, Figure 37 can be produced. Based on the distributions for each area the extreme load used for design is plotted as a function of return period for each area. Cumulative probability is a function of return period as  $F_z = 1 - \frac{1}{\text{returnperiod}}$ . From a set return period, design load for each area can be found.

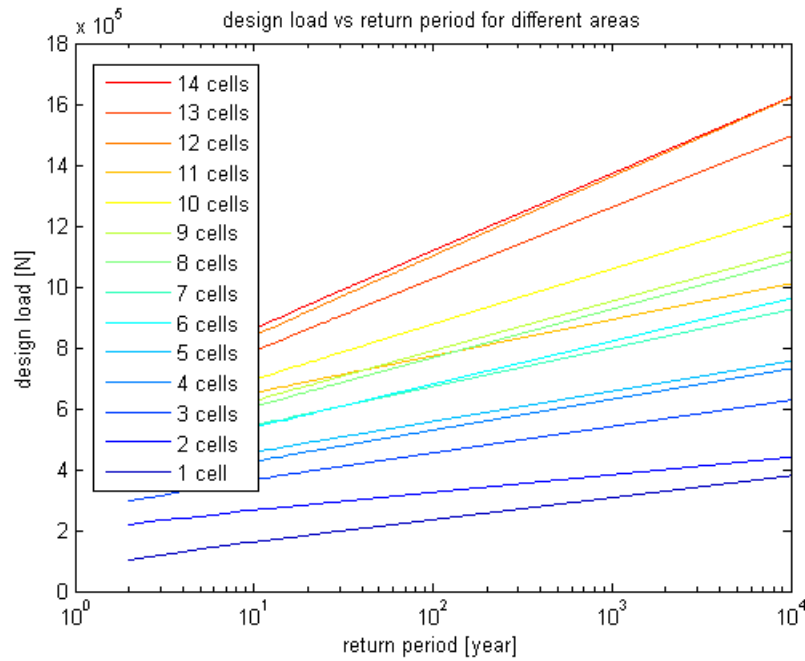


Figure 37: Return period vs design load for given design scenario

## 4.4 Optimized structure

Based on the design procedure described in subsection 3.4.6, the different structural options presented in Table 6 and Table 7 are considered. Alternatives for frames are chosen from Figure 38, which are existing L-profiles produced by Ruukki. To limit workload, spacing in the case of longitudinal framing is set to 0.3 m, and span in the case of transversal framing to 2.8 m. For simplicity one kind of profile is considered, L profiles from Ruukki. The column "cells" represent the number of corresponding censor cells that it is place for along the longitudinal direction of the plate, and is the same

as the area distribution for the area corresponding to the same amount of cells. Span and spacing is termed  $l$  and  $s$  respectively.  $Z_{req}$  is the section modulus requirement based on the area distributions, and  $Z$  is the section modulus of the ready recommended scantlings, and is also compliant with FSICR. Ruukki row identifies the stiffener used based, on the row number in Figure 38.  $\frac{weight}{area}$  is a cost measure, in that steel weight is proportional with cost. For comparison the requirement for midship section modulus of a vessel with class 1 a super is presented in column  $Z_{req}$  FSICR. The ratio between the two requirements is also presented. In the last column the probability of failure based on the Monte Carlo simulation is presented. A recommendation based on the tables are found in subsection 5.3.

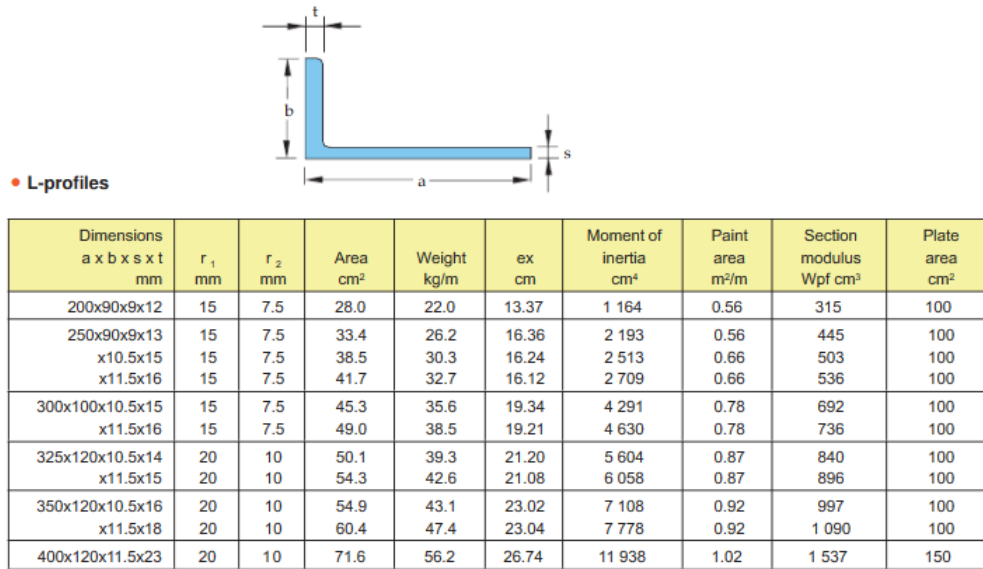


Figure 38: Possible L profiles chosen from Ruukki table



Table 6: Longitudinal framing structural alternatives, spacing= 0.3 m.

Cells	l [m]	$Z_{req}$ [ $cm^3$ ]	Z	Ruukki row	$\frac{weight}{area}$	$Z_{req}$ [ $cm^3$ ] FSICR	$\frac{Z_{req}}{Z_{FSICR}}$	$P_f$
13	2.98	1319	1404	11	110	174	7.6	0.0073
12	2.75	1306	1404	11	111	154	8.5	0.0062
11	2.52	1119	1404	11	113	133	8.4	0.0016
10	2.29	866	922	9	102	114	7.6	0.0094
9	2.06	701	702	6	110	95	7.4	0.0147
8	1.83	605	654	5	102	77	7.9	0.007
7	1.60	464	483	3	102	61	7.6	0.0087
6	1.37	402	419	2	93	46	8.7	0.0092
5	1.15	276	301	1	93	33	8.4	0.0052

Table 7: Transversal framing structural alternatives, span= 2.8 m.

Cells	s [m]	$Z_{req}$	Z	Ruukki row	$\frac{weight}{area}$	$Z_{req}$ FSICR	$\frac{Z_{req}}{Z_{FSICR}}$	$P_f$
1	0.23	284	292	1	169	83	3.4	0.0101
2	0.46	392	446	2	149	162	2.4	0.0029
3	0.69	549	572	4	159	237	2.3	0.0113
4	0.92	639	746	5	167	307	2.1	0.0027

#### 4.4.1 Monte Carlo simulation

The procedure for the Monte Carlo simulation is explained in subsection 3.4.7. The resulting distributions for the simulation run for area, and recommended structure corresponding to 10 cells is shown in Figure 39. In green is the strength distribution, which lies generally higher than the load distribution shown in purple. The two structures overlaps just a little, and the margin which is the distribution of the difference between the two is shown in black. The percentage of area of the margin under zero is probability of failure of the structure under the design load and is in this case 0.0094, which is under the target value of 0.01. Since the statistical distributions are here based on one year, 0.01 failure in one year is 1 failure in 100 year, which is the return period that is designed for.  $P_f$  is accepted as long as it is lower than 0.01. Result from Monte Carlo simulations of all the other structural options can be seen in Appendix E.

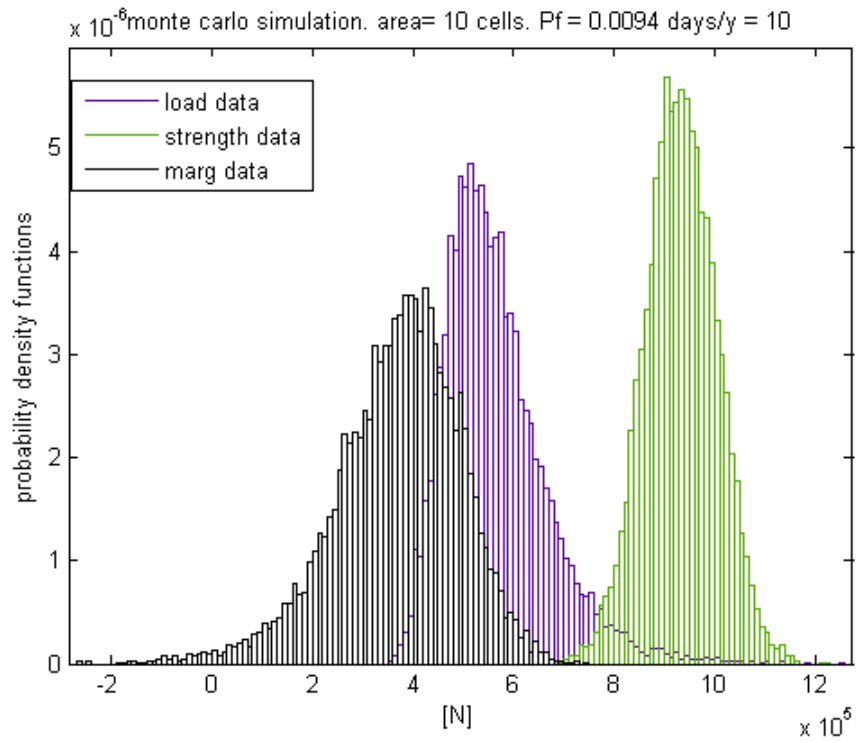


Figure 39: Resulting distributions from Monte Carlo simulation for given scenario and longitudinal framed structure with design load corresponding to 10 cells.

## 5 Discussion

### 5.1 Exposure of cells

From both Figure 14 and Figure 19 and the other cumulative plots, it can be seen that column 37 and 47 are almost dead, compared to column 5 and 7 which expose very high magnitudes. One row that can cause some inconvenience is row 8 which is an insensitive row amongst very sensitive ones. Cells in these kinds of rows result in events that are split in two spatial events separating even large events in two, which could have otherwise been maybe double if counted as one, and then may be one of the critical events in terms of force. After a conversation 16th of April 2013 with Mikko Suominen who was there conducting the experiment, two of these low rows can be explained by a force censor that was installed in the ship side under the censor sheet, leaving small cutouts on the side of it where there is no support for the censor row. The skewness might be due to a little misalignment in the force censor behind the censor sheet, or insufficient testing time/ population in the data set.

Observations similar to the skewness to the upper part as shown in Figure 18 has been made by [Määttä et al., 2011] where "the average position of the line like contact prevailed at the upper part of the ice thickness". Each row in the sheet is 10.9 mm high, and the ice thickness is 29 mm. Although it is not sure where the ice is relative to the sheet, at least it covers a little over two and a half row. Some relative motion between ice and sensor can be assumed and explains partly why it acts over a bigger height, but also broken ice that is pushed down triggers lower sensels.

### 5.2 Distributions and design curves tendencies

The fact that  $\alpha$  is generally lower than similar curves from the literature as seen in Figure 34 means that the slope of the considered data set is generally higher, since  $\alpha$  is the inverse slope.  $\frac{1}{\alpha}$  is the slope at which probability of exceedance,  $P_e(p)$ , decreases with area. The tendency implied by Equation 20 shows that  $\alpha$  decreases with area, meaning the slope of the Weibull probability plot increases with area, which implies that the slope of less probability as a function of area increases with higher areas. This tendency fits the experimental data until areas corresponding to about 10 cells, at about  $0.6 m^2$  full scale, where the tendency is more increasing for higher areas. This can

be seen in Figure 35, where the green line is the lower data set from Taylor et al. [2010], and a fit to the lower data in the form of Equation 20 with  $C = 0.07$  and  $D = -0.7$ . Based on Taylor et al. [2010] data sets, the rise in  $\alpha$  for higher areas is unexpected. It should be noted that for higher areas, the data set gets more and more sparse, and therefore uncertain, in addition to the problems of fitting a line to the diminishing tail, as can be understood from a look at the plots for higher numbers of triggered cells in Appendix D.

The fact that the  $x_0$  data adjusted for exposure is decreasing rather than going towards zero for higher values as in Figure 10, may have to do with the total amount of exposed panels,  $m$ , applied in adjusting for exposure, as this is much higher than the maximum amount of cells that are triggered in one event, 32, although only until 26 is presented, because of the sparse amount of higher areas. If the amount of triggered cells in an event would approach the total number of exposed cells, the adjusted data would approach the raw data. In the case of the data gathered by Taylor et al. [2010] it is possible that this is the case, that there are instants where all monitored panels are triggered at once. In the data set considered here, it is not even close, as the censor sheet has many small cells and covers larger area than the area generally exposed by ice. In addition the time of the series in question is just the time it takes towing the model over the tank, while the other data sets has been collecting data over longer periods, promoting probability of pressures covering larger parts of the monitored area. Decreasing  $x_0e$  for increasing areas results in a shift upwards in the Weibull probability plot, resulting in generally lower probabilities for all pressures. This can be seen in Appendix D.

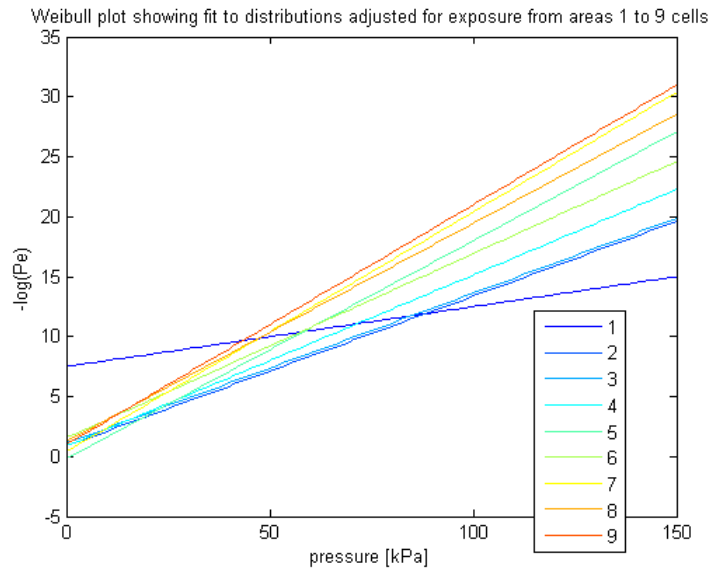


Figure 40: Weibull probability plot for distributions corresponding to areas 1 to 9 cells for model scale data.

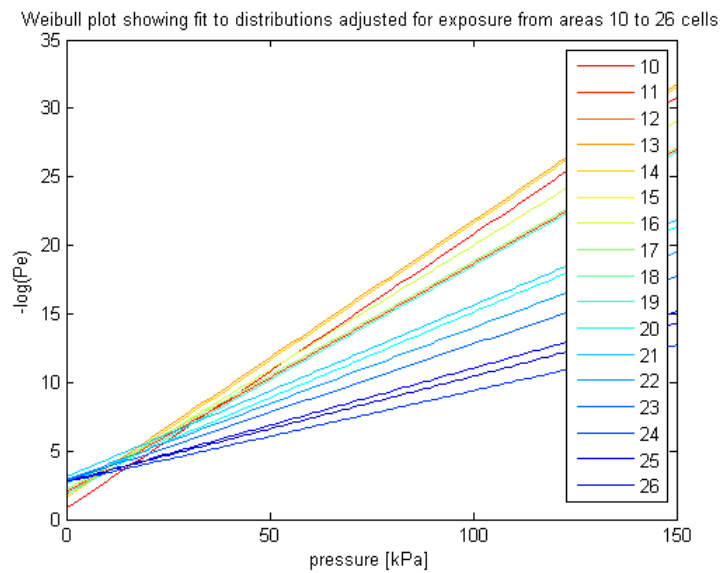


Figure 41: Weibull probability plot for distributions corresponding to areas 10 to 26 cells for model scale data.

To make it more clear what happens with the Weibull probability plots in Appendix D as  $\alpha$  and  $x_0e$  changes, graphs for the fit to the adjusted data in model scale are added into one plot for comparison. In Figure 40, distributions for areas corresponding to 1 to 9 cells are compared. It starts with cold colors for one cell and ends with warm for 9 cells. For areas corresponding to 1 to about 9 cells,  $\alpha$  is decreasing with area, as seen in Figure 35.  $\alpha$  is the inverse of the slope, therefore the slope increases with increasing area, towards warmer colors. Note that upwards on the y axis is towards lower probabilities.  $x_0e$  is around 0 to minus 10 for areas up to about 9 triggered cells, except for the first extreme value, at -150. This first blue line corresponding to area of one cell reflects the high pressures observed at small areas. For higher areas, corresponding to about 10 cells and more,  $\alpha$  is increasing, implying the slope is decreasing, as seen in Figure 41, towards higher probabilities. Now medium areas are warm, and increasingly colder towards higher areas. Further  $x_0e$  is generally lower for higher areas, from -10 to -40.

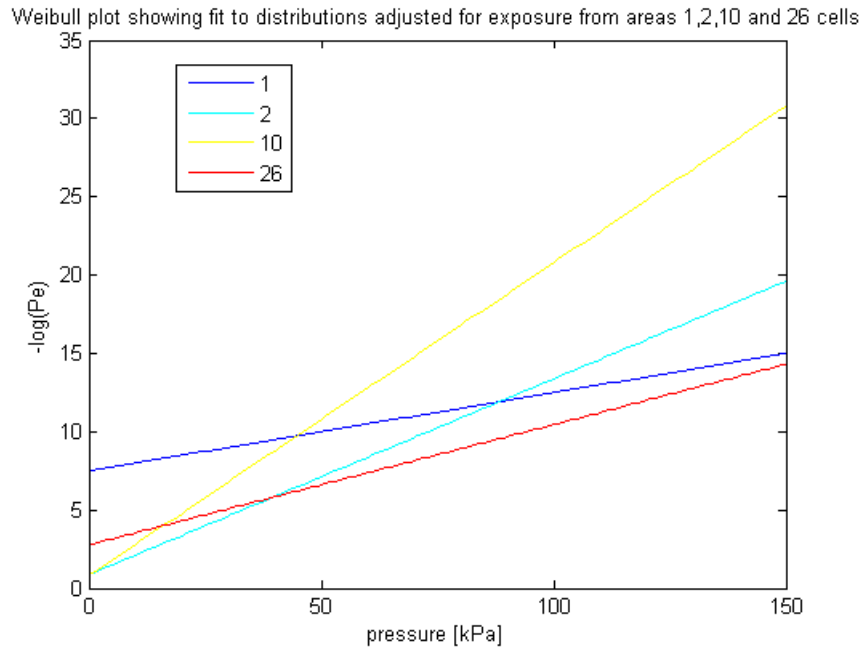


Figure 42: Weibull probability plot for distributions corresponding to areas 1, 2, 10 and 26 for model scale data.

To cut down on the information, distributions for a few areas are compared, including the extremes at low and high areas, see Figure 42. Here it is clearly seen that the distribution for 26 triggered cells has higher probability for all higher pressures. The curves are here extrapolated over the values observed, as the highest value for areas of 26 triggered cells where only 12 kPa, as seen in Appendix D. Although the probability seems higher, one has to take into account that the arrival of large areas is much lower than small areas, as seen in Figure 20. This is an aspect of exposure, as discussed in subsection 3.5, and is taken into account when predicting pressures by  $\mu$  in the extreme distribution, as explained in subsection 3.4.3.

When looking at it from a physical point of view, it is quite logical that higher areas promote all ranges of pressures. Consider crushing over a large area. Crushing is known to have a sawtooth pressure-time behavior. The sawtooth behavior in crushing is attributed to pressure buildup in confined regions, energy transferred to the damaged layer, promoting high pressure zones, until the layer fails in an extrusion event and there is a pressure drop. A large area will contribute to the confinement promoting high pressures, and the failure of the layer will lead to small pressures. For small areas, the ice edge is never far away, promoting spalling, which for an instant leaves all the energy to be transferred through a very small area, promoting high pressures. For medium areas like 10 triggered cells, there are not enough confining pressure to produce high pressure peaks that will dominate the average over many cells.

### 5.3 Optimized structure

In the tables presented in subsection 4.4 the requirements, based on the distributions from the model tests and with the given scenario, is compared to FSICR. The FSICR requirement is based on a yield limit and considers 1000 days in ice during a lifetime [Riska and Kämäräinen, 2011], compared to 10 days in compressive ice over 100 year return period considered here, which equals 1000 days. In FSICR yield is accepted during the lifetime of the vessel, while longer return periods are used for plastic design. Based on the tables a qualitative recommendation can be done. Based on the weight-area ratio objective short longitudinal stiffeners are preferable. If one in addition assumes on a qualitative basis that numbers of stiffeners is also proportional to cost, because of longer working hours for more welding seams,

a second objective is to keep numbers of stiffeners low, and therefore spans and spacings longer. With this in mind a longitudinally framed panel with length corresponding to 10 cells would be a good choice in this case.

## 6 Conclusion

Crushing against vertical side shells can cause high loads, and are typically higher than other failure modes because of the high compressive strength of ice. Compressive ice can cause large deflections over a long region of the hull if the vessel gets stuck. Classification societies do not explicitly design for compressive events, and the local strength requirement from FSICR was shown to be lower than required strength predicted based on the distributions from the experiment. Different kind of pressure area relationships are identified, and used to investigate the spatial and temporal properties of the data. A new event definition is defined in order to apply the maximum event method. An exponential distribution is fit to the highest values of the data, and a Gumbell distribution used to predict the design load based on a scenario. Out of several structural options considered, one is chosen based on a qualitative cost objective. The design is validated using Monte Carlo simulation.

The maximum event method developed by Jordaan et al. [1993] is applied successfully on the new event definition. The new definition is suitable for semi-continuous interaction area, and is based on temporal events, consisting of spatial events. This makes it possible to produce design curves for probabilistic design from only one dataset of sub-panels. The method based on the new event definition can be used in reanalysis of existing datasets and in future tests. The result from the Aalto compressive ice test using the maximum event method on the new defined event, indicates that existing strength requirements for midship is too low according to the scenario. This is especially true for longitudinal framing. Compressive ice events should be considered for vessels that may encounter this in future design.



## 6.1 Further work

The methodology is only applied on one run out of 6 in the same experiment, where both bow and midship were monitored. It would be preferable to examine the rest of the data sets with the same method. In doing this one should check that only the data from the actual testing time interval is analyzed. Instead of treating sub-areas of spatial events as here with including subsequent next highest pressure in the average, a new algorithm could be developed, with a corresponding script. This should find the highest average of any combination of adjacent (in contrast to connected) triggered cells of each spatial event. The sampling method based on maximum of temporal events consisting of spatial events should be applied on full scale data. Based on the new scenario and results from full scale application of the method, design recommendations for compressive ice loads on various sizes of local areas can be developed. Pressures as a function of aspect ratio, and pressure-confinement relations would be interesting to see. Further studies of the quality of model tests in compressive ice, and comparison to similar full scale tests should be performed before applying results in design.

## 7 References

*Tekscan. I-Scan equilibration and calibration practical suggestions.*

- A. G Atkins and R. M Caddell. The laws of similitude and crack propagation. *International Journal of Mechanical Sciences*, 16:541–548, 1974.
- C Daley. A study on the process-spatial link in ice pressure-area relationships. *NRC Publications Archive (NPArc)*, 2004.
- C Daley, A Kendrick, and E Appolonov. Plating and framing design in the unified requirements for polar class ships. In *Proceedings of the 16th international conference on port and ocean engineering under Arctic conditions*, 2001.
- E Enkvist, P Varsta, and K Riska. The ship - ice interaction. *Port and Ocean Engineering under Arctic conditions*, 2:977–1002, 1979.
- Patrick Eriksson, Jari Haapala, Istavan Heiler, Hanna Leisti, Kaj Riska, and Jouni Vainio. Ships in compressive ice. Technical report, Finnish winter navigation research board, 2009.
- R Frederking. The local pressure area relationship in ship impact with ice. In *Proceedings of the 15th international conference on port and ocean engineering under Arctic conditions*, 1999.
- R Frederking, I J Jordaan, and McCullum J. S. Field tests of ice indentation at medium scale: Hobson’s choice island 1989. In *Proceedings of the 10th International Symposium on Ice, IAHR, Espoo, Finland*, 1990.
- R Gagnon. Analysis of data from bergy bit impacts using a novel hull-mounted external impact panel. *Cold Regions Science and Technology*, 52: 50–66, 2008.
- R Gagnon, A Bugden, and R Ritch. Preliminary testing of a new ice impact panel. *Port and Ocean Engineering under Arctic conditions*, 01:33, 2009.
- G. A. M Ghoneim and A. J Keinonen. Full-scale impact tests of canmar kigoriak in thick ice. *Port and Ocean Engineering under Arctic conditions*, 3:329–346, 1983.

- Samuli Hänninen. Incidents and accidents in winter navigation in the baltic sea, winter 2002-2003. Technical report, Finnish winter navigation reasearch board, 2003.
- K Izumiyama, Wako D, and S Uto. Ice pressure acting over a model ship hull. *Port and Ocean Engineering under Arctic conditions*, 2:793–802, 2001.
- I J Jordaan, M A Maes, Brown P W, and I P Hermans. Probabilistic analysis of local ice pressures. *Journal of Offshore Mechanics and Arctic Engineering*, 115:83–89, 1993.
- I J Jordaan, R. S. Taylor, and J Wells. Ice crushing, damage layers, and pressure-area realtionships. In *Proceedings of the 20th International Conference on Port and Ocean Engineering under Arctic conditions*, 2009.
- Ian Jordaan, Jonathan Bruce, Dan Masterson, and Robert Frederking. Local ice pressures for muliyear ice accounting for exposure. *Cold Regions Science and Technology*, 61:97–106, 2010.
- S Kivimaa. Long term measurements with an ice load panel in board the cutter ms uisko. *Port and Ocean Engineering under Arctic conditions*, 1: 338–350, 1993.
- K Kotisalo and P Kujala. Ice load measurements onboard mt uikko during the arcdev voyage. *Port and Ocean Engineering under Arctic conditions*, 3:974–987, 1999.
- N Krupina and Alexey Chernov V. Measuring global ice forces during the full-scale ice impact study of icebreaker "kapitan nikolaev". *Port and Ocean Engineering under Arctic conditions*, 37, 2009.
- P Kujala and S Arughadhoss. Statistical analysis of ice crushing pressures on a ship's hull during hull-ice interaction. *Cold Regions Science and Technology*, 70:1–11, 2012. URL <http://www.scopus.com/inward/record.url?eid=2-s2.0-83055184374&partnerID=40&md5=6950067d9ec35478c365a84c493d8c00>. cited By (since 1996) 0.
- P Kujala and J Vuorio. On the statistical nature of ice induced pressures measured on board ib sisu. *Port and Ocean Engineering under Arctic conditions*, 2:823–837, 1985.

- P Kujala, P Varsta, R Goldstein, N Osipenko, and V Danilenko. As ship in compressive ice, analysis of the ice failure process. *Port and Ocean Engineering under Arctic conditions*, 2:810–823, 1993.
- P Kujala, M. Suominen, and K Riska. Statistics of ice loads measured on mt uikko in the baltic. *Port and Ocean Engineering under Arctic conditions*, 51, 2009.
- Pentti Kujala. Damage statistics for ice strengthened ships in the baltic sea 1984-1987. Technical report, Finnish winter navigation reasearch board, 1991a.
- Pentti Kujala. Safety of ice strengthened ships in the baltic sea. *Royal Institution of Naval Architects. Transactions*, 1991b.
- Pentti Kujala. Semi empirical evaluation of long term loads on a ship hull. *Maine Structures*, 9:849–871, 1995.
- Chuanke Li, Ian J Jordaan, and Rocky S Taylor. Estimation of local ice pressures using up-crossing rate. *Journal of Offshore Mechanics and Arctic Engineering*, 132, 2010.
- D M Masterson. A revised ice pressure-area curve. *Recent development of Offshore engineering in cold regions*, 2007.
- D M Masterson and R M D Frederking. Local contact pressure in ship/ice and structure/ice interactions. *Cold Regions Science and Technology*, 21: 169–185, 1993.
- Takatoshi Matsuzawa, Tadanori Takimoto, Haruhito Shimoda, and Wako Daisuke. Five-year observations of ship hull ice load in the southern sea of okhotsk. *IAHR International Symposium on Ice*, 20, 2010.
- L Müller and H. G Payer. Lload on reasearch vessel polarsteren under arctic conditions. *Port and Ocean Engineering under Arctic conditions*, 1:495–508, 1987.
- Mauri Määttänen, Pieti Marjavaara, Saarinen Sami, and Matti Laakso. Ice crushing tests with variable structural flexibility. *Cold Regions Science and Technology*, 67:120–128, 2011.

- A Nakamura, M Kano, T Nozawa, and T Kitazawa. Study on icebreaking performance of large arctic tanker. In *Proceedings of the International Conference on Port and Ocean Engineering under Arctic Conditions*, 1983.
- Andrew Palmer and John Dempsey. Model tests in ice. In *Proceedings of the 20th international conference on port and ocean engineering under Arctic conditions*, 2009.
- K Riska. Observations of the line-like nature of ship-ice contact. *Port and Ocean Engineering under Arctic conditions*, 2:785–811, 1991.
- K Riska, P Kujala, and J Vuorio. On the statistical nature of the ice-induced pressures measured on board i. b sisu. *Port and Ocean Engineering under Arctic conditions*, 2:812–823, 1985.
- Kaj Riska and Jorma Kämäräinen. A review of ice loading and the evolution of the finnish-swedish ice class rules. *Draft to the sname annual meeting in 2011*, 2011.
- Ron Ritch, R Frderking, M Johnston, Robin Browne, and Ralph Freeman. Local ice pressures measured on a strain gauge panel during the ccgs terry fox bergy but impact study. *Cold Regions Science and Technology*, 52: 29–49, 2008.
- Sanderson. *Ice mechanics: risk to offshore structures*. Graham & Trotman, 1988.
- D S Sodhi. Crushing failure during ice-structure interaction. *Engineering Fracture Mechanics*, 68:17–18, 2001.
- J St. John, A Tunik, K Riska, and Sheinberg R. Forward shoulder ice impact loads during the uscgc healy ice trials. *Port and Ocean Engineering under Arctic conditions*, 2:965–968, 2001.
- I.V Stepanov, O.Ya Timofeyev, V.A Likhomanov, S-V Frolov, and A.D Masanov. R/v "akademik fedorov" expedition along the northern sea route during summer 1994: Ice conditions, ship performance in ice, and ice loads on the ship hull. *Port and Ocean Engineering under Arctic conditions*, 1: 150–160, 1995.

- Mikko Suominen and Pentti Kujala. 21st iahr international symposium on ice. In *Ice reasearch for a sustainable environment*, 2012.
- Abdullah Suyuthi, Bernt J Leira, and Kaj Riska. Variation of the short term extreme ice loads along a ship hull. In *Proceedings of the ASME 2010 29th international conference on ocean, offshore and arctic engineering*, 2010.
- Rocky S Taylor, I J Jordaan, Chuanke Li, and Denise Sudom. Local design pressures for structures in ice: Analysis of full-scale data. *Journal of Offshore Mechanics and Arctic Engineering*, 132:1–7, 2010.
- G. W. Timco. Ice forces on structures: physical modelling techniques. Technical report, National reasearch council Canada, 1984.
- G. W. Timco and W F Weeks. A review of the engineering properties of sea ice. *Cold Regions Science and Technology*, 60:107–129, 2010.
- O Timofeev, B Egorov, A Klenov, and N Krupina. Measurement of ice loads onboard icebreaker "kapitan dranitsyn" during arcdev-expedition. *Port and Ocean Engineering under Arctic conditions*, 2:747–756, 1999.
- S Uto, S Oka, C Muramaki, T Takimoto, and K Izumiyama. Ice lload exerted on the hull of icebreaker pm teshio in the south sea of okhotsk. *Port and Ocean Engineering under Arctic conditions*, 2:683–692, 2005.
- W F Weeks. *On sea ice*. University of Alaska Press, 2010.
- R.T Weiss, B Wright, and B Rogers. In-ice performance of the molikpaq off sakhalin island. *Port and Ocean Engineering under Arctic conditions*, 1: 211–222, 2001.
- J Wells, I J Jordaan, A Derradji-Aouat, and R. S. Taylor. Small-scale laboratory experiments on the indentation failure of polycrystalline ice in compression: Main results and pressure distribution. *Cold Regions Science and Technology*, 65:315–325, 2011.

## A DNV strength rules for ships navigating in ice

DNV has the ice classes ICE-1A\*, ICE-1A, ICE-1B and ICE-1C corresponding to the FSICR classes 1A Super 1A 1B and 1C respectively and is covered in subsection 1.7.1. In addition there is ice classes ICE-C and ICE-E, which is intended for light ice conditions and light localized drift ice. ICE-C has light requirements for plating, frames, web frames, stringers welds, rudder, stem, power and propeller, while ICE-E has requirements for plating framing and stem. These will not be covered beyond this, but the DNV classes ICE-05 (or -10 or -15) Icebreaker or POLAR-10 (or -20 or -30) Icebreaker will be covered in the next paragraph, followed by the IACS unified Polar Class rules.

Vessels for Arctic and ice breaking services intended to operate unassisted in ice-infested waters of sub-Arctic, Arctic and/or Antarctic regions can have one of DNV's classes ICE-05 (or -10 or -15) Icebreaker or POLAR-10 (or -20 or -30) Icebreaker. The appropriate class is to be decided by the ship owner based on the design scenario which is a glancing impact of varying severity. 7 different areas of the hull is defined; bow, stem, stern, midship, bottom, lower transition and lower bow. The different areas are identified using vertical extension parameters which are function of class. The basic pressure is given by Equation 21, where  $F_A$  is a correction factor based on hull area and class.  $\sigma_{ice}$  is the nominal ice strength and is also a function of class. The design pressure given in Equation 22 is based on the basic pressure in addition to the correction factor for size of design contact area,  $F_B$ . Design contact area is as in Equation 23 with  $h_0$  the height of the contact area given in a table as a function of class, and  $w$  the span for longitudinal framing and the spacing for transversal spacing.

$$p_0 = 1000F_A\sigma_{ice} \quad (21)$$

$$p = F_B p_0 \quad (22)$$

$$A_C = h_0 w \quad (23)$$

In addition to buckling requirements which should be checked independently there is requirements for plate thickness, sectional area of web of frames, frame web thickness, section modulus and stiffener connection area. For plating exposed to a load patch the required thickness is as expressed in Equation 24, where  $k_a$  is the aspect ratio for the plate field, and the first fraction a kind of aspect ratio of the load, with  $s$  the spacing in case on longitudinals, or height of contact area if transversal framing, and  $h_0$  the least of contact height and spacing.  $k_w$  is an influence factor for narrow strip of load,  $m_p$  bending moment factor,  $\sigma_f$  minimum upper yield strength of steel used and  $t_k$  addition for corrosion. The requirements are, as for FSICR, different for longitudinal and transversal framing. The requirement for web area of longitudinal frames is simplified in Equation 25, where  $\alpha$  is the angle of the bow with the centerline seen from above,  $\beta$  is the frame angle with the plating,  $l$  is span and  $s$  is spacing of stiffeners and  $A_K$  an addition for corroded web area. Web thickness requirements for flanged longitudinal profiles is simplified in Equation 26, where  $h_W$  is the height of the frame web,  $t_s$  the shell plate thickness and  $t_K$  addition for corrosion. Finally the section modulus requirement is simplified in Equation 27, where  $w_k$  is a corrosion factor.

$$t = 23k_a \frac{s^{0.75}}{h_0^{0.25}} \sqrt{\frac{k_w p_0}{m_p \sigma_f}} \quad (24)$$

$$A_W = f(l, s, h_0, \alpha, \beta) + A_K \quad (25)$$

$$t_W = f(p_0, \sigma_F, \beta, h_w, h_0, t_s) + t_K \quad (26)$$

$$Z = f(h_0, \alpha, \beta, l, p_0, w_k, \sigma_f) \quad (27)$$

DNV has also adopted the IACS unified Polar Class rules, which covers Polar class-1 through 7 from highest to lowest. A work-energy approach is used, and the design load level accounts for some plastic behavior, still maintaining a reserve against rupture and collapse. Limit states are 3 hinge mechanism plastic collapse, shear failure under end load and web collapse, see Figure 43, together with existing buckling rules. Several sets of factors are used. There are five different class factors, covering crushing failure, flexural



failure, load patch dimensions, displacement and longitudinal strength, and each of these have different numbers depending on the target class. A pressure patch with dimensions  $b$  times  $w$  is used to design for pressure peaks, and pressure peak factors are developed for different structural members. Like the Finnish-Swedish rules, the different regions, or areas of the ship are associated with factors. The areas used are bow, bow intermediate, midship and stern, and all of these except bow are further separated into ice belt, lower and bottom. Each of these area factors are different for each class, and a table is given. There are different tables if the vessel is operating bow first, aft first, or if it is intended the notation "icebreaker". Plate thickness requirement is given as in Equation 28, where the average pressure is given by Equation 29,  $AF$  is the hull area factor and is a function of hull area and class,  $PPF_p$  is peak pressure factor for plate and is a function of framing system and spacing,  $\sigma_y$  is yield strength, and  $t_s$  and addition for corrosion and abrasion.

$$t = t_{net}(AF, PPF_p, P_{avg}, \sigma_y) + t_s \quad (28)$$

$$P_{avg} = \frac{F}{b \cdot w} \quad (29)$$

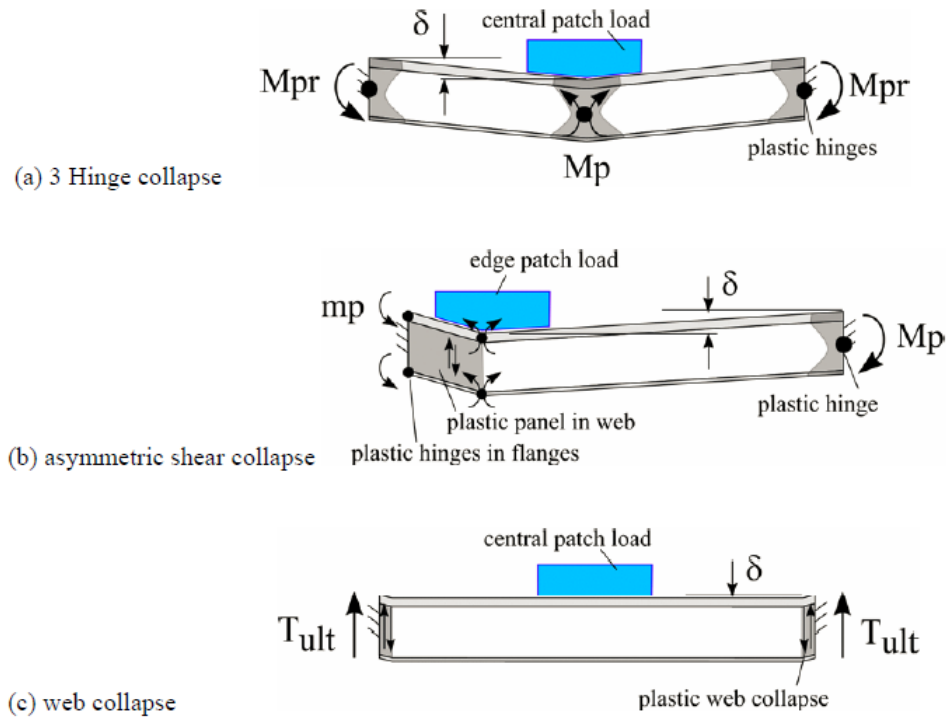


Figure 43: Design limit state for IACS rules adopted by Daley et al. [2001]

## B Matlab functions

Table 8: Overview of matlab functions, their purpose, input and output.

Function name	Input	Output	Description
colorbarplot.m	event, spevent		function plotting a 3d colored bar plot for the given event
designcurves.m		alpha, x0, x0e	function plotting design curves, alpha-area, x0-area. and comparing to curves from literature. alpha and x0 values are buildt in.
designloadreturn.m	my, rep, designzp, designzl, alpha, x0e, col	Pep, Pel, zp, zl	Given scenario and distribution parameters, plots design load vs return period. Given the nr of trig cell for area distr, returns probability of exceedance and design load
scenario.m	dpy, y, dist, col, mcells	my, y	Given a design scenario, days in compressive ice per year (dpy) and lifetime in ice (y), returns expected nr of impacts per year (my) and the return period given in input. mcells is nr of total exposed cells from
eventasess.m	timevent, spevent, nbigload	MTCtevent, MELtevent, MTCevent, MELevent	function also including other functions plotting force vs frames, spatial pressure area and 3d colorbar for timevent corresponding to max triggered cell (MTC), max event load (MEL)
Continued on next page			

Table 8 – continued from previous page

Function name	Input	Output	Description
exposed.m	spevent, sortsum	mcells	finding mcells; number of cells in the censoring matrix that has ever been triggered = "exposed cells". Plotting cumulative sum with different color saturation
findevents.m	data	pevent	taking in data from the input file, assigning adjacent values in each frame to one spatial event. pevent is as follows   spatial eventnr   value   frame   i   j
findtimeevents2.m	spevent	timeevent	assigning events that are adjacent in time and space to one timeevent. timeevents is like   timeevent   spatial event
graph.m	maxevents, mcells	x0p, al- phap	plotting Z values (pressure) probability of exceedance with weibull plotting position and exponential distribution fitted to tail. Also accounts for exposure.
isevent.m	fstore, m, n	eventnr	taking in fstore   eventnr   i   j   and indices(m,n) to be checked. If this cell have an eventnr this will be returned
longtranscumdist.m	sortsum		taking in sortsum:   i   j   value   frame   plotting vertical(rows) cummulative distribution sum for whole series, and longitudinal (column) cummulative distribution for series / 10
Continued on next page			

Table 8 – continued from previous page

Function name	Input	Output	Description
main			calls preprocessing, processing and postprocessing
man.m	distcol, col, mcells, alpha, x0, x0e	occ	
maxareadistr.m	spevent, timevent	dist	making model scale distributions using maximum event method for areas from 1 to 32 cells. dist is areas 1 to 32 in columns and distributions model scale [kPa] in rows.
maxloads.m	spevent	nbigload	taking in spevents. nbigload is [N] model scale the sum of all triggered cells within a spatial event and converting to load nbigload ->   eventnr   numbers of triggered cells   p sum   f sum
maxeventsum.m	timevent, spevent	fevent	finding what timevents has larger sum value gives out fevent showing timevent in left column and value sum in right, sorted by value, biggest on top
Continued on next page			

Table 8 – continued from previous page

Function name	Input	Output	Description
FSICR.m	zl, c	Z, A, t, Zreq, wh, wt, ft, fl, s, l, i, tp	FISCR design rules, 1a super, longitudinally framed ice belt. Finding required plate thickness, (t) [mm], shear area (A) [ $cm^2$ ], section modulus (Z) [ $cm^3$ ], spacing (s) [m], span (l) [m], rest [mm]
montecarlo.m	Ultload_my, Ultload_std, x0e, alpha, h, w, c, my	Pf, marg, load, strength	performing monte carlo simulation of load and strength
pacurve.m	spevent		going through all triggered cells and for each cell saves p-a values. If higher p value found for an area this will overwrite existing ones. Plotting local pressure area curve. spa:   area   pressure
postprocessing.m	timevent, spevent, nbigload, sortsum	mcells, MELtevent, MTCtevent, MTCevent, MELevent	running eventasess.m, exposed.m and designcurves.m
preprocessing.m		spevent, timevent	running readdata.m, find-events.m, sortevent.m and findtimevents2.m and clears workspace
processing.m	spevent, timevent	nbigload, sortsum, dist	running sumcell.m, maxloads.m and maxareadistr.m

Continued on next page

Table 8 – continued from previous page

Function name	Input	Output	Description
readdata.m		data	reading from .csv file and saving to "data" in workspace
sortevent.m	pevent	spevent	function sorting out known noise and values below lower limit. gives out spevent sorted on eventnr, new numbering. spevent is as follows  eventnr value frame i j
spatialplot.m	timevent, spevent, tevent, event		plotting riseup spatial pressure-area curve for given timeventnr (tevent) until given max event (event).
strengthdist.m	wt, wh, ft, fl, s, tp, l	Ultload_my, Ultload_std, Z	given structure and steel, finds strength distribution parameters [N] assuming normal distribution. l = span [m], s =spacing [m], rest [mm]
sumcell.m	spevent	sortsum	function adding the values of each cell, giving out sortsum, sorted by value  i j value  frame
teventmovie.m	timevent, spevent, tevent		plotting 3d colored bars for the events in the timevent (tevent) making a short movie
Continued on next page			

Table 8 – continued from previous page

Function name	Input	Output	Description
the_ring.m	dpy, y, dist, mcells, alpha, x0e, c	c, i, Zreq, Z1, Z2, t, tp, Pf	taking in the design scenario, days par year in compressive ice (dpy), return period (y), exposed cells, design parameters for distribution and number of cells exposed. It will make a structure either according to FSICR or based on the distribution with target scenario and make a monte carlo simulation to predict Pe
timemax.m	spevent, timevent	maxevents	finding $Z = \max(X1, X2...Xn)$ max triggerd cell within each timevent. maxevents:   timevent   Z [kPa]
totcontapa.m	spevent	pa	making pressure area curve considering average pressure over total measured contact area for each spatial event. lower values for each area is overwritten. model scale. pa:   pressure [kPa]   area [ $m^2$ ]

Continued on next page





## C Float charts

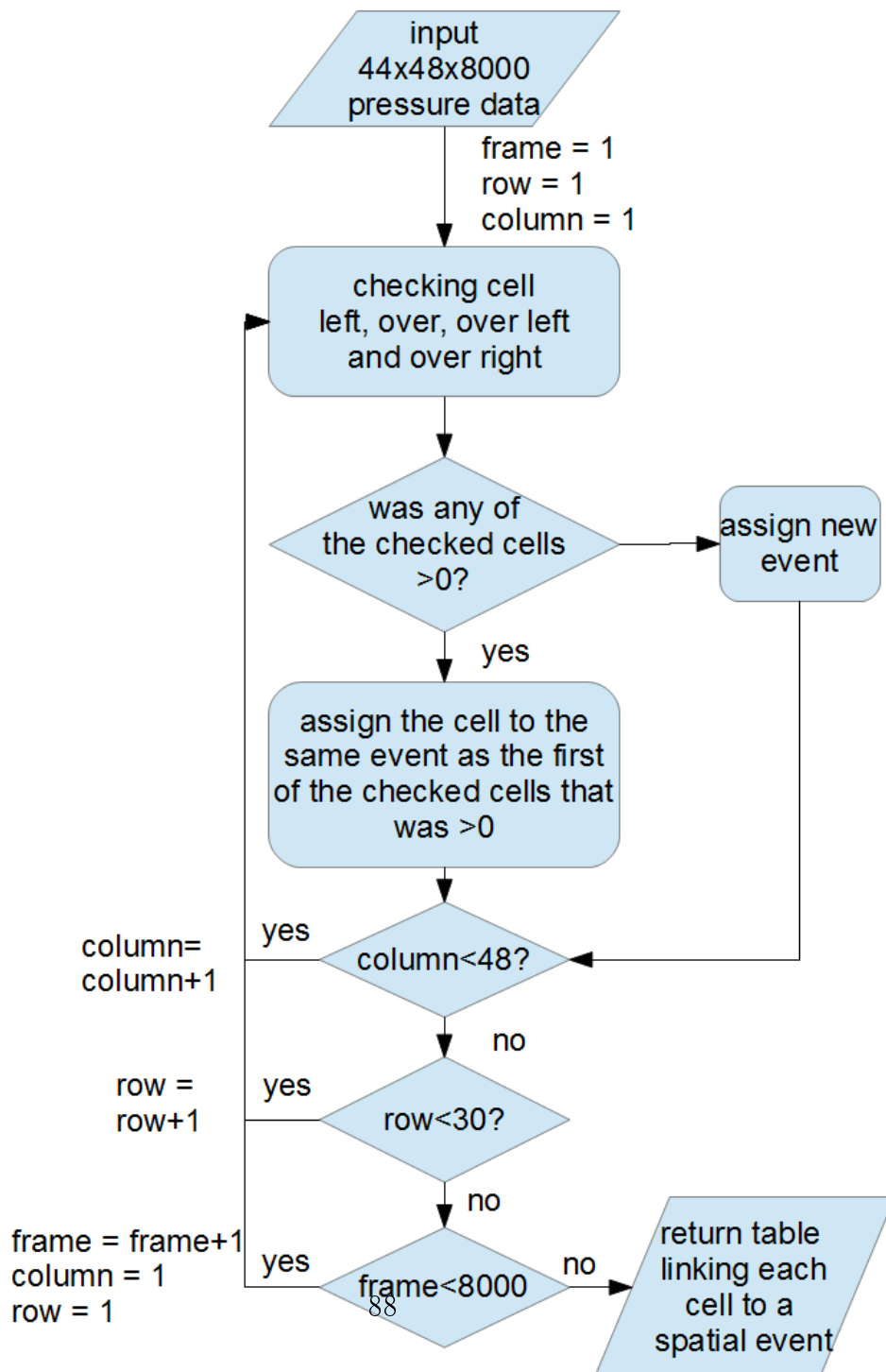


Figure 44: Float chart for function, "findevents" identifying and naming spatial event.

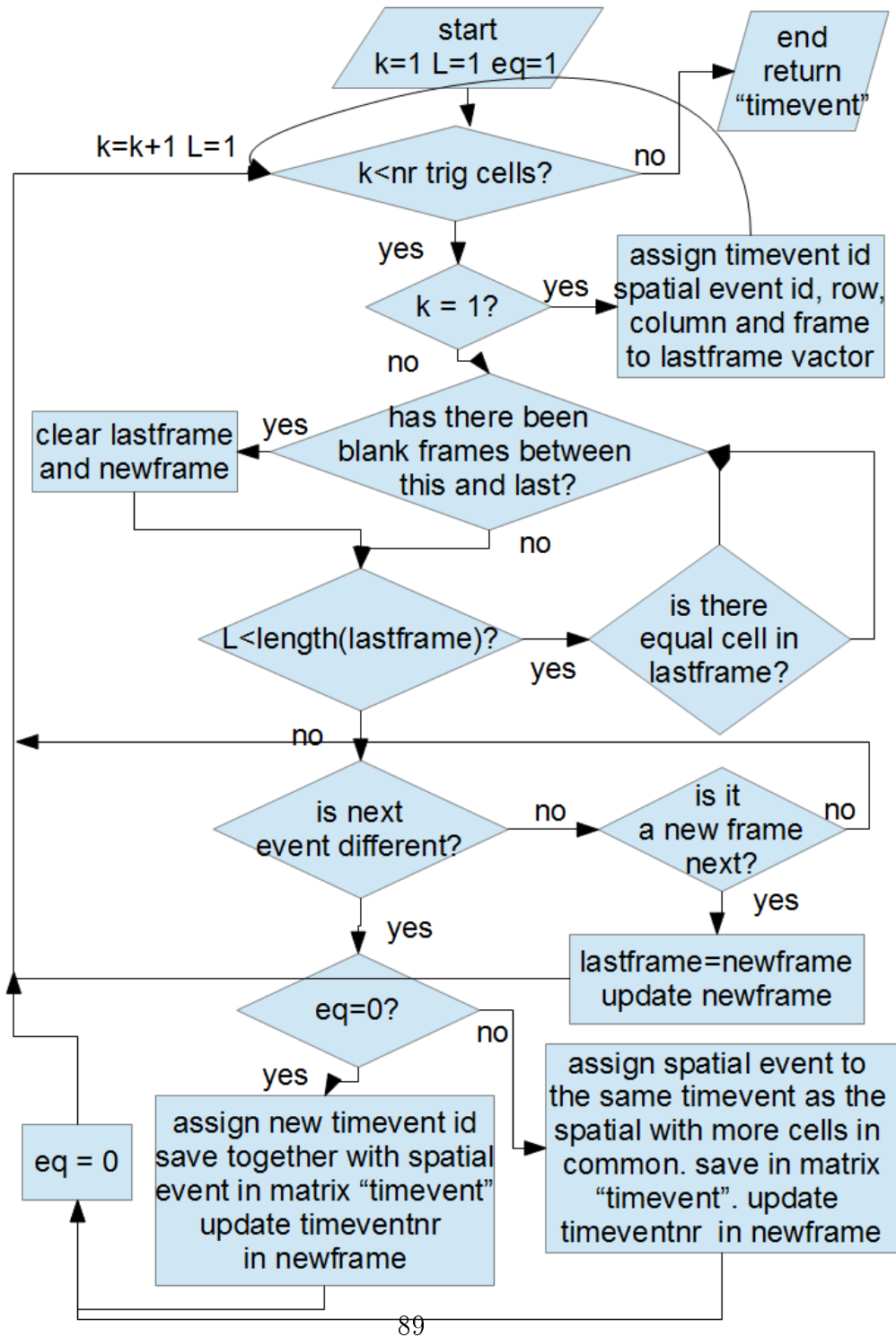


Figure 45: Flow chart for function, "findtimevents" grouping spatial events that are adjacent in time and space to one timevent id.

## D Weibull probability plots for each area

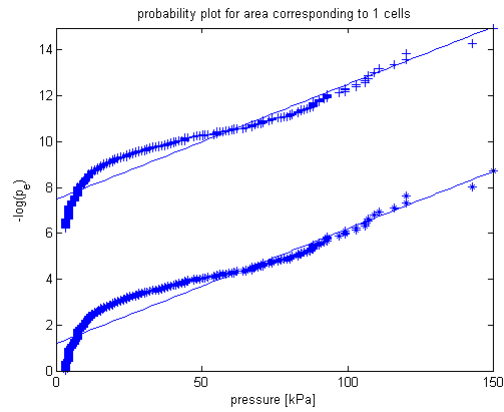


Figure 46: Weibull plot for one triggered cell

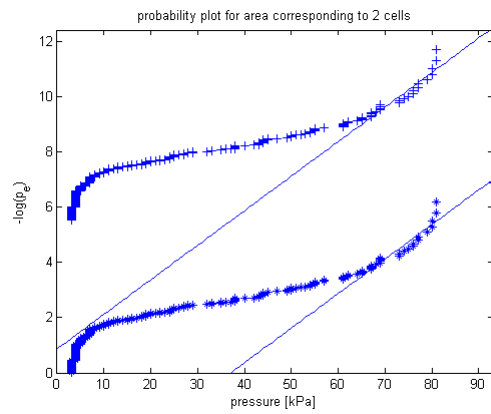


Figure 47: Weibull plot for two triggered cells

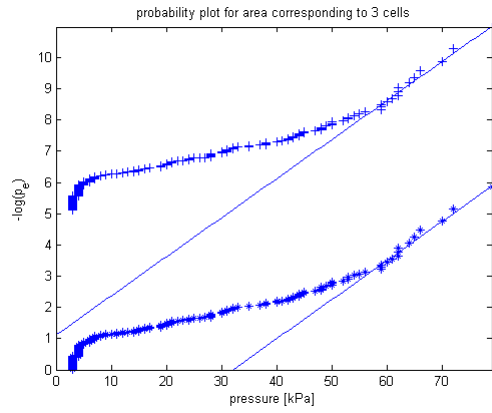


Figure 48: Weibull plot for three triggered cells

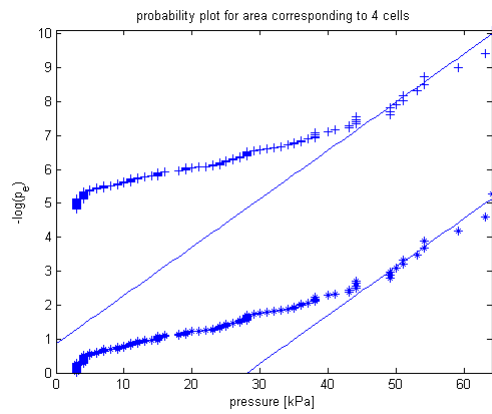


Figure 49: Weibull plot for four triggered cells

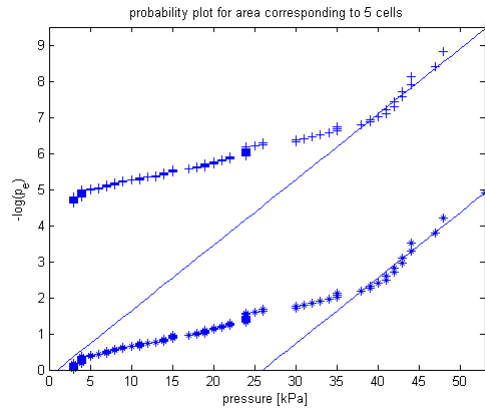


Figure 50: Weibull plot for five triggered cells

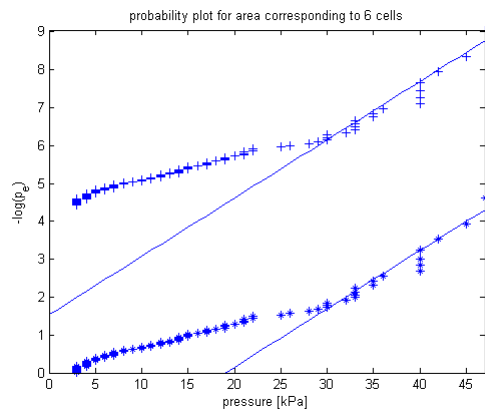


Figure 51: Weibull plot for six triggered cells

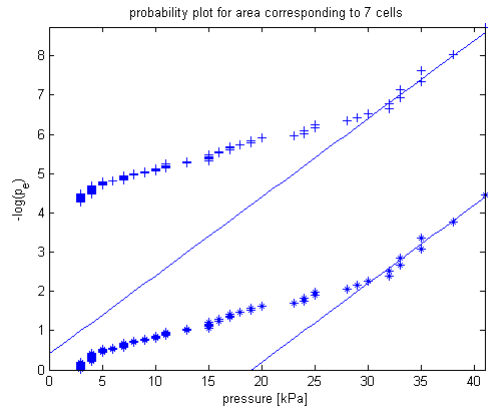


Figure 52: Weibull plot for seven triggered cells

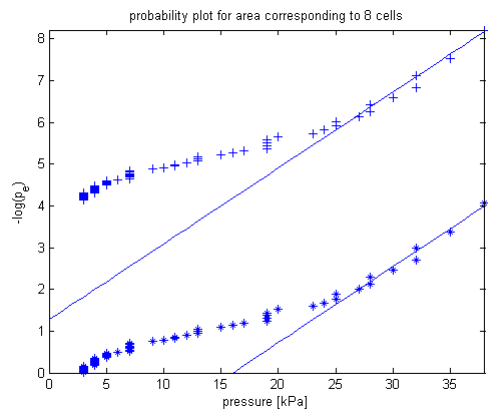


Figure 53: Weibull plot for eight triggered cells

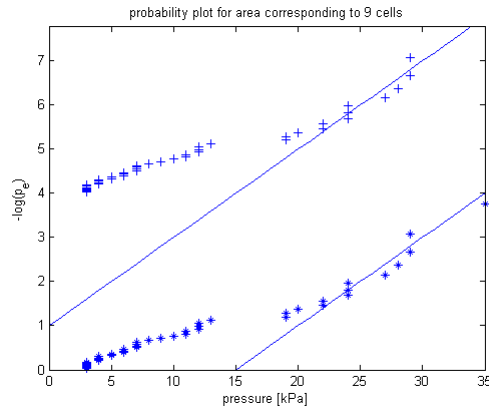


Figure 54: Weibull plot for nine triggered cells

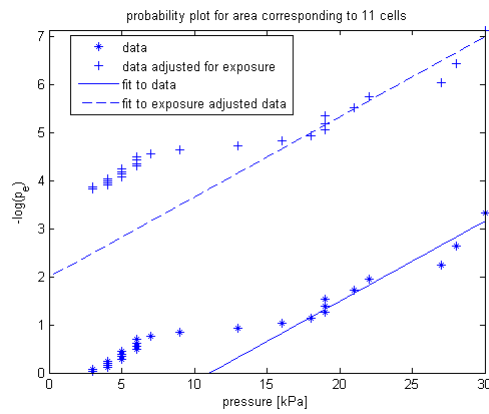


Figure 55: Weibull plot for eleven triggered cells



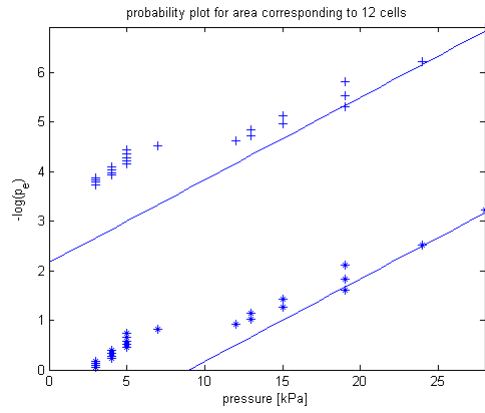


Figure 56: Weibull plot for twelve triggered cells

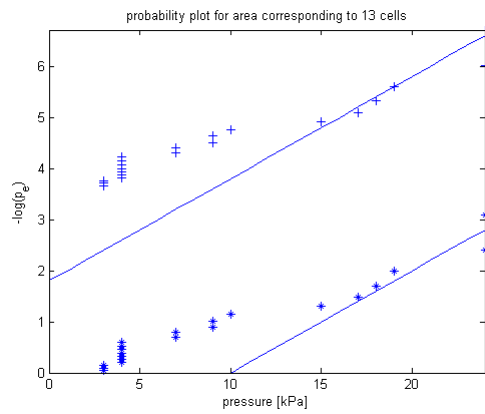


Figure 57: Weibull plot for thirteen triggered cells

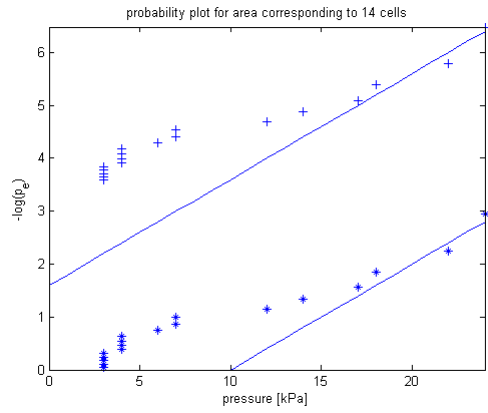


Figure 58: Weibull plot for fourteen triggered cells

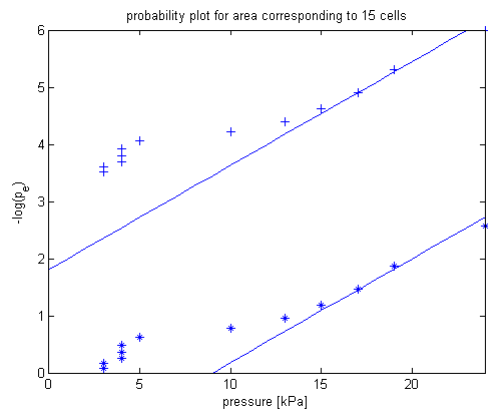


Figure 59: Weibull plot for fifteen triggered cells

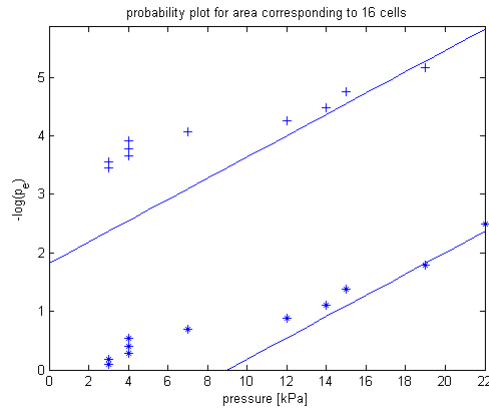


Figure 60: Weibull plot for sixteen triggered cells

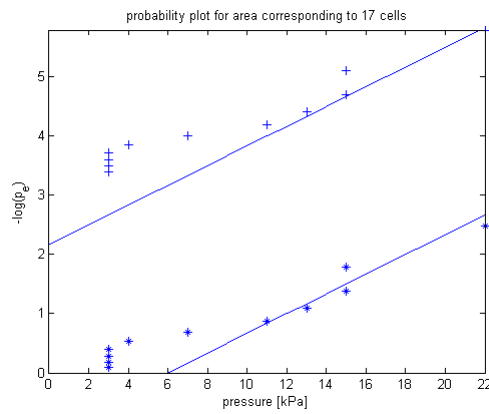


Figure 61: Weibull plot for seventeen triggered cells

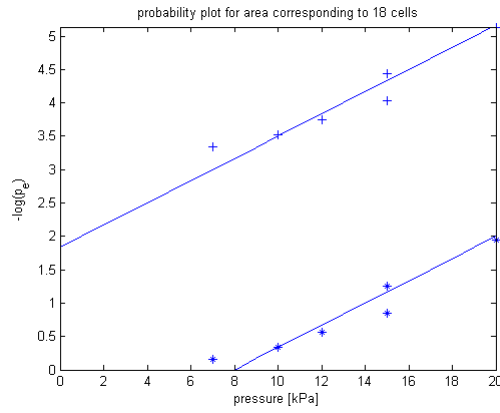


Figure 62: Weibull plot for eighteen triggered cells

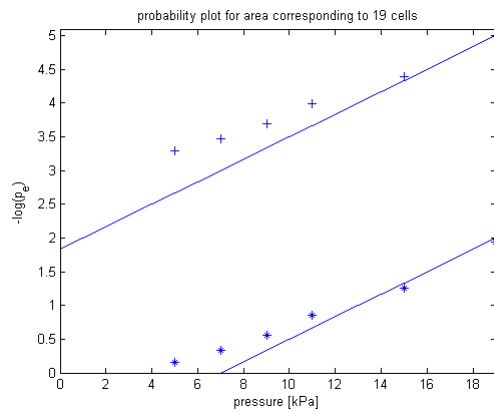


Figure 63: Weibull plot for nineteen triggered cells

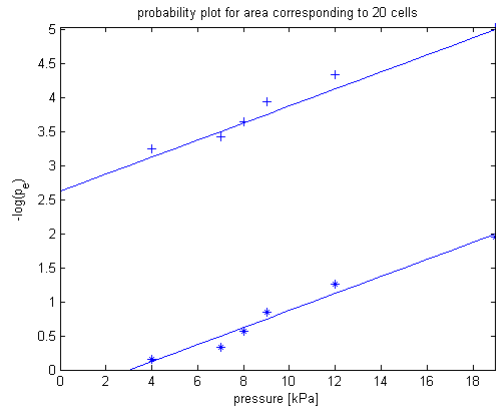


Figure 64: Weibull plot for twenty triggered cells

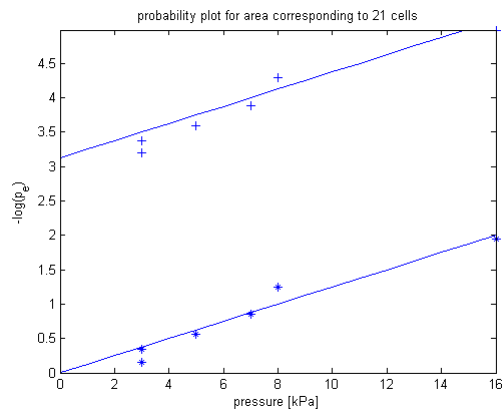


Figure 65: Weibull plot for twentyone triggered cells

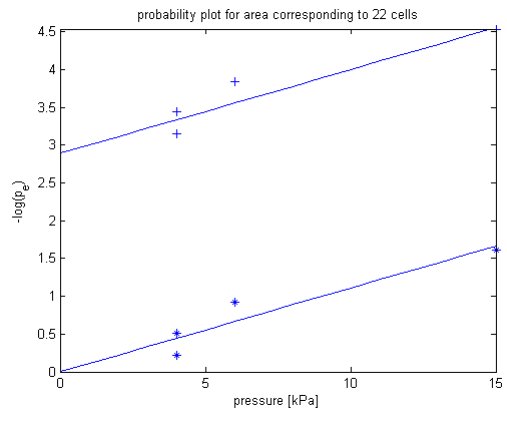


Figure 66: Weibull plot for 22 triggered cells

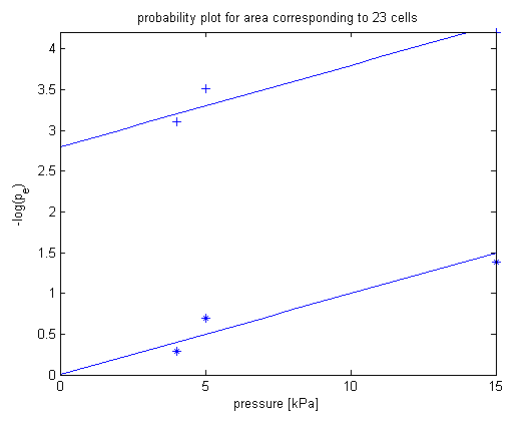


Figure 67: Weibull plot for 23 triggered cells

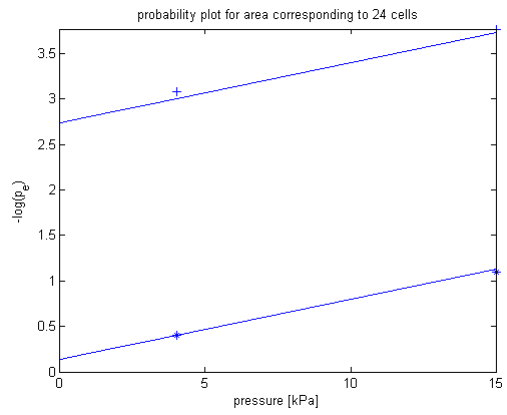


Figure 68: Weibull plot for 24 triggered cells

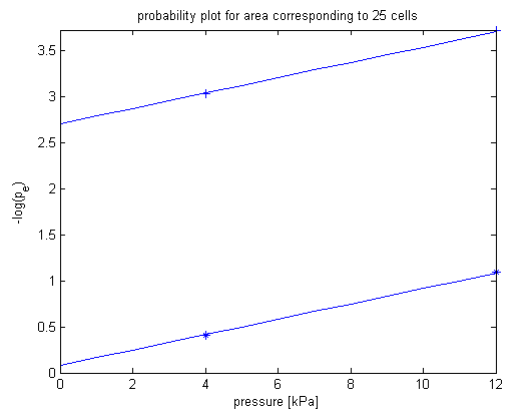


Figure 69: Weibull plot for 25 triggered cells

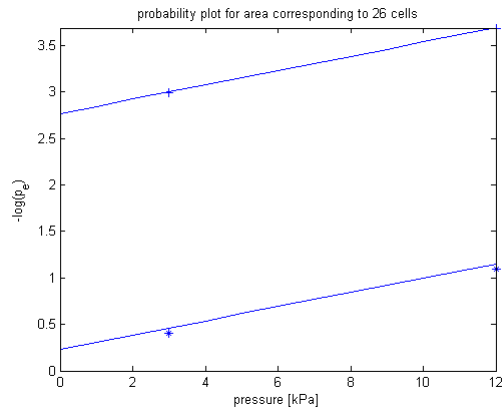


Figure 70: Weibull plot for 26 triggered cells

## E Results from monte carlo simulation

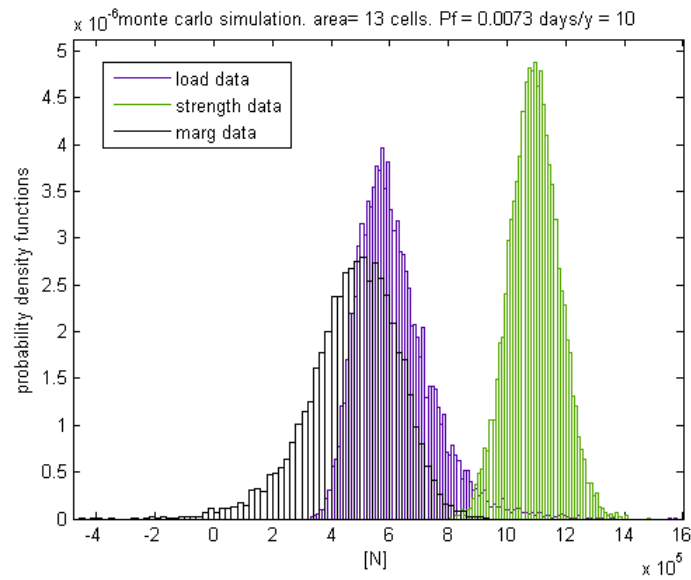


Figure 71: Monte carlo simulation for area equal 13 cells, and transversal framing for given scenario



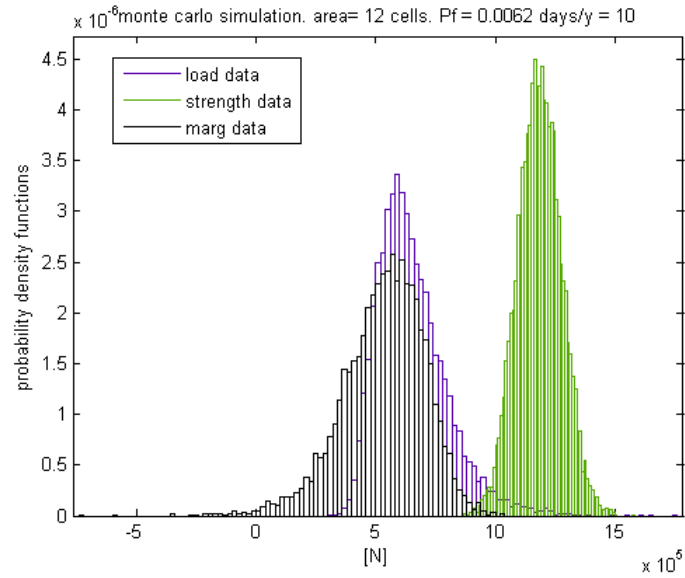


Figure 72: Monte carlo simulation for area equal 12 cells, and transversal framing for given scenario

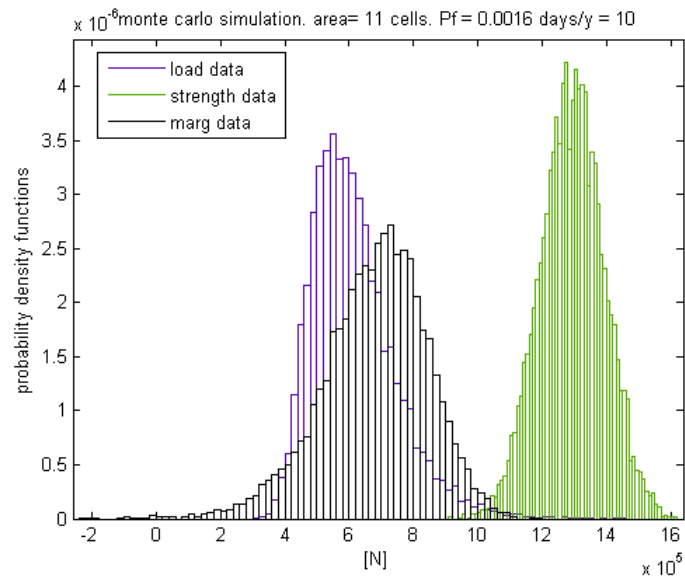


Figure 73: Monte carlo simulation for area equal 11 cells, and transversal framing for given scenario

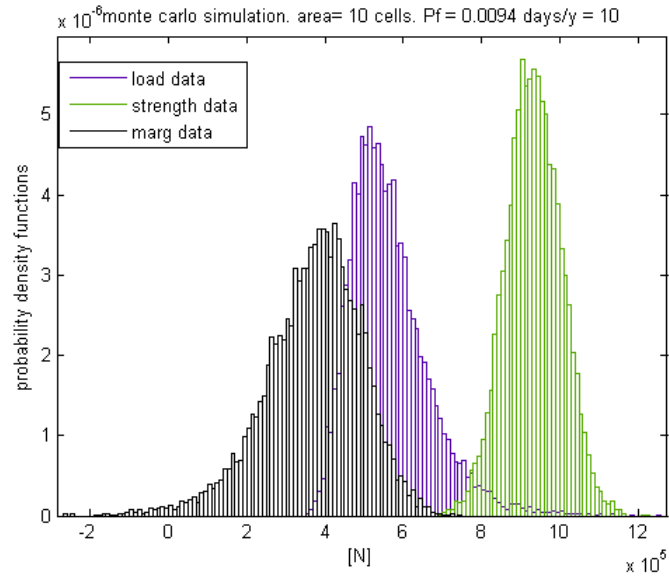


Figure 74: Monte carlo simulation for area equal 10 cells, and transversal framing for given scenario

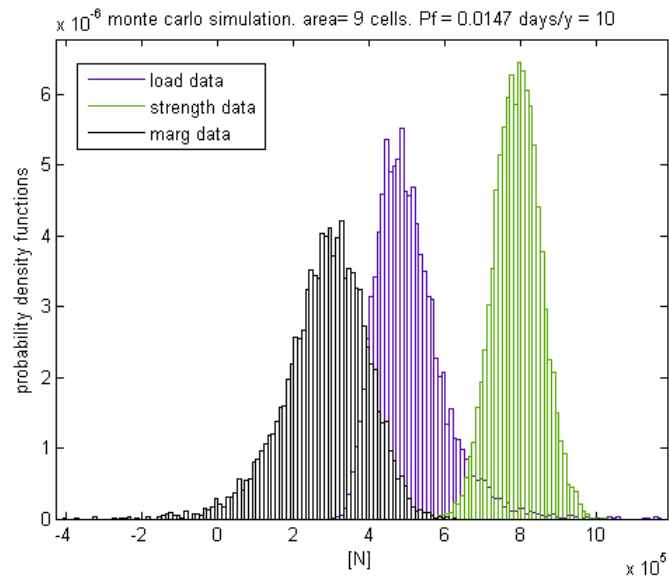


Figure 75: Monte carlo simulation for area equal 9 cells, and transversal framing for given scenario

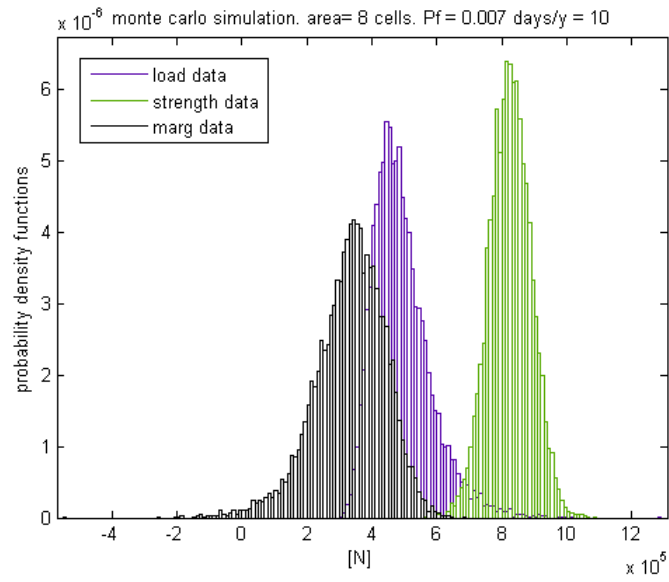


Figure 76: Monte carlo simulation for area equal 8 cells, and transversal framing for given scenario

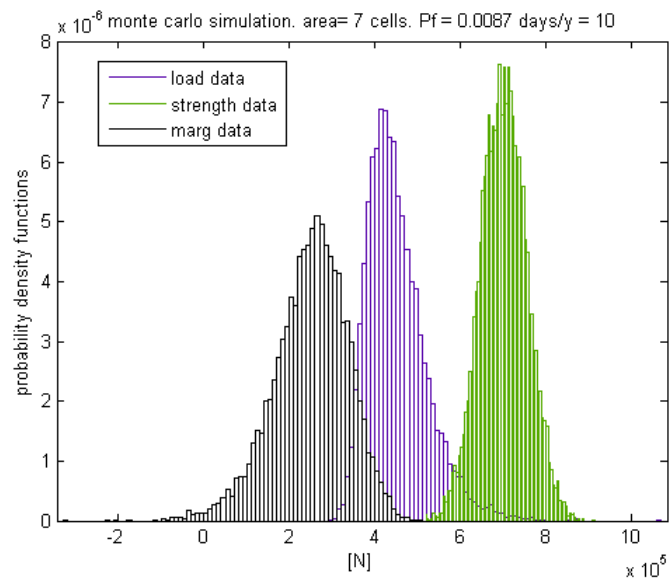


Figure 77: Monte carlo simulation for area equal 7 cells, and transversal framing for given scenario

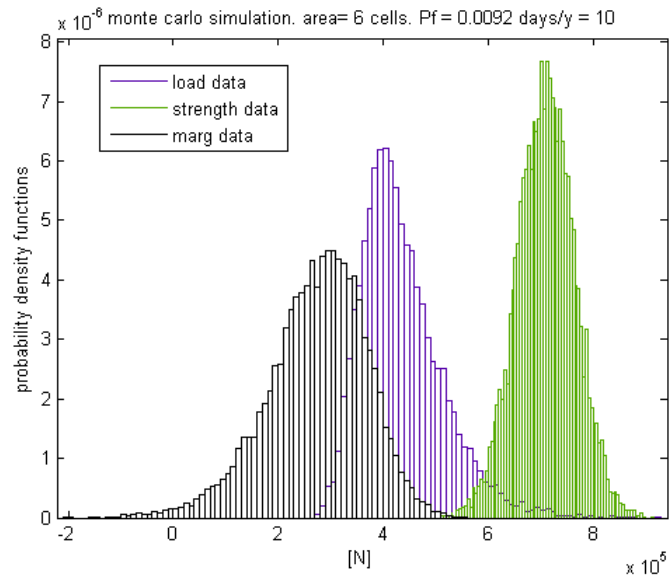


Figure 78: Monte carlo simulation for area equal 6 cells, and transversal framing for given scenario

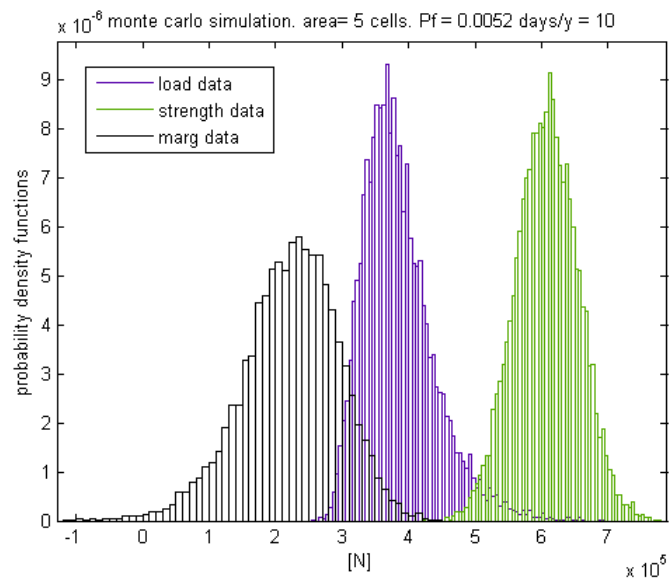


Figure 79: Monte carlo simulation for area equal 5 cells, and transversal framing for given scenario

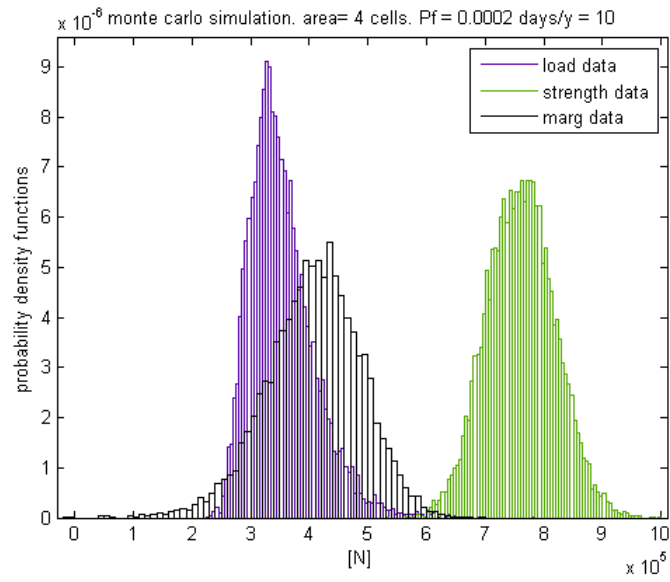


Figure 80: Monte carlo simulation for area equal 4 cells, and transversal framing for given scenario

## F Cusp breaking and rotating



Figure 81: Cusp a



Figure 82: Cusp b



Figure 83: Cusp c



Figure 84: Cusp d